Ultrafast terahertz electrodynamics of photonic and electronic nanostructures

by

Liang Luo

A dissertation submitted to the graduate faculty

in partial fulfillment of the requirements for the degree of

DOCTOR OF PHILOSOPHY

Major: Condensed Matter Physics

Program of Study Committee:

Jigang Wang, Major Professor

Costas M. Soukoulis

Adam Kaminski

Edward Yu

Kirill Tuchin

Liang Dong

Iowa State University

Ames, Iowa

2015

Copyright © Liang Luo, 2015. All rights reserved.

DEDICATION

I would like to dedicate this thesis to my parents Mr. Zhonghua Luo and Mrs. Xianqiong Zhang and to my wife Huajun Zhang. Without their support I would not have been able to complete this work.

TABLE OF CONTENTS

LIST OF FIGURES vi

ACKNOWLEDGEMENTS xvi

ABSTRACT xviii

CHAPTER 1. INTRODUCTION 1

CHAPTER 2. ULTRAFAST THZ SPECTROSCOPY TECHNIQUES 6

2.1 Ultrafast Laser Sources 6

2.1.1 Ti:sapphire oscillator 6

2.1.2 Ti:sapphire regenerative amplifier 10

2.1.3 Optical parametric amplifier 11

2.2 Ultrafast Time-resolved Pump-probe Technique 14

2.3 Ultrafast Terahertz Spectroscopy Experiment 15

2.3.1 Terahertz spectroscopy setup 15

2.3.2 Terahertz generation and detection techniques 17

2.3.3 Terahertz data analysis 22

CHAPTER 3. TERAHERTZ WAVE GENERATION FROM SPLIT-RING-RESONANTOR METAMATERIALS 25

3.1 Introduction 26

3.1.1 Metamaterials 26

3.1.2 Motivations 27

3.2 Sample Preparation and Characterization 28

3.3 Experimental Setup 29

3.4 Experimental Results 31

3.4.1 Terahertz emission from pumping electric- and magnetic-dipole resonances 31
3.4.2 Pump wavelength dependence of THz generation 32
3.4.3 Polarization dependence of THz generation 32
3.4.4 Comparison of SRRs with other emitters 33
3.4.5 Terahertz bandwidth from SRR emitter 35
3.5 Calculation of the Second-order Nonlinear Susceptibility of the SRR Emitter . 36
3.6 Theory to the Terahertz Generation From Split-Ring-Resonators 38
3.7 Summary and Outlook 42
CHAPTER 4. TERAHERTZ WAVE MANIPULATION FROM PHOTO-IMPRINTED PHOTONIC STRUCTURES AND METAMATERIALS . . 44
4.1 1D and 2D Photo-imprinted Diffraction Gratings for Terahertz Wave Manipulation 45
4.1.1 Introduction 45
4.1.2 Experimental setup and results 46
4.1.3 Summary and outlook 51
4.2 Reversible Terahertz Wave Modulation in Strongly Photoexcited Metamaterials 52
4.2.1 Introduction 52
4.2.2 Experimental setup and results 53
4.2.3 Simulations and discussions 58
4.2.4 Summary and outlook 62
CHAPTER 5. ULTRAFAST TERAHERTZ PROBES OF INTERACTING DARK EXCITONS IN CHIRALITY-SPECIFIC SEMICONDUCTING SINGLE-WALLED CARBON NANOTUBES 63
5.1 Motivations 64
5.2 Introduction to Dark Excitons in Semiconducting Carbon Nanotubes 65
5.2.1 The physical structure of carbon nanotubes 65
5.2.2 The electronic structure of carbon nanotubes 65
5.2.3 Exciton electronic states in semiconducting carbon nanotubes 71
5.3 The Optical Pump and Terahertz Probe Experiment 71

5.3.1 Sample preparation and characterization 71
5.3.2 Experimental setup 72
5.3.3 Experimental results and data analysis 73
5.4 Discussion 83
5.4.1 Excitons vs. phonons 83
5.4.2 Non-equilibrium excitonic correlations vs. thermalization 85
5.5 Summary and Outlook 86
CHAPTER 6. ON-GOING PROJECTS 88
6.1 Ultrafast Terahertz Electrodynamics of Dirac Fermions in Topological Insulator Bi_2Se_3 with Mid-infrared Excitation 88
6.1.1 Introduction 89
6.1.2 The sample preparation and characterization 90
6.1.3 Experimental setup and results 90
6.2 Other On-going Projects 94
CHAPTER 7. SUMMARY 96

LIST OF FIGURES

Figure 2.1 Normalized absorption and emission spectra of a Ti:sapphire rod. The figure is taken from *Tsunami* user manual. 7

Figure 2.2 Schematic of the femtosecond mode-locked Ti:sapphire oscillator. M: cavity mirror, P: pump mirror, Pr: prism. The figure is taken from *Tsunami* user manual. 8

Figure 2.3 Schematic of temporal interference (not drawn to scale) of several electric field oscillations with various mode frequencies for (a) random phase state and (b) mode-locked state. The bottom field (yellow) is the sum of the various modes above it. 9

Figure 2.4 Schematic of the chirped pulse amplification. The oscillator pulse is firstly broadened by a stretcher to reduce the peak power, then amplified by an amplifier, and finally compressed back to the original pulse width by a compressor. 11

Figure 2.5 Illustration of several nonlinear processes. left: optical parametric generation; middle: difference frequency generation; right: sum frequency generation. 12

Figure 2.6 Schematic showing the temporal overlap of 800 nm pump pulse ω_{p} and the seed pulse ω_{seed} from the white light continuum. ω_{p} is converted into ω_{s} and ω_{i} in the parametric generation. 13

Figure 2.7 The basic scheme of the time-resolved pump-probe experiment. The pump beam excites the sample and the subsequent probe beam measures the transient transmission or reflection (shown in dashed box) or polarization change from the sample. The temporal pump-probe delay $\Delta\tau$ of the 2 beams is adjusted by the delay stage. 15

Figure 2.8 (a) Schematic of the THz time-domain spectrometer. (b) A photo of the real spectrometer in our lab. Only the parts in the purge box are shown. 16

Figure 2.9 Top panel: an external driving electric field with frequency ω_0. Middle panel: polarization of electrons in a noncentrosymmetric medium driven by the external field. The total polarization (red) is composed of a linear component (dashed green) and a nonlinear component (dashed blue). Bottom panel: the nonlinear component (dashed blue) can be further divided into a linear component but with twice the driving frequency: $2\omega_0$ (solid blue) and a constant component (dashed blue). 19

Figure 2.10 (a) The ZnTe crystal structure. (b) An optical pulse illuminates the $\langle 110 \rangle$ cut ZnTe. The angle between the polarization of the pulse and the [001] axis is θ. (c) The generated THz intensity as a function of θ. (d) The angle between the optical pulse polarization and generated THz pulse polarization as a function of θ. The figures (a)(c)(d) are taken from Ref (5). 20

Figure 2.11 Schematic showing the electro-optic sampling technique. 21

Figure 2.12 (a) The angles of THz beam E_{THz} and sampling beam E_{p} relative to the ZnTe [001] axis. Both THz and sampling beams are perpendicular to the $\langle 110 \rangle$ cut ZnTe surface. (b) measured THz electric field amplitude as a function of the angles. The figure is taken from (7). 22

Figure 2.13 (a) The THz time-domain fields transmitted through a 2.5 mm copper clear aperture ($E_{\mathrm{ref}}(t)$, green) and a GaAs wafer mounted behind another 2.5 mm copper aperture ($E_{\mathrm{THz}}(t)$, blue), and its pump-induced field change ($\Delta E_{\mathrm{THz}}(t)$, red). (b) The corresponding THz spectra transmitted through clear aperture ($E_{\mathrm{ref}}(\omega)$, green), static GaAs ($E_{\mathrm{THz}}(\omega)$, blue), and photoexcited GaAs ($E'_{\mathrm{THz}}(\omega)$, red). 23

Figure 3.1 (a) Schematic of the SRR unit cell. (b) The SRR array on a substrate. The SRR unit cell materials can be metals such as gold, silver, copper, etc. The substrate materials can be insulators (glass) or semiconductors (GaAs, Si). 26

Figure 3.2 (a) The design dimension of the SRR (left) and electron micrograph of the actual SRR array (right) with three designed yellow SRRs overlaid in the middle to compare the designed and actual dimensions. (b) The linear optical transmission showing electric (red curve) and magnetic (black curve) dipole resonances of the SRRs. It is also plotted in the inset of Fig. 3.4 for easy reference. 29

Figure 3.3 Schematics of THz generation and detection setup. PM: parabolic mirror, WP: Wollaston prism. 30

Figure 3.4 Measured THz time-domain signals by pumping the SRR electric-dipole resonance (red line) at 800 nm, magnetic-dipole resonance (black dots) at 1500 nm and pure substrate (green line) at 1500 nm, respectively. The inset is reproduced from Fig. 3.2(b) showing electric (red curve) and magnetic (black curve) dipole resonances of the SRRs. 31

Figure 3.5 Pump wavelength dependence of THz generation from the SRR emitter. (a) A 2D false-color plot of the THz temporal traces for sweeping the pump wavelength across the magnetic-dipole resonance from 1180 to 2400 nm. The left-hand-side panel summarizes peak-to-peak amplitudes of THz emission (red diamonds) as a function of pump wavelength, together with the 1-T curve (blue solid line). T is the measured transmission around the SRR's magnetic-dipole resonance. The three colored curves (green, red, magenta) indicate the cut positions of three time-domain traces shown in (b-d) corresponding to 2180 nm, 1540 nm and 1376 nm, respectively. 33

Figure 3.6 (a) The THz signals measured at several angles between the polarization of 1500 nm pump beam and the gaps of SRRs. The traces are offset for clarity. (b) The polar graph of the peak-to-peak amplitudes of THz signals as a function of the SRR emitter rotation angle. The inset defines the angles between the polarization of the 1500 nm pump beam (black arrows) and the SRRs. 34

Figure 3.7 The peak-to-peak amplitude of THz signal versus pump energy measured with three different THz emitters: 0.2 mm ZnTe (magenta dots), 1 mm ZnTe (red diamonds) and SRR (blue squares) and the same detector of 1 mm ZnTe. The straight lines are from linear fitting. 35

Figure 3.8 The normalized time-domain THz fields and corresponding spectral amplitudes generated from the same SRR emitter and measured by three different detectors: 1 mm ZnTe detector (red, a-b); 0.2 mm ZnTe (blue, c-d); and 0.1 mm GaSe (green, e-f). 36

Figure 3.9 A Gaussian optical pulse at z=z$'$ propagates along z-axis in a nonlinear medium with thickness L. 37

Figure 3.10 (a) THz time-domain signals transmitted through free space (purple) and the 0.2 mm ZnTe crystal (red). (b) The measured refractive index of the ZnTe crystal as a function of frequency 38

Figure 3.11 Theoretical calculation of the second-order nonlinear susceptibility of the SRR emitter. THz fields generated from the SRR emitter (red) and the 0.2 mm ZnTe emitter (purple) are plotted. The nonlinear second-order susceptibility of the SRR emitter is extracted by comparing the peak-to-peak amplitudes of SRR and ZnTe emitters. 39

Figure 3.12 Distributions of the linear current (blue arrows) and nonlinear polarization (red arrows) for a linear cut-wire (left panel), the electric resonance (middle panel), and electrically excited magnetic resonance (right panel) of the SRR. The + and - indicate charge accumulation. Only the magnetic resonance of the SRR (right panel) exhibits an appreciable THz emission via difference frequency generation (DFG) due to the broken symmetry. 41

Figure 4.1 The experimental setup showing the key elements for reconfigurable diffractive gratings for THz wave manipulation. Optically projecting an image from a photomask onto a GaAs substrate creates a grating in carrier concentration in the surface of the GaAs. 46

Figure 4.2 THz transmission spectra of the photo-imprinted linear grating. (a) Experimental transmission spectra of a grating with lattice constant a=60 μm and duty cycle D=50% for several pump fluences. The inset shows the projected image of the metal mask at the position of the sample measured with a CCD camera. (b) Simulation results from a simplified model of a diffraction grating with lattice constant a=60 μm) consisting of PEC wires for different duty cycles D. 48

Figure 4.3 (a) Experimental transmission spectra for masks with varying lattice constant (Fluence is 96 μJ/cm^2; duty cycle is D=50%). The inset shows that the transmission dip frequencies are inversely proportional to the lattice constant (consistent with diffraction). The black line is the cut-off frequency of the first diffraction order in GaAs, $f = c/n_{\mathrm{GaAs}}a$. (b) Experimental transmission spectra for masks with varying duty cycle (96 μJ/cm^2; a=60 μm). The spectral position of the dips does not depend on the duty cycle (consistent with diffraction; inconsistent with a cut-wire resonance). 49

Figure 4.4 THz transmission spectra of a 2D photo-imprinted diffractive element. Inset: projected image of the metal mask at the position of the sample measured by a CCD camera. 50

Figure 4.5 Transmission spectra from computer simulations of the photo-imprinted carrier grating taking into account the lossy nature of the photoexcited carriers. The conductivity values are specified at 1 THz. The inset plots the electric field component perpendicular to the grating at f=1.6 THz. 51

Figure 4.6 Schematic of the SRR unit cell of one of the samples with lattice constant 50 μm and the polarization of the normally incident THz radiation. a = 50 μm, b = 36 μm, d = 3 μm, g = 2 μm, and w = 6 μm. 54

Figure 4.7 (a) Transient transmission spectra T(ω) taken under two excitation fluences, 19 (dashed cyan line) and 57 μJ/cm2 (solid red line), respectively. Static transmission spectra without pump is plotted together (black dotted line). (b) The nonmonotonic pump fluence dependence (indicated by the gray arrow) of the resonant absorption ~1.63 THz for low (dashed lines) and high (solid lines) photoexcitation. Spectra in both panels are taken at fixed pump probe delay of 20 ps. 55

Figure 4.8 Time evolution of transmission spectra, plotted as -$T(\omega)$, in the photoexcited metamaterial of 50 μm lattice constant for (a) 4 μJ/cm^2 and (b) 70 μJ/cm^2, respectively. These clearly show the opposite relaxation pathways for the weak and strong excitation regimes. 57

Figure 4.9 The extracted transient carrier concentration as a function of time delay. The left and right gray areas illustrate a crossover from the high to low excitation regime with a crossover density N_c (black square). The inset plots the extracted transient carrier concentration as a function of pump fluence at $\Delta\tau$ =20 ps, marked together with N_c corresponding to the density excited by 19 μJ/cm^2. 58

Figure 4.10 The transient transmission spectra $T(\omega)$ at various time delays following 70 μJ/cm^2 photoexcitation. 59

Figure 4.11 Schematic of the simulation configuration. 60

Figure 4.12 (a): The simulated THz transmission spectra for various carrier densities N. The photoinduced THz resonances in the strong excitation regime for two different lattice constants 45 and 50 μm: (b) experiment and (c) simulation. 61

Figure 5.1 Physical structures of carbon nanotubes. A nanotube is obtained by rolling-up the graphene sheet along the chiral vector and matching the two ends of the chiral vector $n\mathbf{a}_1$+$m\mathbf{a}_2$ together to form a cylinder. Therefore, the magnitude of the chiral vector also defines the circumference of the nanotube. Thus obtained nanotube is said to have chirality (n,m). Note the nanotubes shown in the 3 shaded areas are only schematic and not drawn to scale. 66

Figure 5.2 (a) Definition of the graphene lattice unit vectors $\mathbf{a}_1$ and $\mathbf{a}_2$ and unit cell shown in the shaded area in real space. There are 2 carbon atoms C_1 and C_2 in each unit cell. (b) Definition of the reciprocal lattice vectors $\mathbf{b}_1$ and $\mathbf{b}_2$ and unit cell in k space. The first Brillouin zone is shown as the shaded area. Γ is the center of the hexagon, K and K' the corners, and M the center of the edge. 67

Figure 5.3 The electronic band structue of 2D graphene sheet in the fist Brillouin zone. The figure is taken from Ref (81). 69

Figure 5.4 The carbon nanotube energy bands derived from a 2D graphene sheet. If the allowed wave vector k (solid lines, left panel) goes through one of the Dirac points, the energy band has zero bandgap. Such nanotubes are metallic tubes (the top panel). On the other hand, if the allowed wave vector k does not go through any of the Dirac points, the energy band has finite bandgap. Such nanotubes are semiconducting tubes (the bottom panel). The allowed k values are determined by the chiral vector. The figure is taken from Ref (82). 70

Figure 5.5 (a) The lowest electronic levels of semiconducting carbon nanotubes in the first Brillouin zone. (b) The simplified excitonic energy levels of (a) due to Coulomb mixing of electron and hole pairs. Only a few representative states are shown. The dark exciton states are indicated by dashed lines. The bright exciton states are indicated by solid lines. 72

Figure 5.6 The absorption of the 50 μm thick SWNTs/SDBS film showing clearly the dominant (6,5)(7,5) nanotube E_{11} and E_{22} bands. The red arrows indicate 2 photon energies used to excite the sample, either resonant excitation of (6,5) E_{22} transition at 2.17 eV or off-resonant excitation at 1.55 eV which is away from any exciton resonance peak. 73

Figure 5.7 The temporally- and spectrally-resolved differential transmission $\Delta T/T$ after 1.55 eV photoexcitation of the SWNTs sample at T=300 K showing clearly the excitation of mainly (6,5) and (7,5) chiralities. 74

Figure 5.8 The schematic of the optical pump THz probe experimental setup. BS: beam splitter, WP: Wollaston prism. The THz section of the setup is purged with dry N_2 gas as shown in the dashed box. 75

Figure 5.9 Schematic of two-particle *e*-*h* pair dispersion, illustrating the lowest-lying $1s(g) \rightarrow 1s(u)$ intraexcitonic transitions (red arrows) resonantly probed by THz pulses. 76

Figure 5.10 Photoinduced THz spectrum changes of (a) $\Delta\sigma_1^{\mathrm{NT}}$ and (b) $\Delta\varepsilon_1^{\mathrm{NT}}$ (red dots), measured at pump-probe delay $\Delta\tau$=0.5 ps after 1.55 eV pumping with fluence 96 μJ/cm^2 (3.9×10^{14} photons/cm^2) at T=5 K. The black line is the fit using the analytical model Equ. 5.12, which is the sum of the $1s(g) \rightarrow 1s(u)$ excitonic (dashed green line) and unbound *e*-*h* responses (dash-dotted blue line). Inset of (a): the corresponding transmitted THz time-domain fields through reference (a clear aperture) $E_{\mathrm{ref}}(t)$ (gray), unexcited sample $E_{\mathrm{THz}}(t)$ (blue), and its pump-induced change $\Delta E_{\mathrm{THz}}(t)$ (red). 77

Figure 5.11 Comparison of photoinduced THz conductivity changes $\Delta\sigma_1^{\mathrm{NT}}(\omega)$ at $\Delta\tau$=0.5 ps and under an excitation density of 1.4×10^{14}/cm^2 with (a) off-resonant excitation at 1.55 eV and T=5 K, (b) resonant excitation at 2.17 eV and T=5 K, and (c) resonant excitation at 2.17 eV and T=300 K. 78

Figure 5.12 (a) Photoinduced THz spectrum changes $\Delta\sigma_1^{\mathrm{NT}}(\omega)$ and $\Delta\varepsilon_1^{\mathrm{NT}}(\omega)$ (black dots) at several pump-probe delays after resonant (6,5) E_{22} excitation at 2.17 eV and T=5 K. Shown together are the fitting (red lines) and peak positions indicated by the dashed cyan line. (b) The ratio $R = F_{g\rightarrow u}^{1s} \cdot(\varepsilon_0 m/e^2)/(n_{\mathrm{ph}} - n_{eh})$ as a function of pump fluence. (c) The temporal decay of exciton (Δn_{X}) and unbound plasma *e*-*h* (n_{eh}) densities as a function of time delay (top panel) and the reciprocal of Δn_{X} and n_{eh} density decay together with fitting (bottom panel). The traces in the bottom panel are vertically offset for clarity. 80

Figure 5.13 (a) Photoinduced THz spectrum changes $\Delta\sigma_1^{\mathrm{NT}}(\omega)$ and $\Delta\varepsilon_1^{\mathrm{NT}}(\omega)$ (red dots) at several pump fluences after 1.55 eV excitation, $\Delta\tau$=0.5 ps, and T=5 K. The fitting (black lines) is divided into individual components (see text) and the vertical dashed lines indicate the shift of the $1s(g)\rightarrow 1s(u)$ peak positions. (b) The resonance peak as a function of unbound e-h density. (c) Fluence dependence of the unbound e-h density (n_{eh}, red dots) and exciton density (Δn_{X}, black dots), which is divided into two regimes at I_C ~130 μJ cm^{-2} (dashed arrow). 82

Figure 5.14 (a) Static THz conductivity spectra of SWNTs at T=5 K and room temperature. (b) 800 nm photoinduced transient transmission THz field change of SWNTs at T=5 K. 84

Figure 6.1 Schematic of the energy dispersions of a typical TI. The energy scale bars indicate the energy levels of one of the Bi_2Se_3 TI samples that we have studied and presented in this section. 89

Figure 6.2 Static THz fields transmitted through a sapphire substrate (red, left panel) and 40 QLs Bi_2Se_3/sapphire sample (blue, left panel). On the right panel are the extracted static conductivity $\sigma_1(\omega)$ and dielectric function $\varepsilon_1(\omega)$ of the sample. 91

Figure 6.3 Temporal scans of transmitted THz field changes after 3.15 μm (top panel) and 4.5 μm (bottom panel) photoexcitation at several fluences. One of the 3.15 μm pump-probe scans from the top panel (1.6 μJ/cm^2, cyan line) is also plotted in the bottom to compare the signal of above- and below-bandgap excitations. 92

Figure 6.4 Photoinduced THz time-domain field change $\Delta E_{\mathrm{THz}}(t, \Delta\tau)$ at (a) T=300 K and (b) T=5 K after 5 μm excitation with various pump-probe delays. The corresponding photoinduced conductivity change $\Delta\sigma_1(\omega, \Delta\tau)$ at (c) T=300 K and (d) T=5 K. 93

ACKNOWLEDGEMENTS

I would like to take this opportunity to thank all the people who help me in all aspects in order for me to conduct research, discover new science, publish papers, and write this thesis.

First of all, I would like to thank my advisor Professor Jigang Wang for his guidance and help throughout my Ph.D. study. Jigang is one of my best advisors. He is very patient and always supervises me in a manner that is easy for me to follow. Jigang instructed me not only the knowledge in ultrafast laser spectroscopy techniques and how I should analyze experimental observations and interpret their physics scenarios, but the way of thinking and conceiving new ideas. These will benefit me significantly in my future work and research. I greatly appreciate all the help from him that is very precious to me.

Next I would like to thank my colleagues in our lab. Dr. Ioannis Chatzakis, Dr. Tianqi Li, Aaron Patz, and Xu Yang. They are very easy-going and help me a lot not only in scientific research but also in living. I am very glad to work with them all the times.

I would also like to thank my collaborators. Professor Costas Soukoulis, Professor Thomas Koschny, and Professor Jiangfeng Zhou, who provide me high quality samples and world-class theoretical support to help me understand experimental observations. I wish to thank Professor Martin Wegener, Dr. Fabian Niesler, Professor Jacek Furdyna, and Professor Xinyu Liu, who also provide me high quality samples so that my research can proceed smoothly and successfully.

My thanks also go to the staff members in the Department of Physics and Astronomy and Ames Lab-USDOE, who assist me continuously such as class registration, safety training, lab components purchasing, and various paperwork.

I would additionally like to thank my committee members, who helped me better plan my research and brought me insights from their expertise.

Finally I would like to thank my family for their support and understanding. This work would not be done without them.

This work was supported by the U.S. Department of Energy (DOE), Office of Basic Energy Science, Division of Materials Sciences and Engineering at the Ames Laboratory under contract number DE-AC02-07CH11358. The Ames Laboratory is operated for the DOE by Iowa State University. The document number assigned to this thesis/dissertation is IS-T3141.

ABSTRACT

This thesis summarizes my work on using ultrafast laser pulses to study Terahertz (THz) electrodynamics of photonic and electronic nanostructures and microstructures. Ultrafast time-resolved (optical, NIR, MIR, THz) pump-probe spectroscopy setup has been successfully built, which enables me to perform a series of relevant experiments. Firstly, a novel high efficiency and compact THz wave emitter based on split-ring-resonators has been developed and characterized. The emitter can be pumped at any wavelength by tailoring the magnetic resonance and could generate gapless THz waves covering the entire THz band. Secondly, two kinds of new photonic structures for THz wave manipulation have been successfully designed and characterized. One is based on the 1D and 2D photo-imprinted diffractive elements. The other is based on the photoexcited double-split-ring-resonator metamaterials. Both structures are flexible and can modulate THz waves with large tunability. Thirdly, the dark excitons in semiconducting single-walled carbon nanotubes are studied by optical pump and THz probe spectroscopy, which provides the first insights into the THz responses of nonequilibrium excitonic correlations and dynamics from the dark ground states in carbon nanotubes. Next, several on-going projects are briefly presented such as the study of ultrafast THz dynamics of Dirac fermions in topological insulator Bi_2Se_3 with Mid-infrared excitation. Finally, the thesis ends with a summary of the completed experiments and an outlook of the future plan.

CHAPTER 1. INTRODUCTION

Terahertz (THz) spectral band, loosely defined from 0.1 THz to 15 THz (1 THz = 4.1 meV = 300 μm = 33 cm^{-1} = 48 K), is one of the least explored spectral ranges due to the lack of efficient and compact THz wave emitters and detectors for a long time. For the past years, a few approaches have been developed to generate and detect THz radiation, such as quantum-cascade lasers, photoconductive antennas, optical rectification, free electron lasers, electro-optic sampling, bolometers, and pyroelectric detectors, etc. Some of them require cryogenic temperatures to operate (quantum-cascade lasers, bolometers) and some are very bulky (free electron lasers). The most popular table-top generation and detection techniques include optical rectification, photoconductive antennas, and electro-optic sampling. However, compared with other spectral bands from radio waves to γ-rays, THz generation and detection efficiencies by these techniques are much weaker.

On the other hand, a lot of very interesting science is only accessible by THz frequencies, such as the rotational energy transitions of molecules, vibrational motion of organic compounds, lattice vibrations in solids, intraband transitions in semiconductors, and energy gaps in superconductors, etc. Furthermore, THz radiation has a lot of practical applications, such as communications, security screening, drug detection, non-invasive evaluation, imaging, medical analysis, real-time air pollution monitoring, etc. Therefore, developing more efficient and compact THz wave emitters and detectors is a pressing problem to be solved by the community. It would enable the deeper exploration of THz science and technology.

Meanwhile, in order to make use of THz waves more efficiently, they need to be very well controlled, such as by waveguides and modulators. However, controlling THz waves has proven to be more difficult than other spectral bands. A major recent progress that scientists have made is to use artificial materials containing conductive structures such as metamaterials and

other photonic structures to control THz waves. However, the functionality of such devices is still limited with little tunability. Therefore, designing more flexible and tunable THz wave modulators is one of the pressing problems to be solved by the community.

Moreover, the interaction of THz waves with condensed matter is a highly active area of research. The THz band is filled with numerous spectral features associated with fundamental physical phenomena, such as lattice vibrations, intraband transitions, and phase transitions in semiconductors and superconductors, which are still poorly understood. Some of the outstanding problems to be studied are, e.g., the phase transition in many particle *e*-*h* systems and THz electrodynamics of nonlinear optics in photonic structures such as metamaterials and plasmonics.

In order to solve the above mentioned pressing problems in our community, I have successfully built ultrafast time-resolved (optical-, NIR-, MIR-, THz-) pump-probe setup to conduct a series of relevant experiments. Specifically, my topics of research can be divided into 2 areas: first, the study of photonic nanostructures and microstructures, such as split-ring-resonator metamaterials and plasmonics as THz wave modulators; second, the study of complex electronic nanostructures, such as semiconducting single-walled carbon nanotubes, graphene, and topological insulators Bi_2Se_3 in order to understand low energy electrodynamics of complex materials. More specifically, I have participated in:

(1) the development of a novel high efficiency and compact broadband split-ring-resonator-based THz emitter. Unlike the conventional THz emitters, such as ZnTe/GaSe/GaP/InP/GaAs /$LiNbO_3$, the new emitter overcomes 2 severe limitations that exist in almost all conventional emitters, i.e., the strong absorbing phonon gap and subtle phase-matching requirement. Additionally, the new emitter has second-order nonlinear susceptibility three-orders of magnitude higher than the conventional emitters and it can be pumped at any wavelength by tailoring the magnetic dipole resonance and potentially generate gapless continuous THz wave covering the entire THz band.

(2) the design and characterization of new photo-imprinted photonic structures as THz wave modulators. Unlike conventional photonic devices which are fabricated physically with fixed structures, we just use one laser beam to modulate another. There is no real device.

This is realized by projecting an optical image from a photomask onto a GaAs substrate. The resulting high-contrast pattern of photoexcited carriers creates diffractive elements to modulate THz waves with reconfigurable functionality.

(3) the study of strongly photoexcited graphene monolayer by using femtosecond laser pulses and found femtosecond population inversion and stimulated emission of dense Dirac Fermions in graphene. This finding demonstrates that graphene is a good potential laser gain medium to emit broadband laser light.

(4) the study of dark exciton physics in semiconducting single-walled carbon nanotubes by using optical pump and THz probe spectroscopy. This study provides the first insights into the chirality-specific THz responses of nonequilibrium excitonic correlations and dynamics from the dark ground states in carbon nanotubes. This technique may also evolve into a benchmark approach for quantitative exciton management in single-walled carbon nanotube-based device development.

In this thesis, THz spectroscopy is the main experimental scheme to study the photonic and electronic nanostructures and microstructures. Most of the study presented in this thesis is based on this technique. Specifically, the thesis is organized as follows:

In Chapter 2, an introduction to the ultrafast laser sources in our lab is presented, such as Ti:sapphire oscillator, Ti:sapphire amplifier, and optical parametric amplifier. Their working mechanisms and some useful parameters are also provided. Next, ultrafast time-resolved pump-probe technique and THz spectroscopy setup are described. Especially the THz generation and detection techniques that we are using are discussed in detail. Finally, the chapter ends with an explanation of THz data analysis.

In Chapter 3, a novel high efficiency and compact THz wave emitter is demonstrated. The emitter is composed of a single layer of 40 nm thick gold film of split-ring-resonator (SRR) metamaterials on a 1 mm suprasil substrate. This chapter starts with a general introduction to metamaterials and the current situation of THz generation and detection techniques that also points out our motivations for doing this project. The details of the SRR emitter fabrication is provided. Next, the detailed experiment setup and characterizations of the SRR emitter by various measurements (wavelength-dependent, power-dependent, polarization-dependent,

etc.) are described. The second-order nonlinear susceptibility of the emitter is also calculated. Lastly, theoretical explanation of the THz emission mechanism is presented.

In Chapter 4, two kinds of photonic structures for THz wave manipulation are presented. One is the 1D and 2D photo-imprinted diffractive gratings and the other is photoexcited double-SRRs metamaterials. The chapter starts with 1D and 2D photo-imprinted photonic structures. The experimental setup, photonic structure geometries and dimensions are presented in detail. Next, THz modulation results as a function of the structure lattice constant, duty cycle, and pump fluence are described. Simulation is also performed in order to fully understand and explain the mechanism of the observed results. Afterwards, the chapter moves on to the second structure: the photoexcited double-SRRs metamaterials. This section is organized similarly as the first one.

In Chapter 5, the THz electrodynamics of the dark excitons in chirality-specific semiconducting Single-Walled Carbon Nanotubes are studied. This chapter starts with an introduction to the physical and electronic structures of carbon nanotubes. The dark exciton energy dispersion of semiconducting carbon nanotubes is also described. Next, the sample preparation procedures and basic characterization results are provide. The experimental setup and how we understand and analyze THz results are discussed in detail, for example, the THz responses of dark excitons after resonant and off-resonant photoexcitations with different fluence and different lattice temperature. Finally, I summarize the project and also propose future experiments.

In Chapter 6, several on-going projects performed with the optical- or MIR-pump and THz-probe spectroscopy experiments are briefly presented. All of the projects aim to study the low energy electrodynamics of complex materials, which is poorly understood currently. The first on-going project is to study the ultrafast THz electrodynamics of Dirac fermions and bulk states in topological insulator Bi_2Se_3 with MIR excitation. The motivation of this project is to understand the coupling mechanism and charge transport dynamics of two spatially separated insulating and conducting states in Bi_2Se_3 at different lattice temperatures and excitation wavelengths. The other two on-going projects are the study of temperature-dependent THz responses of $BaMn_2As_2$ and the wavelength- and polarization-dependent THz responses of valleytronic material of MoS_2 monolayer and bilayer. Since the projects are not complete yet,

all results and interpretations presented in this chapter represent our best understanding of the results so far.

Finally, in Chapter 7, a short summary of what I have done and what is planned to be done in the near future concludes this thesis.

CHAPTER 2. ULTRAFAST THZ SPECTROSCOPY TECHNIQUES

In this chapter, the ultrafast laser sources used in our lab, such as Ti:sapphire oscillator, Ti:sapphire amplifier, and optical parametric amplifier are presented. Their working mechanisms and some useful laser parameters are also provided. Next, ultrafast time-resolved pump-probe technique and THz spectroscopy setup are described. Especially the THz generation and detection techniques that we are using in our lab are discussed in detail. Finally, this chapter ends with THz data analysis showing how to extract ultrafast time-resolved parameters such as refractive indices, conductivities, dielectric functions, absorption coefficients, and others from photoexcited materials.

2.1 Ultrafast Laser Sources

2.1.1 Ti:sapphire oscillator

The mode-locked Titanium-doped sapphire (Ti:sapphire) oscillator is *Tsunami* from Spectra-Physics. It uses Ti:sapphire rod as the gain medium. The Ti^{3+} ions replace a small percentage of Al^{3+} ions and is responsible for the lasing action. The material has absorption from 400 nm to 600 nm, centered at ∼500 nm. It also provides very broad band fluorescence from 650 nm to 1080 nm, as shown in Fig. 2.1.

A folded cavity is utilized in the laser to save space, although it makes pumping a bit more complex. The schematic of the oscillator configuration is shown in Fig. 2.2. The Ti:sapphire rod of the oscillator is pumped by a 10 W continuous wave (cw) green laser beam with central wavelength 532 nm, which is from the frequency doubling (by a non-critically phase-matched temperature-tuned lithium triborate (LBO) crystal) of 1064 nm emission from neodymium-doped yttrium vanadate (Nd:YVO_4) material pumped by a fiber-coupled bar (FC*bar*) module.

The Ti:sapphire rod surfaces are Brewster-angle-cut to ensure optimal transmission. In addition, cavity losses are minimized to have all the surfaces of input and output windows, prisms, and acousto-optic modulators accurately aligned or cut at the Brewster angles as indicated in the figure.

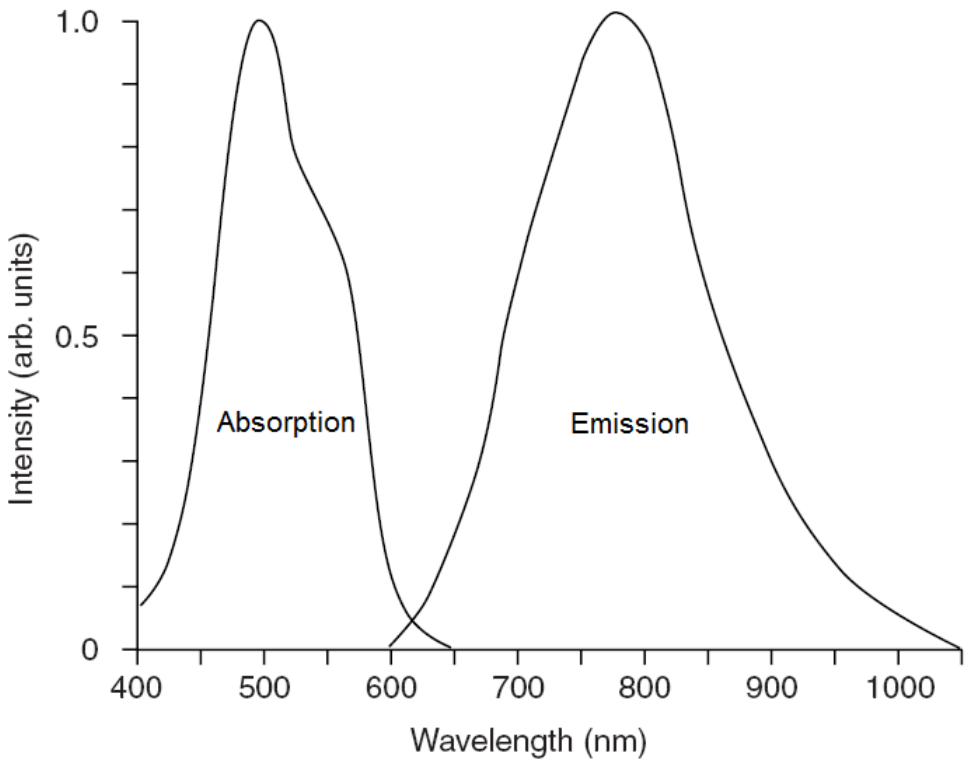

Figure 2.1 Normalized absorption and emission spectra of a Ti:sapphire rod. The figure is taken from *Tsunami* user manual.

Although laser light is quite pure and collimated, for cw operation, the laser output still comprises various randomly-phased mode frequencies. Such cw laser has relatively small peak power and field as shown in Fig. 2.3(a). In order to produce pulsed laser light with extremely large peak power and short time duration, all the longitudinal modes must be locked in phase so that they interfere constructively at some point in the cavity and destructively elsewhere in order to create a single circulating pulse, as shown in Fig. 2.3(b). In the mode-locked state, the constructive interference leads to a train of laser pulses with very large peak power and short duration. The pulse separation is $T = 2L/c$, where L is the length of the cavity and c the

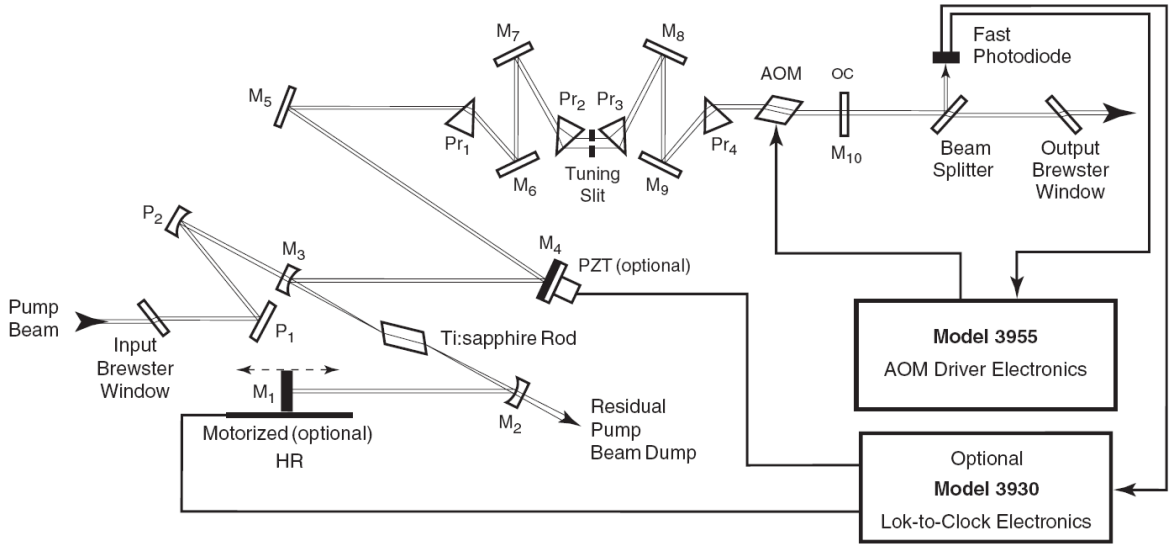

Figure 2.2 Schematic of the femtosecond mode-locked Ti:sapphire oscillator. M: cavity mirror, P: pump mirror, Pr: prism. The figure is taken from *Tsunami* user manual.

speed of light, meaning the time between the pulses is the time it takes for the pulse to make a complete round trip in the cavity and the pulse repetition rate is $\tau = 1/T = c/2L$. For a typical oscillator with a cavity length ∼2 m, the pulse separation is T=13.3 nm, and repetition rate τ= 75 MHz.

The mode-locking can be achieved by either passive mode-locking or active mode-locking. A commonly used device for passive mode-locking is a saturable absorber. The saturable absorber has intensity dependent transmission, which increases with laser intensity. When the light intensity is low, the saturable absorber will absorb all the light hitting on it; while when the light intensity is sufficiently high, the saturable absorber will be saturated and transmit the rest light. When placed in the cavity, for random phase state shown in Fig. 2.3(a), the peak intensity is small and cannot transmit the saturable absorber, therefore it prevents feedback of such states in the cavity. On the other hand, for the state with all modes in phase, it has sufficiently large peak intensity and will have very high transmittance through the saturable absorber. Therefore, such a mode-locked state is highly favorable and supported in the cavity. The output from such laser cavity with a saturable absorber is thus a pulsed laser. Except the saturable absorber, Kerr-lens is another device for passive mode-locking. A commonly

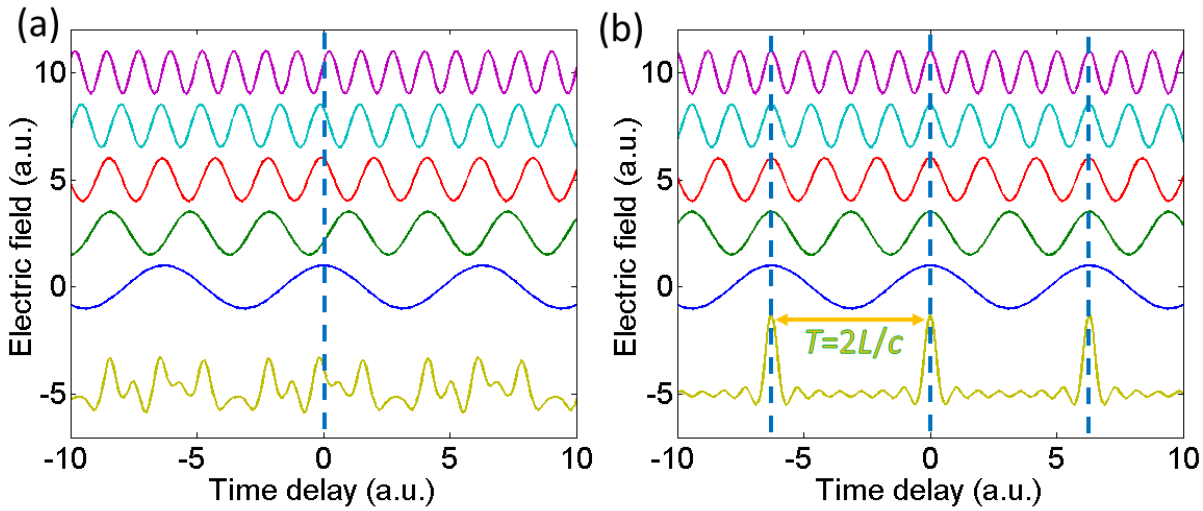

Figure 2.3 Schematic of temporal interference (not drawn to scale) of several electric field oscillations with various mode frequencies for (a) random phase state and (b) mode-locked state. The bottom field (yellow) is the sum of the various modes above it.

used active mode-locking device is the acousto-optic modulator (AOM). The AOM is made of high quality optical materials such as quartz. It is driven externally by, e.g., a radio-frequency transducer, which creates periodic sound waves in the AOM to modulate the material refractive index periodically. It therefore works as a diffractive grating to scatter incoming light to other directions. This prevents feedback of light in the cavity. If the modulator is turned off (to allow feedback) for an instant, the modes that can transmit the AOM at this instant must be in phase, because the modes out of phase will not be able to transmit, for when they arrive, the modulator is already turned on again (to prevent feedback). If the modulator is turned on and off at the frequency precisely matched to the pulse repetition rate $c/2L$, then a single mode-locked pulse of light will survive in the cavity. The output from such a laser cavity with an AOM is thus a pulsed laser. Except the AOM, other active mode-locking devices include Pockels cell, shutter, chopper, etc. As shown in Fig. 2.2, AOM is utilized in the oscillator as an active mode-locking element, which is externally driven by the Model 3955 module.

The wavelength and bandwidth selection of the oscillator output is realized by a prism sequence and an adjustable tuning slit shown in Fig. 2.2. The prism pairs disperse the light

wavelength spatially and a movable slit with adjustable width is located in the dispersed beam to select output wavelength and bandwidth. The prism pairs are also used to produce a net negative intracavity group velocity dispersion (GVD) to compensate the positive GVD introduced by the Ti:sapphire material and other optical materials in the cavity. The compressed pulse duration as short as 35-150 fs can be achieved depending on the cavity configurations.

The optional Model 3930 Lok-to-Clock Electronics module shown in Fig. 2.2 can be added to precisely compensate the cavity length change due to external environment variations in order for the laser to operate with lower timing jitter.

The output from our oscillator has 800 nm central wavelength with 60 nm bandwidth, 1 W average power, 13 nJ pulse energy, and 76 MHz repetition rate.

2.1.2 Ti:sapphire regenerative amplifier

Compared with cw laser beam, the pulsed laser output from an oscillator has much larger peak power and shorter duration, and it can be employed to study time-resolved dynamics. However, many scientific applications concerning nonlinear phenomena require even higher peak powers, so in order to induce strong nonlinear phenomena and study strongly photoexcited dynamics of materials, pulses from an oscillator need to be further amplified, by a Ti:sapphire regenerative amplifier in our case, which can amplify the pulse energy from nJ to mJ, by $\sim 10^6$ times!.

Due to extremely high peak power of amplified pulses, in order to get rid of optical damage of optical components induced by the amplified pulses, chirped pulse amplification is employed. The basic idea is shown in Fig. 2.4. The oscillator pulse duration is firstly stretched by a stretcher, composed of a pair of diffraction gratings, from tens of femtosecond (fs) to hundreds of picosecond (ps) and the peak power of the pulse is greatly reduced. Then the stretched pulse is amplified in the Ti:sapphire rod of the amplifier. After amplification, a compressor, composed of another pair of gratings, compresses the pulse to the initial pulse duration and the peak power is greatly increased.

The Ti:sapphire rod in the amplifier is pumped by Q-switched 527 nm green light with 1 kHz repetition rate, which is from the frequency doubling (by a non-critically phase-matched

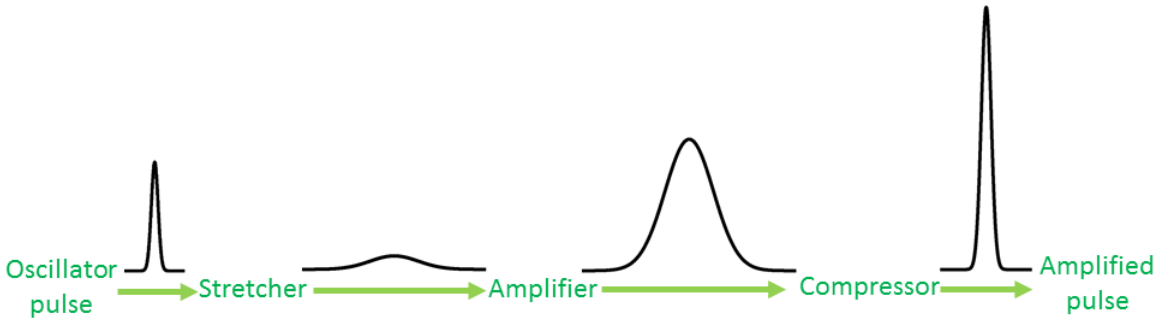

Figure 2.4 Schematic of the chirped pulse amplification. The oscillator pulse is firstly broadened by a stretcher to reduce the peak power, then amplified by an amplifier, and finally compressed back to the original pulse width by a compressor.

temperature-tuned LBO crystal) of 1053 nm radiation from neodymium-doped yttrium lithium fluoride (Nd:YLF) rod. One seed pulse per 1 ms is selected from the oscillator pulses for amplification in the cavity. Therefore, the pulse repetition rate is decreased from 76 MHz of the oscillator beam to 1 kHz of the amplifier beam. The injection of the seed pulse and ejection of the amplified pulse are accomplished by 2 electronically controlled Pockels cells by changing the polarization of the pulse. A trapped seed pulse will make ∼10 round trips in the cavity in order to fully use the gain in the Ti:sapphire rod, each time the pulse passing through the rod being amplified by a factor of 3-4. In our case, the output of the amplifier beam has 4 mJ pulse energy, 800 nm central wavelength with 40 nm bandwidth, 35 fs pulse duration (for the past a few years, the amplifier has been serviced many times. Sometimes, we ended with a bit larger pulse duration, e.g. 40-45 fs; If that is the case, we will indicate clearly; otherwise the pulse duration is 35 fs), and 1 kHz repetition rate.

2.1.3 Optical parametric amplifier

The output wavelengths of both oscillator and amplifier are centered at ∼800 nm with ∼40-60 nm bandwidth. Its application in many scientific researches which require more broadband and tunable light sources is very limited. This is fulfilled by the use of an optical parametric amplifier (OPA), which provides much broader bandwidth and tunability ranging from 500 nm to 20 μm.

The OPA is pumped by our 1 kHz Ti:sapphire amplifier centered at 800 nm. The optical parametric generation is a second-order nonlinear process in which a photon of a powerful pump pulse with frequency ω_p is converted into two photons with lower frequencies ω_s and ω_i, denoting signal and idler respectively, with the requirement $\omega_p=\omega_s+\omega_i$ as shown in Fig. 2.5 (left panel).

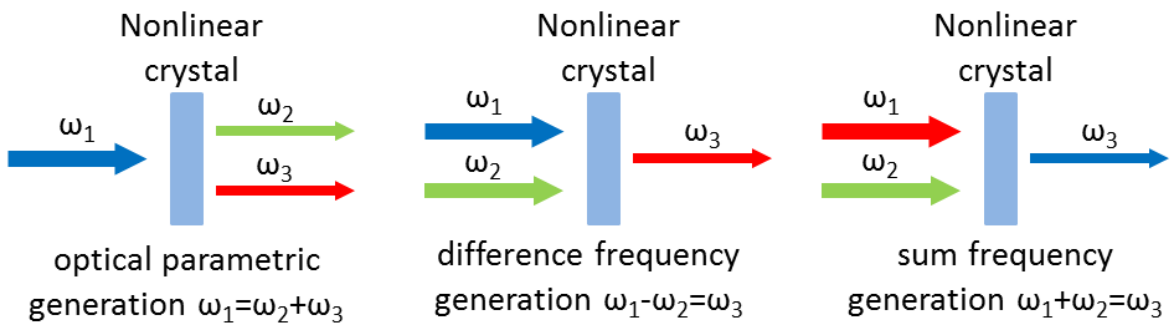

Figure 2.5 Illustration of several nonlinear processes. left: optical parametric generation; middle: difference frequency generation; right: sum frequency generation.

The pump wavelength is 800 nm. The signal and idler wavelengths can be tuned by changing phase-matching condition and temporal overlap of the pump pulse and a seed pulse as shown in Fig. 2.6. The seed pulse, very weak radiation of a white-light continuum (WLC), is generated by focusing a small portion of the amplifier beam into a sapphire crystal. The WLC, with super continuous bandwidth ~400 nm−1.6 μm, serves as the seed pulse and is present in the nonlinear crystal [bismuth triborate (BiBO)] simultaneously with the pump pulse that creates population inversion. The seed pulse, which induces stimulated emission in the crystal, is therefore amplified along the crystal length as it copropagates with the pump pulse. The signal pulse ω_s essentially originates from the amplified seed pulse ω_{seed} ($\omega_s=\omega_{seed}$). Also amplified in the process is the idler pulse (ω_i) when a pump photon is split into two.

The WLC has a pulse duration of ~2 ps and is dispersive temporally, so by changing the temporal delay of the 35 fs pump pulse and the 2 ps WLC pulse, the pump pulse can be chosen to overlap with a particular frequency of the WLC pulse ω_{seed}, and by properly tuning the phase-matching condition, ω_{seed} is amplified with optimal efficiency.

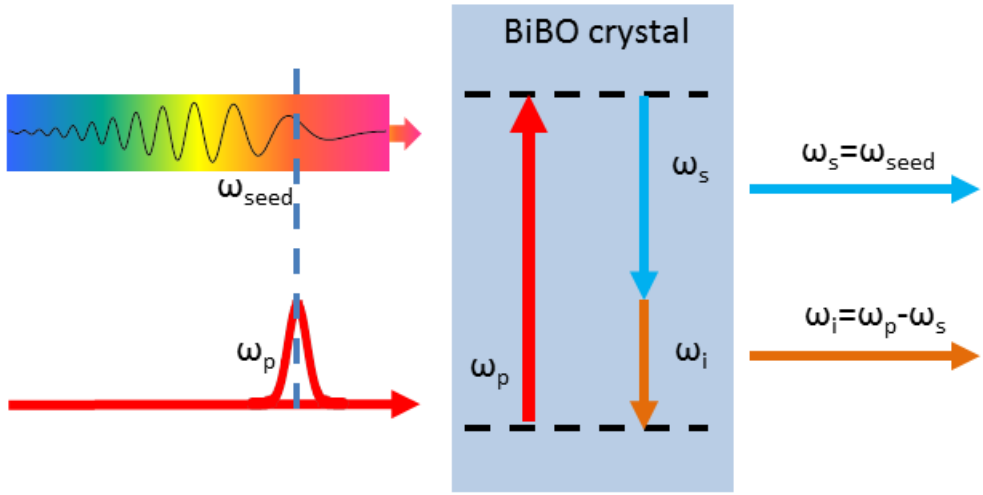

Figure 2.6 Schematic showing the temporal overlap of 800 nm pump pulse ω_{p} and the seed pulse ω_{seed} from the white light continuum. ω_{p} is converted into ω_{s} and ω_{i} in the parametric generation.

The tuning range of the signal wavelength in our OPA is about 1.1-1.9 μm and the idler wavelength is about 1.4-2.9 μm. The output power is a few mW, which is not sufficiently high for many scientific applications. Therefore, a second parametric amplification stage is employed to further amplify the signal and idler pulses. The second amplification mechanism is the same as the first stage as discussed above. Briefly, a pump pulse from the amplifier with much higher power and the signal pulse amplified in the first stage copropagate in the second BiBO crystal for amplification. The further amplified signal and idler pulses have a total power of ~800 mW. The output beam is a combination of many wavelengths, such as pump beam residue, signal, idler, SHG of them, etc. The pump beam can be blocked by using a longpass filter. The polarization of the idler pulse is the same as that of the pump beam, while the signal pulse has perpendicular polarization, therefore, the signal and idler pulses can be separated by using a polarizer or dichroic mirror.

The signal and idler pulses from the second stage can be employed for second harmonic generation (SHG) and sum frequency generation (SFG) in a β-barium-borate (BBO) crystal to produce wavelength covering the visible range, or for difference frequency generation (DFG) in a GaSe crystal to produce wavelength covering the Mid-Infrared (MIR) range, as shown in

Fig. 2.5. Therefore the OPA can produce broadband tunable wavelength from 500 nm to 20 μm, which suffices for many scientific studies.

2.2 Ultrafast Time-resolved Pump-probe Technique

Ultrafast laser pulses have sub-ps time duration. It can be used to study ultrafast phenomena which happen in sub-ps time scale, because the temporal resolution measured by such a pulse is essentially only limited by its time duration. Furthermore, because the energy is concentrated in such a ultrashort time period, the peak intensity is extremely high. For example, the output from our 35 fs amplifier pulse could reach a peak intensity of $\sim$100 GW. Such a big peak intensity can create many interesting nonlinear phenomena and extremely strong optical excitation in materials.

In order to probe photoexcited transient dynamics, the time-resolved pump-probe technique is used. The basic idea is shown in Fig. 2.7. A laser beam is split into two. One part (pump beam, red lines) passes through a delay stage, which is used to adjust the time delay relative to the other beam, and then illuminates the sample for photoexcitation. The other (probe beam, green lines) is sent into the sample to measure the photoexcited transient transmission or reflection (as shown in the dashed box) or polarization change. The temporal pump-probe delay $\Delta\tau$ of the 2 beams is adjusted by changing the optical path length by moving the delay stage. From the transmission and/or reflection and/or polarization measurements, we can study ultrafast phenomena happening in the sample. For example, the refractive index, conductivity, dielectric function, absorption coefficient, and others can be extracted from such measurements.

Note Fig. 2.7 just illustrates a basic idea of the technique. In actual experiments, the pump and probe beams are not necessarily split directly from the same pulse. It could be that one or both beams are from OPA or WLC or THz, or one beam from the oscillator and one beam from the amplifier, depending on the lab requirements. For THz spectroscopy measurement, the probe beam are THz pulses. The time-domain THz fields cannot be measured directly by a photodetector, instead, it is measured by electro-optic sampling of 800 nm sampling beam in a ZnTe crystal. The technique will be discussed in detail in next section.

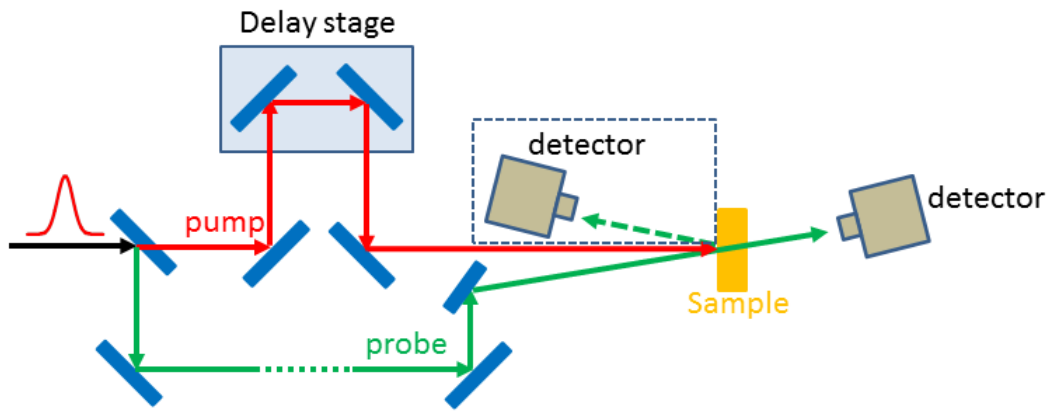

Figure 2.7 The basic scheme of the time-resolved pump-probe experiment. The pump beam excites the sample and the subsequent probe beam measures the transient transmission or reflection (shown in dashed box) or polarization change from the sample. The temporal pump-probe delay $\Delta\tau$ of the 2 beams is adjusted by the delay stage.

2.3 Ultrafast Terahertz Spectroscopy Experiment

2.3.1 Terahertz spectroscopy setup

Our ultrafast THz spectrometer is driven by the 1 kHz Ti:sapphire regenerative amplifier with 35 fs pulse duration and 800 nm central wavelength. One part of the output (2.7 W) is used to excite the sample directly or to pump the OPA to generate other wavelength ranging from 500 nm to 20 μm for excitation. Another part (200 mW) is used to generate THz field transients via optical rectification in a 1 mm thick $\langle 110 \rangle$ ZnTe crystal (in some other experiments, we also use other crystals like GaSe or 0.2 mm thick ZnTe to generate and detect THz). Another small part of the output (a few mW) is used to detect the phase-locked THz transients in time-domain via electro-optic sampling in a second 1 mm thick $\langle 110 \rangle$ oriented ZnTe crystal.

A schematic of the setup is shown in Fig. 2.8(a). A photo of the real setup in the purge box is shown in Fig. 2.8(b). The generation beam (red lines), after passing through a delay stage, illuminates the ZnTe emitter to generate THz radiation. A Teflon filter is then used to block the 800 nm generation beam and transmit THz beam. A 4-inch 90° off-axis parabolic mirror focuses the THz beam at the sample position with ∼2.5 mm focus diameter. A pump beam (dark red line), after passing by a delay stage and a ∼3 mm hole in the parabolic mirror, illuminates the sample for photoexcitation. A second 4-inch 90° off-axis parabolic mirror collimates the

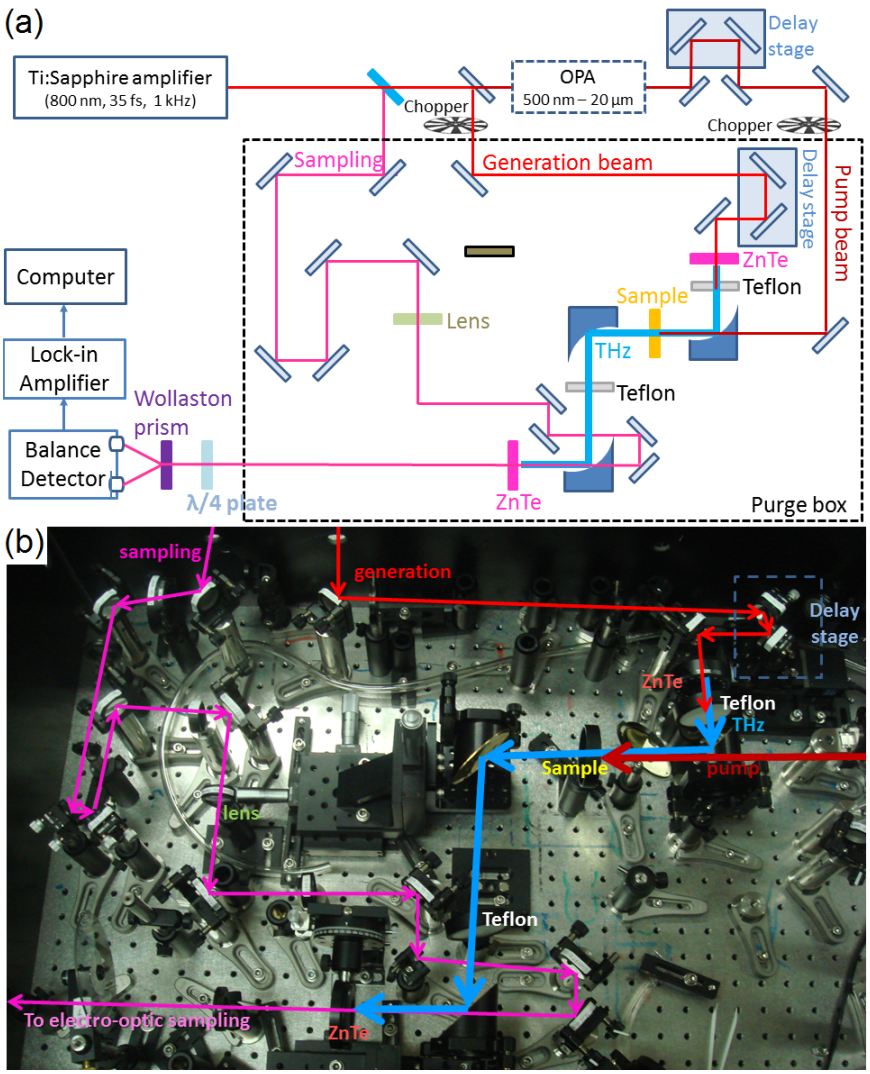

Figure 2.8 (a) Schematic of the THz time-domain spectrometer. (b) A photo of the real spectrometer in our lab. Only the parts in the purge box are shown.

THz beam, which is focused again by the third same type parabolic mirror onto the ZnTe detector. The sampling beam (pink lines) is softly focused by a 750 mm lens onto the ZnTe detector at the same position as the THz beam for electro-optic sampling. The second Teflon filter is used to block the back-reflection of the sampling beam from the ZnTe detector from hitting the sample from backside (it is also used to block the transmitted pump beam through the sample). The transmitted sampling beam is then sent into a polarization bridge composed of a quarter-wave plate, a Wollaston prism, and a balanced detector to detect the intensity difference of the vertical and horizontal polarizations. The output from the balance detector

is sent to an lock-in amplifier for signal amplification and noise rejection. A computer is used to collect and save the data from the lock-in amplifier. Two optical choppers are employed to assist data acquisition. One is used in the generation beam, while the other is used in the pump beam. For the static THz measurement (there is no pump yet), the chopper modulates the generation beam at 500 Hz and triggers the lock-in amplifier at the same frequency. The output from the lock-in amplifier measures the absolute static THz fields $E_{\mathrm{THz}}(t)$. And for photoexcited measurement, the chopper in pump beam modulates the pump pulses at 500 Hz and triggers the lock-in amplifier at 500 Hz. The output from the lock-in amplifier measures the pump-induced THz field change $\Delta E_{\mathrm{THz}}(t, \Delta\tau)$ at pump-probe delay $\Delta\tau$. The absolute THz field with photoexcitation can be obtained by $E'_{\mathrm{THz}}(t, \Delta\tau) = E_{\mathrm{THz}}(t) + \Delta E_{\mathrm{THz}}(t, \Delta\tau)$. Interesting physical parameters can be extracted after knowing $E_{\mathrm{THz}}(t)$ and $E'_{\mathrm{THz}}(t, \Delta\tau)$ as to be discussed later.

The sample is mounted behind a 2.5 mm diameter copper aperture. Another clear aperture with the same diameter is also mounted as a reference. The sample and reference sit on a 3D stage for precise position tuning (not shown in the photo). The sample and reference can also be mounted into a vacuum cryostat for low temperature experiment.

2.3.2 Terahertz generation and detection techniques

Compared with other frequency bands from radio waves to γ-rays, THz band is one of the least explored spectral ranges due to the lack of efficient and compact THz wave emitters and detectors for a long time. For the past years, a few approaches have been developed to generate and detect THz radiations either coherently or incoherently (although they are either weak or bulky or cannot operate at normal conditions), such as quantum-cascade lasers (QCLs) (1), photoconductive antennas (PCAs) (2), optical rectification (OR) (3), free electron lasers (FELs) (4), bolometers, pyroelectric detectors, etc. Some of them require low temperature to operate (QCLs, bolometers) and some are very bulky (FELs). The most popular table-top THz generation and detection techniques, although relatively low efficiency, are the OR and PCAs for generation and electro-optic sampling for detection. The techniques we use are the OR and electro-optic sampling, respectively.

The most popular nonlinear crystal for OR is the ZnTe. The structure of ZnTe is noncentrosymmetric and has no inversion symmetry, because Zn has a lower electronegativity than Te. Therefore, electrons are not evenly distributed between Zn and Te (5). When driven by an external electric field oscillation, the electrons experience asymmetric potential energy and have nonlinear motion. If the driving field is $E(t) = E_0 \exp(-a_0 t^2)\exp(-i\omega_0 t)$, the polarization of the electrons in ZnTe crystal induced by the driving field is

$$P(t) = \alpha E(t) + \chi^{(2)} E(t) E^*(t) + \text{higher orders.} \tag{2.1}$$

The first term of linear polarization is $P_{\text{Linear}}(t) = \alpha E(t)$, and the second-order nonlinear term is $P_{\text{NL}}(t) = \chi^{(2)} E(t) E^*(t)$. (The higher orders have much smaller efficiencies and will not contribute considerably in the case, so they can be neglected.) The second-order nonlinear efficiency $\chi^{(2)}$ is much smaller than the linear efficiency α, so when $E(t)$ is small, the linear effect dominates the nonlinear effect. But when $E(t)$ is very large, the nonlinear contribution cannot be neglected.

Assuming electrons oscillate around their mother atoms with the revised harmonic oscillator model including nonlinear response, the asymmetric potential energy of electrons is given as $U(x) = \frac{1}{2}k_0 x^2 + \frac{1}{3}kx^3$, where $k_0 = m\omega_0^2$. The polarization can be expressed as in Fig. 2.9. The total polarization $P(t)$ (red) is composed of 2 components: linear polarization $P_{\text{Linear}}(t)$ (dashed green, oscillating with the same frequency as the driving frequency ω_0), and nonlinear polarization $P_{\text{NL}}(t)$ (dashed blue). The linear polarization is nothing interesting. It will radiate electromagnetic waves at the same frequency as the driving field (ω_0) with delayed phase. The nonlinear polarization can be further divided into 2 components as shown in the bottom panel. One (solid blue) is linear oscillation but with twice driving frequency ($2\omega_0$). This component is the source of the SHG; the other (dashed blue) is a constant rectified polarization from OR, the amplitude of which is proportional to $P_{\text{NL}}(t) = \chi^{(2)} E_0^2 \exp(-2a_0 t^2)$, i.e., the rectified second-order nonlinear polarization follows the driving field envelop. For a typical 35 fs laser pulses, the pulse envelop has bandwidth ~12.6 THz, calculated from the transform-limited relation $\Delta v \cdot \tau_{\text{p}}$=0.44, where Δv is the bandwidth and τ_{p} is pulse duration. Therefore, the electromagnetic radiation from OR of a fs laser pulse is in THz range!

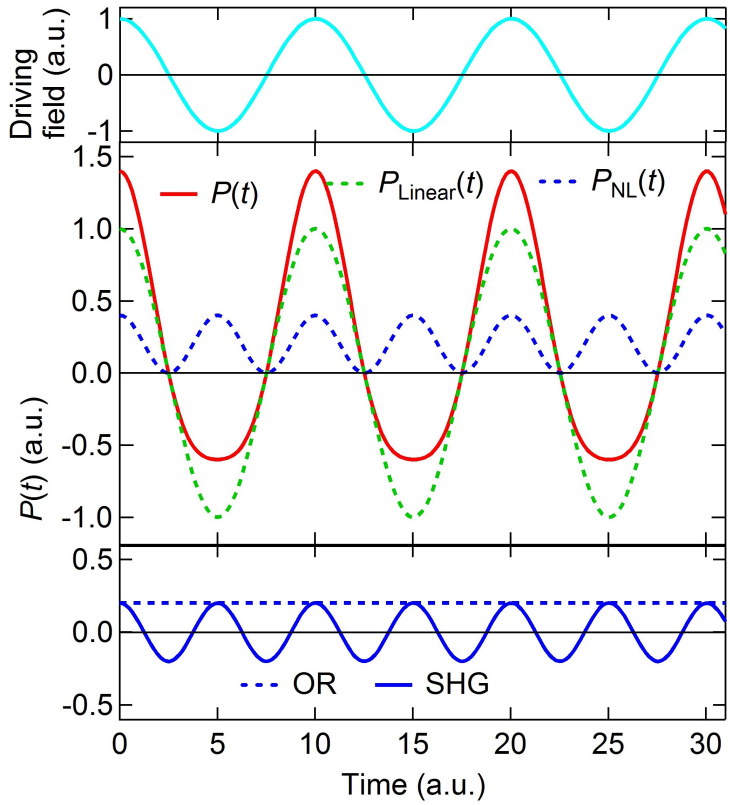

Figure 2.9 Top panel: an external driving electric field with frequency ω_0. Middle panel: polarization of electrons in a noncentrosymmetric medium driven by the external field. The total polarization (red) is composed of a linear component (dashed green) and a nonlinear component (dashed blue). Bottom panel: the nonlinear component (dashed blue) can be further divided into a linear component but with twice the driving frequency: $2\omega_0$ (solid blue) and a constant component (dashed blue).

The ZnTe crystal structure is shown in Fig. 2.10(a). In order to generate most efficient THz from ZnTe, the optical pulse polarization need to be parallel to the chemical bonds between Zn and Te. This requires ZnTe crystal to be $\langle 110 \rangle$ cut and the angle between the optical pulse and the ZnTe [001] axis θ to be 55° as shown in Fig. 2.10(b). The generated THz intensity as a function θ is shown in Fig. 2.10(c). The angle between the optical pulse polarization and the generated THz pulse polarization as a function of θ is shown in Fig. 2.10(d). Clearly, θ=55° yields maximum THz radiation and the THz polarization is antiparallel to the optical pulse. When θ=0 or 180°, there is minimum THz generation. When θ=90°, THz intensity is about 80% of the maximum generation and the THz polarization is perpendicular to the optical pulse.

From θ=0 to 55°, the THz polarization changes from perpendicular to antiparallel gradually. This feature can be used to tune the generated THz polarization.

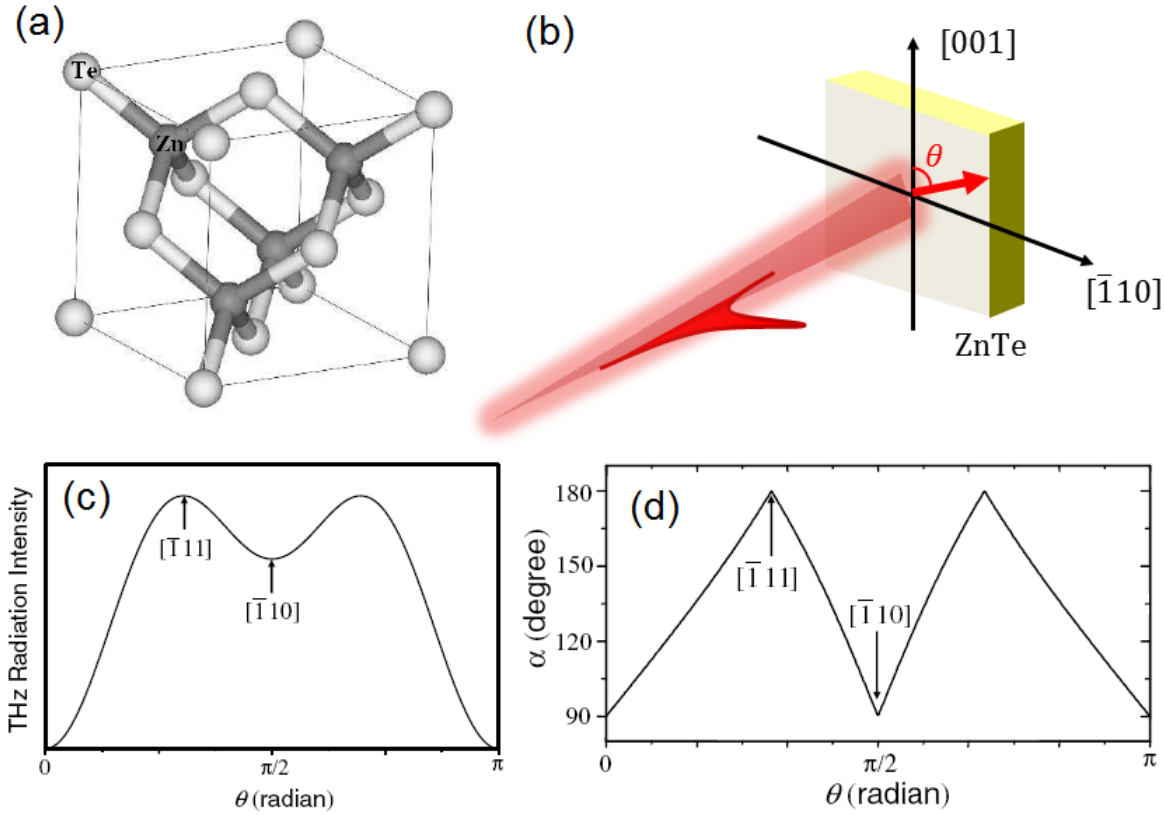

Figure 2.10 (a) The ZnTe crystal structure. (b) An optical pulse illuminates the $\langle 110 \rangle$ cut ZnTe. The angle between the polarization of the pulse and the [001] axis is θ. (c) The generated THz intensity as a function of θ. (d) The angle between the optical pulse polarization and generated THz pulse polarization as a function of θ. The figures (a)(c)(d) are taken from Ref (5).

For THz detection by electro-optic sampling, it measures coherently the THz electric field in time-domain. Therefore, unlike incoherent detection from a bolometer or pyroelectric detector, the electro-optic sampling can measure both the THz field amplitude and phase. The THz pulse duration usually is a few ps, but the sampling beam pulse duration, which determines the temporal resolution, needs to be as short as possible. Depending on the desired detection bandwidth, it needs to be shorter than $\tau_{\mathrm{p}} = 0.44/\Delta v$. The electro-optic sampling technique is illustrated in Fig. 2.11. The electro-optic detection mechanism employs the Pockels effect in ZnTe. When there is no THz field in presence, the sampling pulse does not change polarization

after going through ZnTe. Afterwards, the polarization is changed from linear to circular by a quarter-wave plate. Next, a Wollaston prism separates vertical and horizontal polarizations, which are equal in the case. Therefore the signal measured by the balance detector is $I_{\text{signal}} = I_1 - I_2$=0. On the other hand, when THz field is present and copropagates with the sampling beam in the ZnTe crystal, the sampling beam polarization changes a little after going through the ZnTe crystal, due to the THz field induced birefringence in the ZnTe which is linearly proportional to the THz field strength. Therefore, the sampling polarization is elliptical (close to circular) after the quarter-wave plate. The signal measured by the balance detector in this case is not equal: $I_{\text{signal}} = I_1 - I_2 = I\Delta\varphi$, where I is the intensity of the sampling beam and $\Delta\varphi$ is the phase retardation of the 2 perpendicular polarizations of the sampling beam after traveling through the ZnTe crystal. $\Delta\varphi$ can be calculated as (6)

$$\Delta\varphi = (n_1 - n_2)\omega L/c = \omega L n_o^3 r_{41} E_{\text{THz}}/c, \tag{2.2}$$

where n_o is the refractive index of the sampling beam in ZnTe, r_{41} the electro-optic coefficient (=4 pm/V for ZnTe), L the thickness of the ZnTe crystal. Clearly, the signal measured by the balance detector I_{signal} is linearly proportional to the THz field strength E_{THz}.

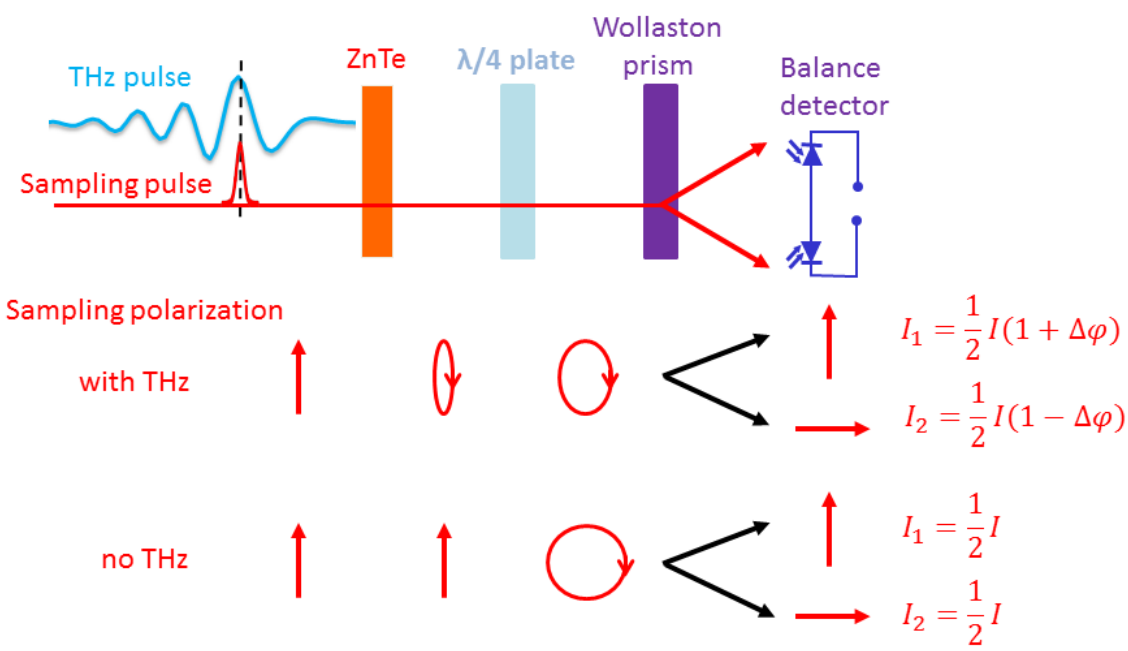

Figure 2.11 Schematic showing the electro-optic sampling technique.

The detection polarization relations between the sampling beam, THz, and ZnTe are more complex. The detail of the study is presented in (7). Here I will just summarize the conclusion in Fig. 2.12. The ZnTe crystal is still ⟨110⟩ cut. The relations of THz polarization E_{THz}, THz wavevector k_{THz}, the sampling beam polarization E_{p}, sampling beam wavevector k_{p}, and their angles relative to ZnTe [001] axis are shown in Fig. 2.12(a). The measured THz electric field amplitude as a function of angles are shown in Fig. 2.12(b). Clearly, both perpendicular and parallel polarizations between the THz and sampling beams can yield maximum THz detection efficiency. For example, when THz and sampling beams are parallel, THz field being perpendicular to [001] axis gives the maximum efficiency.

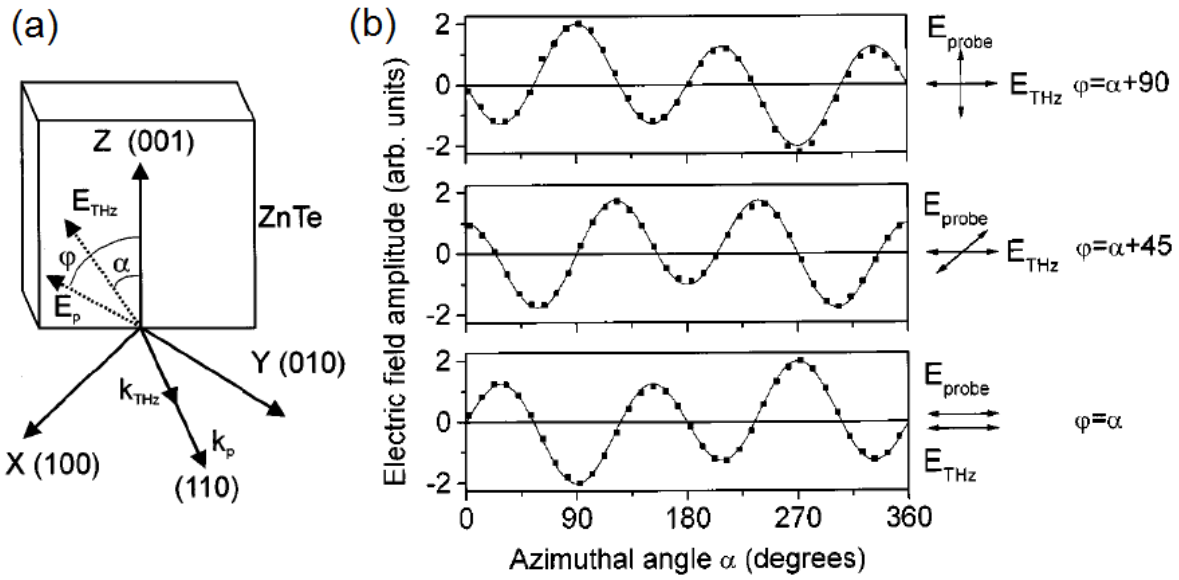

Figure 2.12 (a) The angles of THz beam E_{THz} and sampling beam E_{p} relative to the ZnTe [001] axis. Both THz and sampling beams are perpendicular to the ⟨110⟩ cut ZnTe surface. (b) measured THz electric field amplitude as a function of the angles. The figure is taken from (7).

2.3.3 Terahertz data analysis

The typical time-domain THz fields from the ZnTe emitter and detector are shown in Fig. 2.13(a). The green line is the THz time-domain field $[E_{\mathrm{ref}}(t)]$ transmitted through a 2.5 mm diameter copper clear aperture. The blue line is the THz field $[E_{\mathrm{THz}}(t)]$ transmitted through a 0.51 mm thick GaAs wafer which is mounted behind the other 2.5 mm copper aperture.

The red line is the pump-induced THz field change [$\Delta E_{\mathrm{ref}}(t)$] through photoexcited GaAs after some pump-probe delay time $\Delta\tau$ which can be precisely controlled by the delay stage. The THz field transmitted through the static GaAs wafer (blue) has smaller amplitude and ~4.5 ps time delay relative to that through the clear aperture (green). This can be understood as the partial reflection of the THz field on the air-GaAs surfaces and the extra time it takes for THz to travel in GaAs with refractive index (n_{GaAs} ~3.6) larger than that in air (n_{air}=1). The corresponding THz spectra transmitted through clear aperture, static, and photoexcited GaAs are shown in Fig. 2.13(b), which shows clearly the finite spectrum ranging from 0.5-2.5 THz, which is a typical range for 1 mm thick ZnTe crystals.

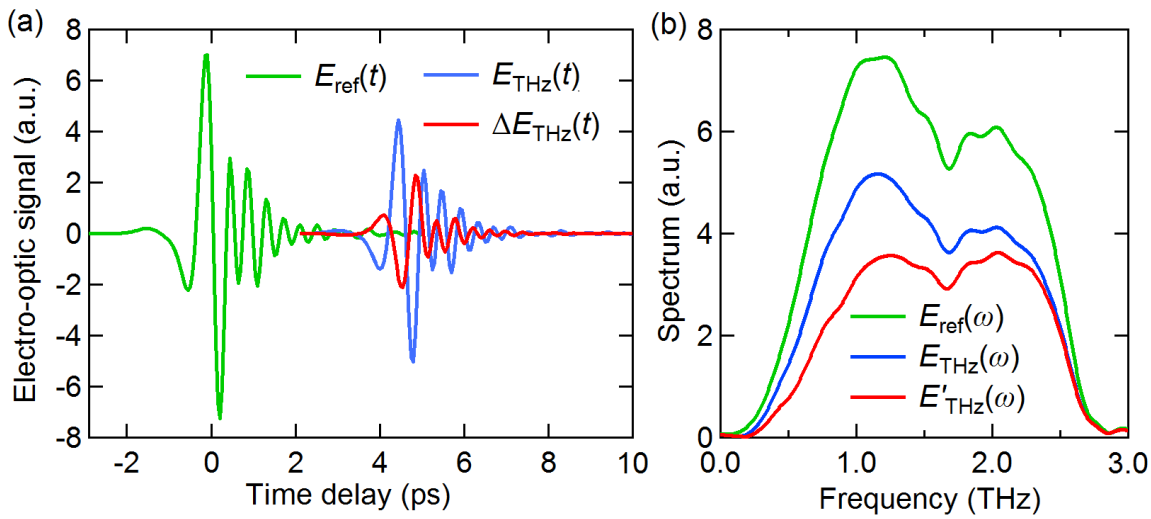

Figure 2.13 (a) The THz time-domain fields transmitted through a 2.5 mm copper clear aperture ($E_{\mathrm{ref}}(t)$, green) and a GaAs wafer mounted behind another 2.5 mm copper aperture ($E_{\mathrm{THz}}(t)$, blue), and its pump-induced field change ($\Delta E_{\mathrm{THz}}(t)$, red). (b) The corresponding THz spectra transmitted through clear aperture ($E_{\mathrm{ref}}(\omega)$, green), static GaAs ($E_{\mathrm{THz}}(\omega)$, blue), and photoexcited GaAs ($E'_{\mathrm{THz}}(\omega)$, red).

By comparing the THz spectra through reference (a clear aperture), static, and excited sample, we can extract a lot of useful information of the sample. Specifically, we determine temporal evolution of the THz conductivity in the photoexcited sample. The phase-sensitive nature of the time-domain THz spectroscopy technique can directly yield both real and imaginary parts of the conductivity and dielectric function on equal footing without the use of Kramers-Kronig relations. Quantitatively, through the fast Fourier transformation and Fresnel equation, the

complex-valued static transmission is calculated as $T(\omega) = E_{\mathrm{THz}}(\omega)/E_{\mathrm{ref}}(\omega)$, from where the complex-valued static refractive index $\widetilde{n}(\omega)$, dielectric function $\widetilde{\varepsilon}(\omega) = \widetilde{n}^2(\omega)$, and conductivity $\widetilde{\sigma}(\omega) = \omega[1 - \widetilde{\varepsilon}(\omega)]\varepsilon_0 i$ are obtained. Next, from photoexcited THz measurement, the transient transmission after pump-probe delay $\Delta\tau$ is obtained: $T^{'}(\omega) = [E_{\mathrm{THz}}(\omega) + \Delta E_{\mathrm{THz}}(\omega)]/E_{\mathrm{ref}}(\omega) = E^{'}_{\mathrm{THz}}(\omega)/E_{\mathrm{ref}}(\omega)$, which yields the transient conductivity change $\Delta\widetilde{\sigma}(\omega) = \widetilde{\sigma}^{'}(\omega) - \widetilde{\sigma}(\omega)$ and dielectric function change $\Delta\widetilde{\varepsilon}(\omega) = \widetilde{\varepsilon}^{'}(\omega) - \widetilde{\varepsilon}(\omega)$, where the primed parameters are for photoexcited cases. Other parameters such as wave vector $\widetilde{k} = \widetilde{n}\omega/c = k_1 + ik_2$, absorption coefficient $\alpha = 2k_2$, and penetration depth $\delta = 1/\alpha$ could also be obtained. From these results we can learn important physics happening, such as carrier formation, relaxation, transportation, carrier and phase transitions, etc.

For samples with very low THz transmission, reflected THz fields in time-domain are measured instead of transmitted fields. In such a case, the reference will be a gold mirror instead of a clear aperture for transmission. By using the fast Fourier transformation and Fresnel equation, the above mentioned parameters can be similarly calculated.

CHAPTER 3. TERAHERTZ WAVE GENERATION FROM SPLIT-RING-RESONANTOR METAMATERIALS

In this chapter, we demonstrate efficient THz emission up to 4 THz from optical rectification in a single layer of 40 nm thick gold film of split-ring-resonator (SRR) metamaterials, based on resonant photoexcitation of the magnetic-dipole resonance centered at 1500 nm wavelength using 140 fs laser pulse. The strong THz emission intensity from the SRR emitter is on the same order as optimal ZnTe crystals that are thousands times thicker, revealing a gigantic resonant second-order sheet nonlinear susceptibility of SRRs $\sim 10^{-16}$ m^2/V, which is three orders of magnitude higher than the typical surface and sheet values of bulk crystals and thin films. The THz bandwidth from the SRR emitter is only limited by the pump pulse duration. Our approach could generate broadband gapless THz waves covering the entire THz band by using shorter pump pulse.

Specifically, this chapter starts with an introduction to the metamaterials and the current situations of THz generation and detection techniques, which also point out our motivation for this project. Secondly, the SRR emitter fabrication information is provided. Next I will present in detail the experiment setup and the characterizations of the SRR emitter by various measurements (e.g., power-dependent, wavelength-dependent, polarization-dependent, etc.). The second-order nonlinear susceptibility of the emitter is also calculated. Then, theoretical explanation of the THz emission mechanism is discussed. Finally, this chapter ends with a brief summary of current project and an outlook for future direction.

This chapter is largely based on the paper that is published in *Nature Communications* **5**, 3055 (2014).

3.1 Introduction

3.1.1 Metamaterials

Metamaterials are artificially structured materials with exotic properties that do not exist in natural materials (8). Some of their unique properties include the negative refractive index (9) and diffraction-free superlens (8). Additionally, they can be used as photonic elements to control light waves. The potential applications include light source, electromagnetic wave modulation, remote sensing, communications, ultrasonic sensors, antennas, cloaking devices, etc.

Usually metamaterials are made from a group of periodically arranged unit cells on substrates. The unit cell itself is made from conventional materials such as metals . The unit cell size is normally smaller than the light wavelengths it is designed to work with. The metamaterials properties are not mainly determined by the materials they are made from, but from the unit cell geometry, shape, size and orientation, etc. One typical unit cell structure of metamaterials is the split-ring-resonator (SRR) as shown in Fig. 3.1. The SRR unit cell can be made from metals such as gold, silver, copper, etc. The substrate materials can be insulators (glass) or semiconductors (GaAs, Si). The unit cell lattice constant, depending on the applications, usually ranges from hundreds of nm to mm.

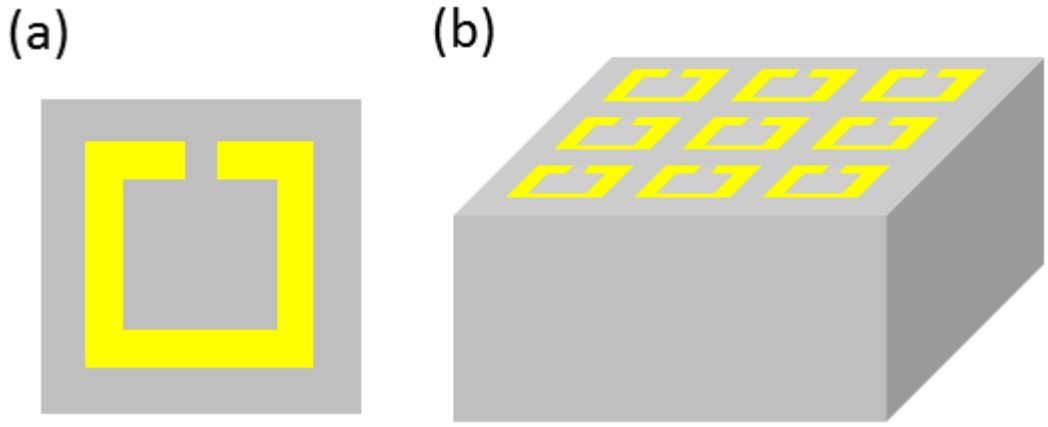

Figure 3.1 (a) Schematic of the SRR unit cell. (b) The SRR array on a substrate. The SRR unit cell materials can be metals such as gold, silver, copper, etc. The substrate materials can be insulators (glass) or semiconductors (GaAs, Si).

Except the simplest SRR structure, some other more complex structures include fishnet, chiral, cubic, spheric, and 3D structures (10).

3.1.2 Motivations

The THz spectral regime, ranging from about 0.1 to 15 THz, is one of the least explored yet most technologically transformative spectral regions. One current challenge is to develop efficient and compact THz emitters/detectors with a broadband and gapless spectrum that can be tailored for various pump photon energies. However, the challenge merges different disciplines of fundamental science and technology, ranging from ultrafast nonlinear optics, condensed matter and materials physics to optoelectronics and microwave photonics. The emerging THz technologies, such as quantum-cascade lasers (1; 11; 12), ultrafast photoconductive switches (2), have enabled various THz spectroscopy/imaging/sensing developments and have offered perspectives, amongst others, for pushing the GHz switching speed limit of todays logic/memory/wireless communication devices into the THz regime (2; 13).

In regard to broadband THz sources, a major recent progress (3) is based on nonlinear optical rectification in inorganic crystals such as ZnTe/GaP/GaAs/GaSe/DAST/$LiNbO_3$, pumped by femtosecond laser pulses combined with field-resolved detection via electro-optic sampling using similar crystals. However, issues in these crystals are: strongly absorbing longitudinal optical phonon bands that lead to a gap in the THz spectrum in the Reststrahlen region; subtle quasi-phase-matching conditions that require locking phase velocity of the THz emission to group velocity of the optical pump, which restricts the accessible pump photon energies to a fixed and narrow range in order to increase the coherent length.

Recently, there have been efforts on thin THz emitter/detector crystals of 10-30 μm thickness (3; 14) to increase the THz emission bandwidth by leveraging above-mentioned restrictions and to enable integration with current micro-/opto-electronics technology. However, the relatively small nonlinear susceptibilities of inorganic emitters limit the THz emission intensity.

Some other nonlinear media have also been explored although they mostly suffer from either poor stability or limited bandwidth, e.g., the ambient air-plasma generation normally with large shot-by-shot fluctuations (15; 16), and electrically-biased photoconductive antenna

that not only requires extra voltage driving source but also has limited bandwidth (17), e.g., some substrate materials such as GaAs still have strong TO and LO phonon resonances at 8.1 and 8.8 THz, which limits the THz radiation in this range (5). The same narrow THz emission bandwidth has also been seen from the fs-laser-accelerated photoelectrons in nano-plasmonic structures (18; 19).

Meanwhile, nonlinear metamaterials have been actively pursued (9; 20; 21; 22; 23; 24; 25; 26; 27) and recently the development of metamaterials composed of SRRs has enabled researchers to tailor resonant optical nonlinearities from the THz to the infrared and visible regions (8; 10). In this regard, investigating single nm thickness metamaterials exhibiting artificial optical magnetism i.e., sustaining circulating ring currents at optical frequencies can meet the urgent demand for new nonlinear materials for optical rectification free from both quasi-phase-matching limitation and spurious THz phonon absorption. This is mainly due to the coexistence of resonant nonlinearity (28; 29; 30) from magnetic dipoles and local electric-field enhancement in the narrow gaps of the SRRs, which together allows efficient and broadband THz radiation from emitters of significantly reduced thickness. In addition, tailoring the magnetic resonances of the metamaterial emitters allows for matching to essentially any desired pump photon energy. For example, this allows for integrating THz optoelectronics with high-speed telecommunications as the 1.3-1.5 μm range is not ideal for the above inorganic crystals.

3.2 Sample Preparation and Characterization

The SRR sample has been fabricated using electron-beam lithography and high-vacuum evaporation of gold, followed by a lift-off procedure. The sample is composed of a single layer of 40 nm thin gold film of SRRs with a square lattice constant of 382 nm on a 1 mm thick suprasil substrate coated with a 5 nm thick ITO layer that serves to prevent distortion due to local charge accumulation during the electron-beam lithography. As shown in Fig. 3.2(a), the big yellow SRR on the left illustrates the geometrical parameters used for the numerical calculations. Three small yellow SRRs are overlaid in the middle of SRR array micrograph on the right in order to compare the designed SRR geometry with the actual fabricated SRR dimension.

The SRR exhibits two resonances as shown in Fig. 3.2(b). The electric-dipole resonance (red curve) is centered at 800 nm and the magnetic-dipole resonance (black curve) is centered at 1500 nm. They are measured with the polarization of the incident light either perpendicular (electric) or parallel (magnetic) to the gap of the SRRs respectively.

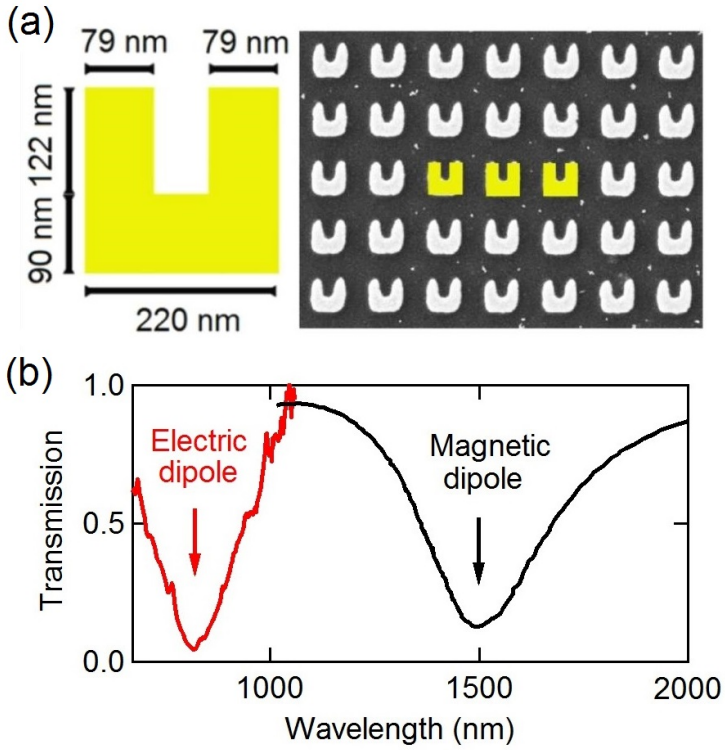

Figure 3.2 (a) The design dimension of the SRR (left) and electron micrograph of the actual SRR array (right) with three designed yellow SRRs overlaid in the middle to compare the designed and actual dimensions. (b) The linear optical transmission showing electric (red curve) and magnetic (black curve) dipole resonances of the SRRs. It is also plotted in the inset of Fig. 3.4 for easy reference.

3.3 Experimental Setup

Figure 3.3 schematically illustrates the experimental setup and shows key elements. A Ti:sapphire amplifier is used to drive the whole setup with central wavelength 800 nm, pulse duration 35 fs and repetition rate 1 kHz. The main portion of the output from the amplifier is used to pump an optical parametric amplifier (OPA) to produce tunable near-infrared (NIR) radiation from 1100 to 2600 nm of about 140 fs pulse duration. The NIR radiation from the

OPA is used as a generation beam to pump the SRR emitter. The FWHM of the NIR beam size is ∼4 mm. Therefore, 1 μJ pulse energy corresponds to the fluence of 8 μJ/cm^2 and a peak intensity of 5.7×10^7 W/cm^2. The generated THz pulses are focused onto a ZnTe or GaSe crystal by a parabolic mirror for electro-optic sampling by a small portion of the amplifier output. A wire grid polarizer is used to measure the polarization of the generated THz pulses (note the wire grid polarizer is used only for the determination of the polarization and not used for all the other experiments). The THz section of the setup is purged with dry N_2 gas.

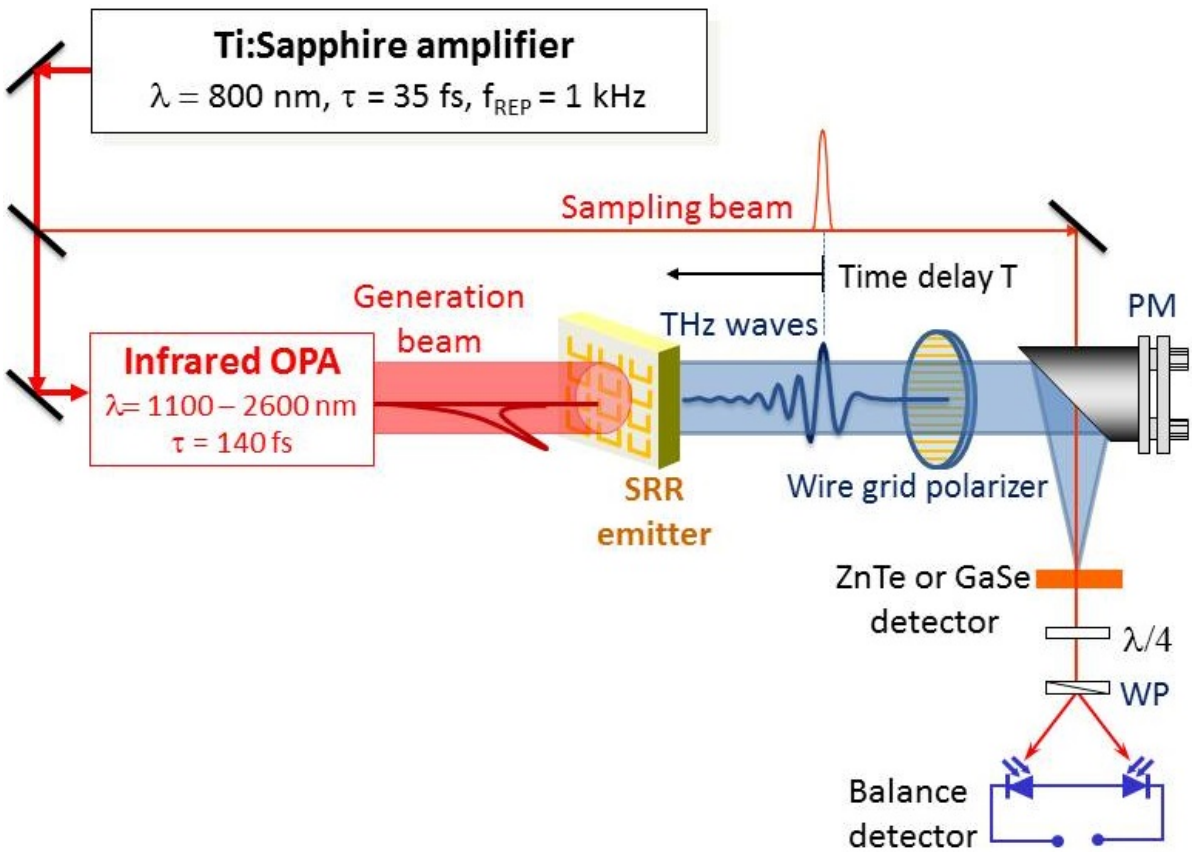

Figure 3.3 Schematics of THz generation and detection setup. PM: parabolic mirror, WP: Wollaston prism.

3.4 Experimental Results

3.4.1 Terahertz emission from pumping electric- and magnetic-dipole resonances

Typical time-domain THz traces, E_{THz}, during the 4-ps interval and for a pump fluence of 200 μJ/cm^2, are shown in Fig. 3.4 for two pump wavelengths: this clearly demonstrates THz generation is exclusively from pumping at the SRR magnetic-dipole resonance with 1500 nm (black dots), while there is negligible THz signal from pumping at the electric-dipole resonance with 800 nm (red line) and pumping the bare substrate with 1500 nm (green line). The two resonances are excited with the linear polarization of the incident pump light either perpendicular (electric) or parallel (magnetic) to the gap of SRRs. In addition, we characterize the polarization state of the emitted THz pulses to be perpendicular to the gap of the SRRs, consistent with the second-order nonlinearity.

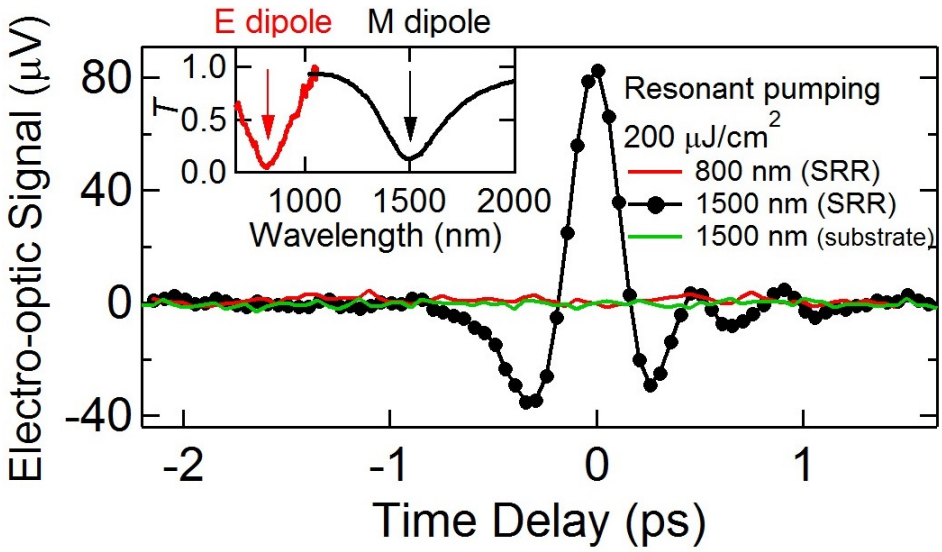

Figure 3.4 Measured THz time-domain signals by pumping the SRR electric-dipole resonance (red line) at 800 nm, magnetic-dipole resonance (black dots) at 1500 nm and pure substrate (green line) at 1500 nm, respectively. The inset is reproduced from Fig. 3.2(b) showing electric (red curve) and magnetic (black curve) dipole resonances of the SRRs.

3.4.2 Pump wavelength dependence of THz generation

To further investigate the nature of the THz emission, a 2D false-color plot and the time-domain THz traces in Fig. 3.5 show the detailed excitation-wavelength dependence. Resonant photoexcitation of the magnetic-dipole resonance near 1500 nm leads to significant enhancement of the THz emission, as shown in Fig. 3.5(a). The corresponding time-domain trace for the on-resonance pumping is plotted in Fig. 3.5(c). The conversion efficiency quickly decreases under off-resonance pumping, which is shown by the reduction of the THz emission for excitation both below and above the magnetic-dipole resonance, at 2180 nm [Fig. 3.5(b)] and 1376 nm wavelengths [Fig. 3.5(d)], respectively. The peak-to-peak amplitudes of THz emission ΔE_{THz} (red diamonds) closely follow the absorption around the magnetic-dipole resonance, as seen by comparison with the 1-T curve [blue, left side panel, Fig. 3.5(a)], where T is the linear optical transmission of the sample. All of these observations corroborate the resonant THz generation from nonlinear currents induced by the electrically coupled fundamental magnetic SRR resonance.

3.4.3 Polarization dependence of THz generation

Figure 3.6 shows the control of the amplitude and phase of THz emission by varying relative polarization by rotating the SRR emitter. As shown in the inset of Fig. 3.6(b), we define the polarization angle to be 0 degree when the polarization of the pump beam is parallel to the gap of the SRR and 90 degrees for the orthogonal polarization. Fig. 3.6(a) plots 7 traces by varying the SRR emitter from 0 to 180 degree under 1500 nm pumping (traces are offset for clarity). It clearly shows that the THz emission amplitude oscillates starting from a maximum at 0 degree, crosses zero at 90 degrees and returns back to a maximum at 180 degrees with a π phase shift from the origin. The complete polarization dependence of the emission amplitude is shown as a polar graph in Fig. 3.6(b) where the peak-to-peak amplitude of THz signal is plotted as a function of the rotation angle. The amplitude is best fitted with a $\cos^3(\theta)$ function, where a $\cos^2(\theta)$ dependence is from the polarization between the pump beam and the gap of the SRR, and the other $\cos(\theta)$ originates from the detection ZnTe crystal. In short, the ZnTe detector

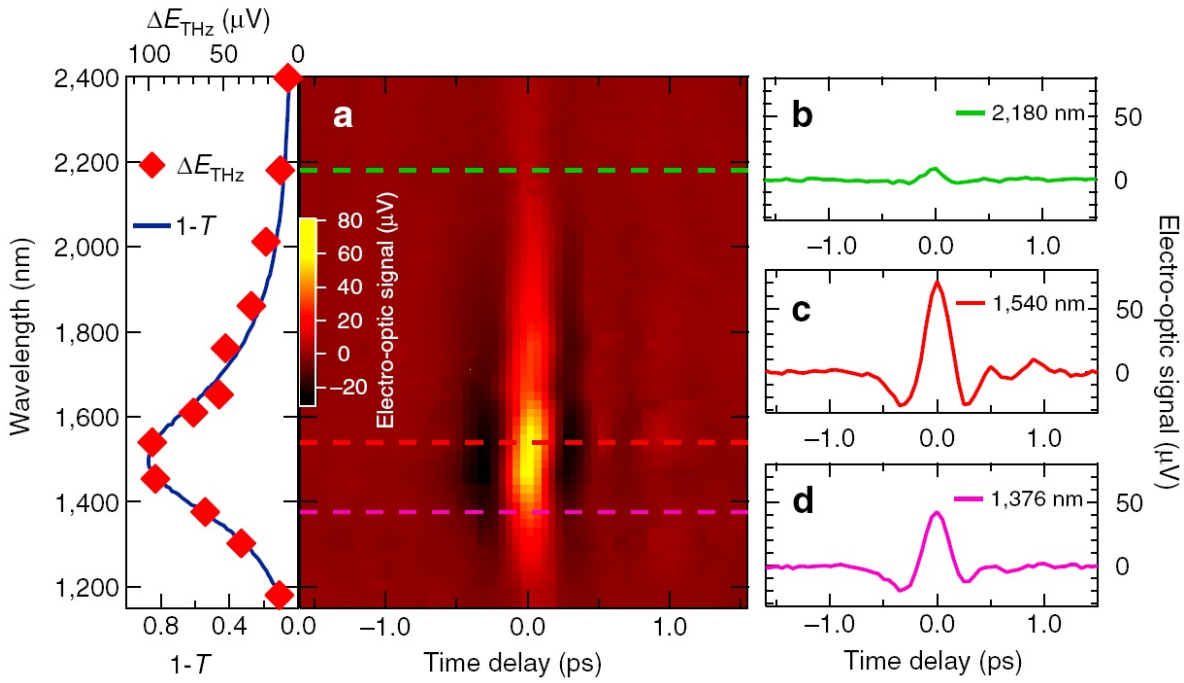

Figure 3.5 Pump wavelength dependence of THz generation from the SRR emitter. (a) A 2D false-color plot of the THz temporal traces for sweeping the pump wavelength across the magnetic-dipole resonance from 1180 to 2400 nm. The left-hand-side panel summarizes peak-to-peak amplitudes of THz emission (red diamonds) as a function of pump wavelength, together with the 1-T curve (blue solid line). T is the measured transmission around the SRR's magnetic-dipole resonance. The three colored curves (green, red, magenta) indicate the cut positions of three time–domain traces shown in (b-d) corresponding to 2180 nm, 1540 nm and 1376 nm, respectively.

is aligned such that it measures vertically (horizontally) polarized THz pulses at maximum (minimum) efficiency and the efficiency follows a $\cos(\theta)$ function (7).

3.4.4 Comparison of SRRs with other emitters

Figure 3.7 compares the peak-to-peak amplitude of THz electric field ΔE_{THz} versus pump energy for the SRR emitter (blue squares) with two ZnTe emitters with thicknesses of 1 mm (red diamonds) and 0.2 mm (magenta dots), respectively. The THz signals for the three emitters are measured at the same pump energy and using the same ZnTe detector crystal of 1 mm thickness. For the ZnTe emitters pumped at 1500 nm, the coherence length L_{c} for the THz

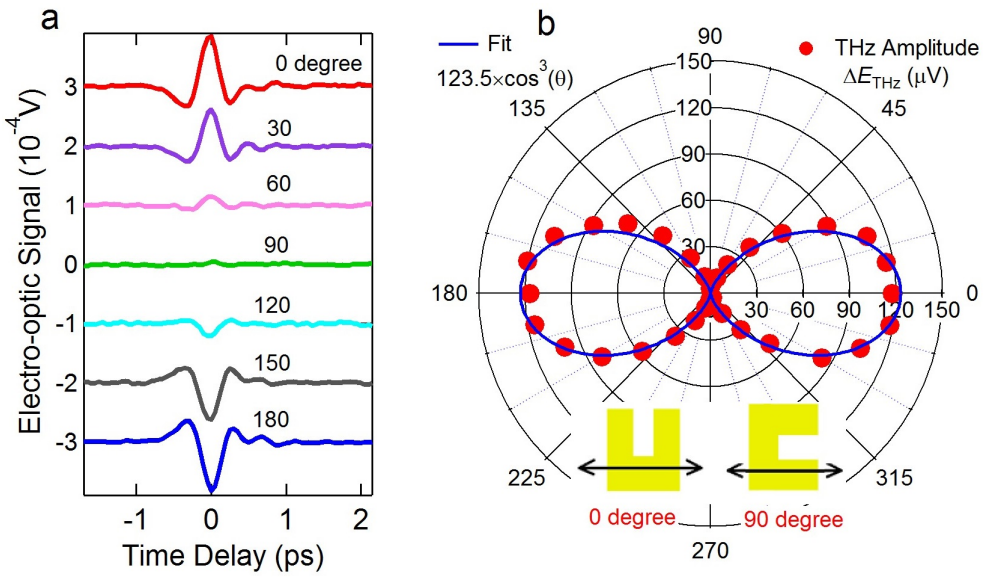

Figure 3.6 (a) The THz signals measured at several angles between the polarization of 1500 nm pump beam and the gaps of SRRs. The traces are offset for clarity. (b) The polar graph of the peak-to-peak amplitudes of THz signals as a function of the SRR emitter rotation angle. The inset defines the angles between the polarization of the 1500 nm pump beam (black arrows) and the SRRs.

emission is $\sim$ 0.2 mm (5). Increasing the crystal thickness beyond this value actually decreases the emission intensity, as seen for the 1 mm ZnTe case. This effect is expected from the quasi-phase-matching in the ZnTe emitter crystal: after propagating L_c, the superposition of the emitted THz pulses from different sheets will have destructive interference in the ZnTe. Most intriguingly, Fig. 3.7 reveals a remarkably efficient THz generation from the 40 nm thick SRRs with emission intensity on the same order as the optimal ZnTe emitters of 5000 times thicker: the SRRs generate THz radiation approximately 1/5 of the maximum from the 0.2 mm ZnTe. The emitted THz electric field scales linearly with the pump energy, which corroborates the optical rectification process. Our phase-resolved THz measurements from the SRR and ZnTe emitters allow us to unambiguously determine the second-order nonlinear susceptibility of the 40 nm thick single layer SRR emitter to be $0.8\times10^{16}\mathrm{m}^2\mathrm{V}^{-1}$ (detail of the calculation will be presented in section 3.5), which has not been possible from previous nonlinear measurements such as the second-harmonic generation (28; 29).

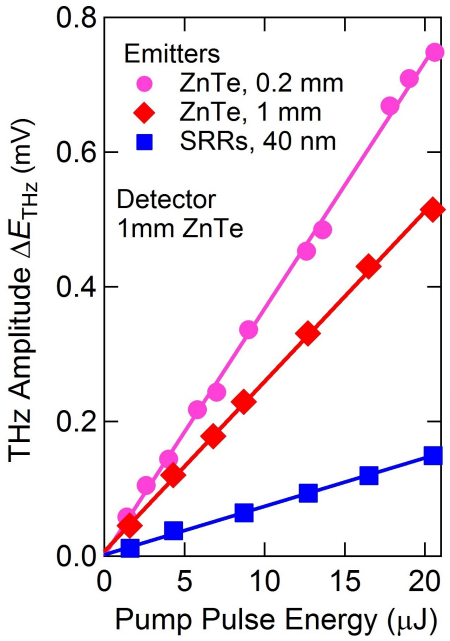

Figure 3.7 The peak-to-peak amplitude of THz signal versus pump energy measured with three different THz emitters: 0.2 mm ZnTe (magenta dots), 1 mm ZnTe (red diamonds) and SRR (blue squares) and the same detector of 1 mm ZnTe. The straight lines are from linear fitting.

3.4.5 Terahertz bandwidth from SRR emitter

Figure 3.8 plots normalized temporal traces of THz electric fields and corresponding spectral amplitudes from the SRR emitter. The THz detection crystals are 1 mm ZnTe (red), 0.2 mm ZnTe (blue) and 0.1 mm GaSe detector (green). This demonstrates the THz bandwidth of the SRR emitter up to 4 THz that is limited mostly by the excitation pulse duration of $\sim$ 140 fs (spectral width $\sim$ 13 meV or 3.2 THz) and by the Reststrahlen region of the inorganic nonlinear detector crystals (centered $\sim$ 5-6 THz). Our approach can potentially even generate much higher THz bandwidth by shortening the pump pulses because the SRR emitter does not suffer from the intrinsic limitation of the Reststrahlen region in almost all inorganic THz emitters/sensors.

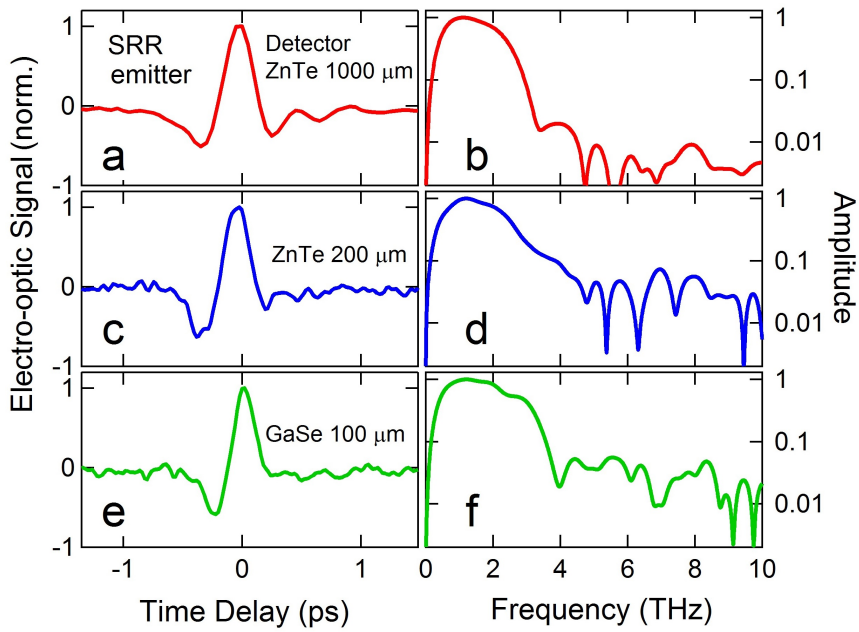

Figure 3.8 The normalized time-domain THz fields and corresponding spectral amplitudes generated from the same SRR emitter and measured by three different detectors: 1 mm ZnTe detector (red, a-b); 0.2 mm ZnTe (blue, c-d); and 0.1 mm GaSe (green, e-f).

3.5 Calculation of the Second-order Nonlinear Susceptibility of the SRR Emitter

We describe in this section the procedure to extract the second-order nonlinear susceptibility of the SRR emitter. We start with the wave equation in a nonlinear medium propagating in z-axis as (5):

$$\frac{\partial^2 E_{\mathrm{T}}(z,t)}{\partial z^2} - \frac{n_{\mathrm{T}}^2}{c^2}\frac{\partial^2 E_{\mathrm{T}}(z,t)}{\partial t^2} = \frac{1}{\varepsilon_0 c^2}\frac{\partial^2 P_{\mathrm{T}}^{(2)}(z,t)}{\partial t^2} = \frac{\chi^{(2)}}{c^2}\frac{\partial^2 |E_o(z,t)|^2}{\partial t^2} \tag{3.1}$$

where $E_{\mathrm{T}}(z,t)$ is the generated THz field, n_{T} the refractive index of THz pulses in the nonlinear medium, ε_0 the free space permittivity, c the speed of light, $P_{\mathrm{T}}^{(2)}(z,t)$ the second-order polarization of the nonlinear medium due to the optical pump beam $E_{\mathrm{o}}(z,t)$, and $\chi^{(2)}$ the second-order nonlinear susceptibility of the nonlinear medium. As shown in Fig. 3.9, we define a Gaussian optical pump pulse propagating in a nonlinear medium, and at $z = z'$ the optical pulse field amplitude can be expressed as $E_{\mathrm{o}}(z,t) = E_0 e^{-a(t-z'/v_{\mathrm{o}})^2}$, where a=2ln2/τ_{p}^2 and τ_{p} is the optical pulse duration, which is 140 fs in our case, and v_{o} is the group velocity

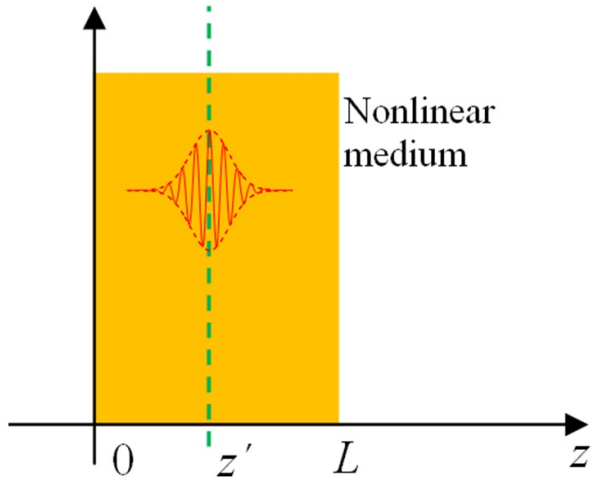

Figure 3.9 A Gaussian optical pulse at z=z′ propagates along z-axis in a nonlinear medium with thickness L.

of the optical pump pulse in the medium. THz radiation generated from an infinitesimal thin layer of the nonlinear medium at $z = z'$ can be expressed as $E_{\mathrm{T}}(z', t) = A\chi^{(2)}(1 - 4ax^2)e^{-2ax^2}$, where $x = t - \frac{z'}{v_{\mathrm{o}}} - \frac{L-z'}{v_{\mathrm{T}}}$, A is a constant, L the thickness of the medium, and v_{T} the phase velocity of THz pulses in the medium. Consequently, the THz field generated from a single sheet of SRRs can be obtained as

$$E_{\mathrm{T}}^{\mathrm{SRR}}(t) = A\chi_{\mathrm{SRR}}^{(2)}(1 - 4at^2)e^{-2at^2}. \tag{3.2}$$

In a thick nonlinear medium, the THz field generated can be obtained by taking the integration of the sheet result over the thickness. For a 0.2 mm thick ZnTe crystal, we have:

$$\begin{aligned} E_{\mathrm{T}}^{\mathrm{ZnTe}}(t) &= \int_0^{L=0.2\mathrm{mm}} E_{\mathrm{T}}(z', t)\mathrm{d}z' = \int_0^{L=0.2\mathrm{mm}} A\chi_{\mathrm{ZnTe}}^{(2)}(1 - 4ax^2)e^{-2ax^2}\mathrm{d}z' \\ &= \frac{Ac\chi_{\mathrm{ZnTe}}^{(2)}}{n_{\mathrm{T}} - n_o}\int_{t-2.10\mathrm{ps}}^{t-1.89\mathrm{ps}}(1 - 4ax^2)e^{-2ax^2}\mathrm{d}x. \end{aligned} \tag{3.3}$$

In the calculation, the group refractive index of optical pump beam at 1500 nm is $n_{\mathrm{o}} = n_{\mathrm{gr}}(1500\mathrm{nm})$=2.82 [ref (31)]. The central frequency of the THz spectrum $\sim$ 2 THz is used to determine the refractive index of THz in ZnTe, *i.e.*, $n_{\mathrm{T}} = n_{\mathrm{T}}(2\ \mathrm{THz})$. Because we found that our calculation is very sensitive to the indices which depend on each own crystal specifications, so in order to get as accurate calculation as possible, we measured it experimentally by comparing the time-domain THz transmission through free space and the 0.2 mm ZnTe crystal, from where

the refractive index is obtained. The results are shown in Fig. 3.10, which indicates that $n_{\mathrm{T}} = 3.15$ at 2 THz.

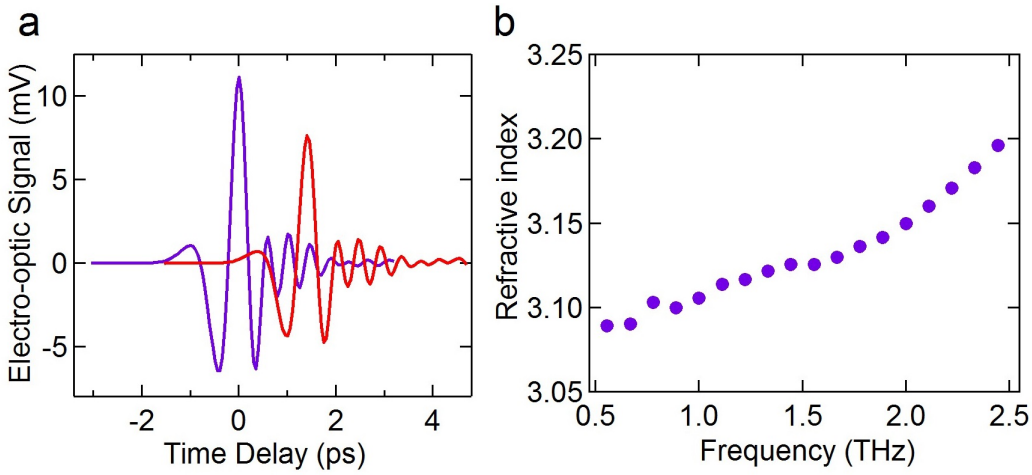

Figure 3.10 (a) THz time-domain signals transmitted through free space (purple) and the 0.2 mm ZnTe crystal (red). (b) The measured refractive index of the ZnTe crystal as a function of frequency

Knowing the measured peak-to-peak amplitudes $\Delta E_{\mathrm{T}}^{\mathrm{SRR}} \approx 0.2 \times \Delta E_{\mathrm{T}}^{\mathrm{ZnTe}}$ and $\chi_{\mathrm{ZnTe}}^{(2)} = 2r_{41} = 8 \times 10^{-12}$ m/V, where $r_{41} = 4 \times 10^{-12}$ m/V (32; 33) is the electro-optic coefficient of ZnTe, we can extract $\chi_{\mathrm{SRR}}^{(2)}$ from calculated THz electric fields by comparing Equs. 3.2 and 3.3. The result is shown in Fig. 3.11, where $\chi_{\mathrm{SRR}}^{(2)} = 0.8 \times 10^{-16}$ m^2/V reproduces the experimental peak-to-peak ratio. Therefore, we reveal a gigantic resonant sheet nonlinear susceptibility of SRRs, which is three orders of magnitude higher than the typical surface and sheet values. For example, the typical surface values are in the range of $\sim 10^{-22}$ m^2/V-10^{-21} m^2/V for fused silica and BK7 glass, $\sim 10^{-19}$ m^2/V for liquid crystals, inorganic and organic thin films (34; 35; 36).

Note the above calculations do not take into account the detector response function since THz waves from both SRRs and ZnTe are measured by the same detector.

3.6 Theory to the Terahertz Generation From Split-Ring-Resonators

The observed THz emission from the SRR emitter is due to optical rectification (OR) by the second-order nonlinear electric response arising from the electrons in the metal that makes

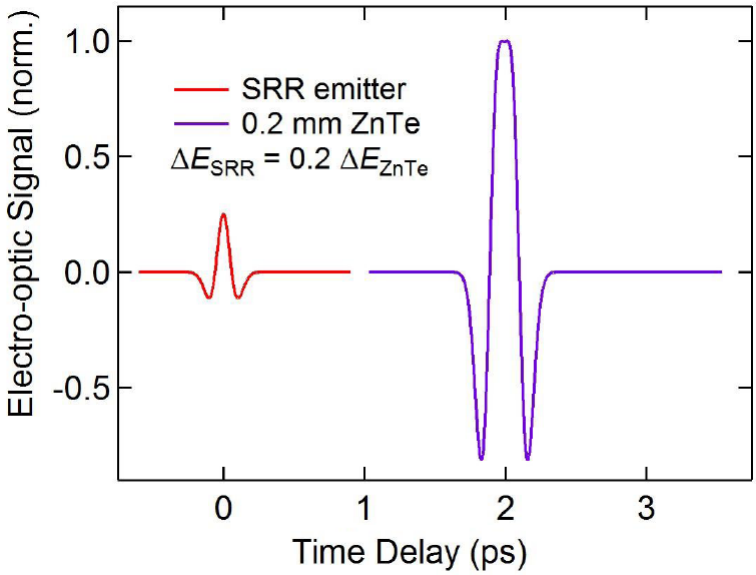

Figure 3.11 Theoretical calculation of the second-order nonlinear susceptibility of the SRR emitter. THz fields generated from the SRR emitter (red) and the 0.2 mm ZnTe emitter (purple) are plotted. The nonlinear second-order susceptibility of the SRR emitter is extracted by comparing the peak-to-peak amplitudes of SRR and ZnTe emitters.

up the SRR. As shown in previous literature, the electron gas in the metal can be described by a hydrodynamic model (28; 29; 30) known as Maxwell-Vlassov theory, which goes beyond the usual linear Drude model for the metallic response and contains second-order nonlinearities as described by:

$$\partial_t \mathbf{j} = \frac{ne^2}{m}\mathbf{E} - \gamma\mathbf{j} - \frac{e}{m}(\mathbf{E}\mathrm{div}\mathbf{E} + \mathbf{j}\times\mathbf{B}) + \frac{1}{ne}(\mathbf{j}\cdot\mathrm{grad})\mathbf{j} + \frac{e}{m}\mathrm{grad}p \tag{3.4}$$

$$p(n) = \frac{1}{5}(3\pi^2)^{2/3}\frac{\hbar}{m}n^{5/3} \tag{3.5}$$

The first two terms comprise the linear response as described by the conventional Drude model, the following terms are the nonlinear response of the electrons and represent Lorentz force, convective acceleration and Fermi pressure, respectively. All the nonlinear terms are second-order in the Maxwell fields, giving rise to a non-zero second-order electric polarizability $\chi^{(2)}$, which is responsible for the second harmonic generation as well as for the THz generation via OR considered here.

As was shown in Ref. (30), the main nonlinear contributions are coming from the $\mathbf{E}\mathrm{div}\mathbf{E}$ and $(\mathbf{j}\cdot\mathrm{grad})\mathbf{j}$ terms, which do not contribute in the bulk but do contribute on surfaces. Qualitatively, both terms behave like $j\rho$, current times accumulated density on the surface: As a consequence the nonlinear current is parallel or antiparallel to the linear current induced by the external excitation in regions of increasing or decreasing surface charge, respectively. This behavior is illustrated in Fig. 3.12: in the case of a simple straight nanorod (left panel), the radiation caused by the nonlinear current contribution (red arrows) in the two regions of surface charge accumulation (i.e. both ends of the nanorod) is out of phase, interferes destructively, and is not observed in the far field. Similarly, the symmetry of the current distribution at the electric dipole resonance of the SRR (middle panel) leads to nonlinear polarization that is parallel to the linear currents at the top ends of the SRR where (positive) charge is accumulating and anti-parallel at the bottom where (positive) charge is depleting. Hence, again, no radiation due to the nonlinear current contributions is observed in the far field. If, however, we excite the resonant mode that has a continuous current (without nodes) around the SRR ring (right panel), i.e. from the tip of one arm to the tip of the other, the nonlinear current in both arm are now parallel, their radiated fields interfere constructively and are observed in the far field. This mode is the magnetic resonance of the SRR, to which we couple electrically by the incident optical pulse (i.e. via the bi-anisotropic electric dipole moment across the gap), such that the resonance can be excited for normal incidence to the SRR plane. It should be noted that, although the mechanism also holds for second harmonic generation reported before (28; 29), the current phase-resolved THz results allow us to solve completely different pressing challenges in THz opto-electronics and gain new insights in nonlinear optics of metamaterials, i.e., quantitatively reveal the second-order susceptibility of the SRRs and phase reversal of THz emission, which have not been obtained in prior SHG experiment.

In first approximation we can describe the temporal optical input signal as a linearly chirped Gaussian pulse,

$$G(t) = e^{i(\Psi t^2+\Omega t+\phi)}h_{\sigma_0}(t) + e^{-i(\Psi t^2+\Omega t+\phi)}h^*_{\sigma_0}(t) \tag{3.6}$$

where $h_\sigma(t) = \frac{1}{2}e^{-\frac{1}{2}\sigma^2 t^2} \Leftrightarrow h_\sigma(\omega) = (2\sigma\sqrt{2\pi})^{-1}e^{-\frac{\omega^2}{2\sigma^2}}$, and $\Psi, \Omega, \phi, \sigma_0 \in \mathbb{R}$, and $\sigma_0 > 0$, and $\mathrm{Re}(\sigma^2) > 0$.

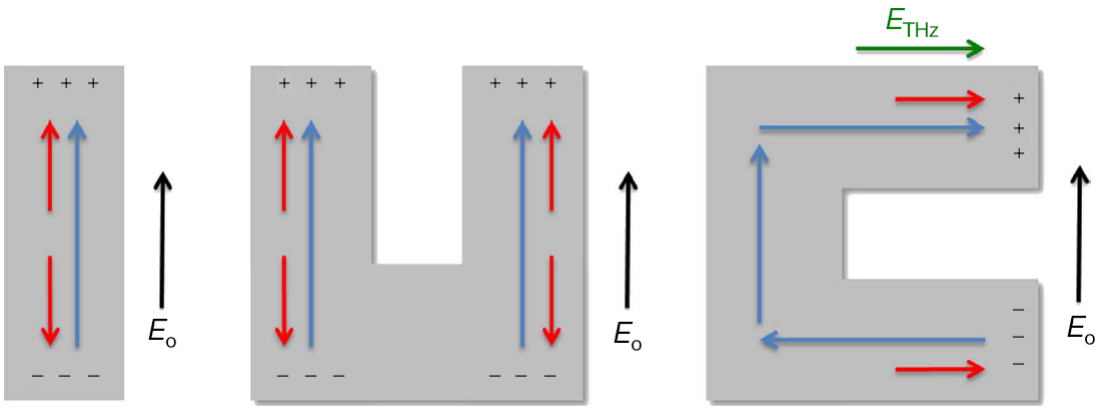

Figure 3.12 Distributions of the linear current (blue arrows) and nonlinear polarization (red arrows) for a linear cut-wire (left panel), the electric resonance (middle panel), and electrically excited magnetic resonance (right panel) of the SRR. The + and - indicate charge accumulation. Only the magnetic resonance of the SRR (right panel) exhibits an appreciable THz emission via difference frequency generation (DFG) due to the broken symmetry.

The linear chirp $\alpha = 2\Psi/\sigma_0^2$ is just a redefinition $\sigma = \sigma_0\sqrt{1 - i\alpha}$ and can be obtained from the difference in spectral width of the measured power spectrum of the pump pulse ($\sigma \approx 2\pi\times$ 9 THz) and the temporal width of the pump pulse derived from a cross-correlation measurement ($\sigma_0 \approx 2\pi\times$ 2 THz). Ω is the center frequency of the pump pulse and ϕ a phase shift between carrier and envelope.

$$G(t) = e^{i(\Omega t+\phi)}h_\sigma(t) + e^{-i(\Omega t+\phi)}h_\sigma^*(t) \Leftrightarrow G(\omega) = e^{i\phi}h_\sigma(\omega - \Omega) + e^{-i\phi}h_\sigma^*(-\omega - \Omega) \tag{3.7}$$

where $\sigma = \sigma_0\sqrt{1 - i\alpha}, \alpha = \frac{2\Psi}{\sigma_0^2}$, with the second-order nonlinear response being proportional to

$$G^{(2)}(t) = 2h_{\sigma_0}^2(t) + e^{i(2\Omega t+2\phi)}h_\sigma^2(t) + e^{-i(2\Omega t+2\phi)}[h_\sigma^2(t)]^* \Leftrightarrow \tag{3.8}$$

$$G^{(2)}(\omega) = \frac{1}{2}\left\{2h_{\sqrt{2}\sigma_0}(\omega) + e^{2i\phi}h_{\sqrt{2}\sigma}(\omega - 2\Omega) + e^{-2i\phi}h^*_{\sqrt{2}\sigma}(-\omega - 2\Omega)\right\}. \tag{3.9}$$

The OR is the first term in the spectrum above; the other two summands represent the SHG, which is removed from the signal by the Teflon filter in the THz signal path and by the detector crystals acting as an effective low-pass filter. Note that the chirp drops out and the OR signal only depends on the temporal envelope of the pump pulse.

We can write the radiated THz field in terms of a $\chi^{(2)}$ polarizability of the SRR sample shown as:

$$\mathbf{E}_{rad}^{(nl)}(\omega) \sim \chi^{(2)}(-i\omega)^2 G^{(2)}(\omega) \Leftrightarrow \mathbf{E}_{rad}^{(nl)}(t) \sim -\chi^{(2)}\partial_t^2 h_{\sqrt{2}\sigma_0}(t). \tag{3.10}$$

The time derivative in the radiated fields suppresses zero-frequency components such that the THz spectrum has a peak at finite frequency,

$$\mathbf{E}_{rad}^{(nl)}(\omega) \sim \chi^{(2)}\omega^2 e^{-\frac{\omega^2}{4\sigma_0^2}} \Leftrightarrow \mathbf{E}_{rad}^{(nl)}(t) \sim \chi^{(2)}\sigma_0^2(1-2\sigma_0^2 t^2)e^{-\sigma_0^2 t^2}. \tag{3.11}$$

The THz spectrum peaks at $\omega = 2\sigma_0$ and has a bandwidth $\Delta\omega_{\mathrm{FWHM}} \approx 2.31\sigma_0$.

Strictly, the radiated nonlinear fields are given by the currents in the SRR, which are proportional to the reflection amplitude of the electric sheet given by the SRR metasurface. So in the formulas above we have $G(\omega) \sim R(\omega)G^{(in)}(\omega)$. From the linear transmittance measurements of the SRR we get $R(\omega) \approx Z\sigma_e(\omega)/[2 + Z\sigma_e(\omega)]$ with $Z\sigma_e(\omega) \approx -i\alpha\omega/(\beta^2 - \omega^2 - i\gamma\omega)$ where $\alpha \approx$384, $\beta \approx 2\pi\times$199 THz, and $\gamma \approx 2\pi\times$15.4 THz. Thus, since the SRR resonance is very wide compared to the bandwidth of the optical pump pulse envelope ($\sigma_0 \approx 2\pi\times$2 THz) the effect of $R(\omega)$ on the THz pulse shape is negligible: In our experiments, the achievable THz bandwidth is limited by the duration of the optical pump pulse, not the SRR response.

A second, more severe problem is that the bandwidth and, in particular, the upper cut-off frequency (low-pass, between 2 and 3 THz depending on the used crystal) of the detectors is much smaller than the expected THz signal. As a consequence, the spectrum of the observed THz signal in our experiments is not limited by the OR but essentially given by the bandwidth of the detectors. The so predicted THz waveform agrees well with the experimental observation.

3.7 Summary and Outlook

In summary, we show that a single nm-scale layer of SRRs merges nonlinear metamaterials and THz science/technology, representing a new platform for exploring artificial-magnetism-induced nonlinear THz generation. This leads to broadband THz emission from deep-sub-wavelength-scale meta-atoms.

One of the future objectives is to design and fabricate 3D SRR emitters in order to greatly improve the THz emission intensity. Although our SRR emitter has much larger second-order

nonlinear efficiency than conventional nonlinear media, it is only nanometer thick, which cannot fully compete with the conventional nonlinear crystals of thousands times thicker at this stage regarding the total THz emission intensity. Our study opens fascinating opportunities for scaling up of the THz emission power via engineering 3D-like nonlinear metamaterials emitter and/or unit cells with even larger nonlinearities.

CHAPTER 4. TERAHERTZ WAVE MANIPULATION FROM PHOTO-IMPRINTED PHOTONIC STRUCTURES AND METAMATERIALS

In this chapter, we demonstrate ultrafast THz wave manipulations with 2 kinds of photonic structures: (i) the 1D and 2D photo-imprinted diffractive gratings and (ii) photoexcited double-SRRs metamaterials. For the first structure, the photo-imprinted diffractive elements are realized by projecting the optical image of a photomask onto a GaAs substrate using a fs laser source. The resulting high-contrast pattern of illuminated and dark regions creates diffractive elements to modulate THz waves with reconfigurable functionality. For the second structure, the fs laser excited double-SRRs modulate THz resonances and at relatively high fluence, photoexcited diffractive gratings emerge and dominate electric resonance, revealing a reversible and nonmonotonic modulation effect as a function of pump fluence.

Specifically, this chapter starts with the study of 1D and 2D photo-imprinted photonic structures. The experimental setup, photonic structure geometries and dimensions are presented in detail, as well as the THz modulation results as a function of the structure lattice constant, duty cycle, and pump fluence. Simulation is also performed in order to fully understand and explain the mechanism of the observed results. Next, this chapter moves on to the study of double-SRRs metamaterials. The sample information is given. The fluence-dependent and carrier-concentration-dependent resonance tunability are studied in detail. Simulation is finally performed to explain the experimental results.

This chapter is largely based on the published paper *Applied Physics Letters* **103**, 043101 (2013) and *Physical Review B* **86**, 125110 (2012).

4.1 1D and 2D Photo-imprinted Diffraction Gratings for Terahertz Wave Manipulation

4.1.1 Introduction

The THz spectral range has long been an inaccessible region in between the successful realms of electronics and photonics, because of the lack of efficient and compact sources and detectors for THz radiation. In the past few decades, however, the development of technologies like quantum-cascade lasers (1; 11; 12), THz wave generation through nonlinear crystals (37) and THz time-domain spectroscopy (38; 39) has enabled the exploration of THz science and the rapid rise of THz imaging and spectroscopy for, amongst others, biomedical and security applications (2; 13). However, controlling THz radiation has proven to be more difficult, although recent breakthroughs in waveguiding (40) and manipulating (41; 42; 43; 44; 45; 46) THz waves have been reported. A major driving force behind these breakthroughs is the progress that scientists have made in artificial materials containing conductive structures, for example, frequency-selective surfaces (47), metamaterials (9; 10; 48) and photonic crystals (49; 50; 51). By carefully tailoring the response of these artificial materials, it is possible to create THz devices like filters (41; 42),absorbers (43; 44),and polarizers (45; 46). It is even possible to achieve tunability by incorporating semiconductors with electrical biasing into the artificial materials (20; 21; 52) or the ability to switch between two different states (22; 53; 54; 55), but these devices have essentially a specific functionality determined at the time of their design.

In this section, we demonstrate a reconfigurable THz wave modulator, realized by creating a photonic structure by projecting the optical image of a metal mask onto a thin GaAs substrate using a femtosecond pulsed laser. We show that the resulting high-contrast pattern of photoexcited carriers can create diffractive elements, which can be tuned between a wide class of functionalities, such as beam shaping, beam steering, and wavefront correction, potentially providing a route to THz modulations with reconfigurable functionality.

4.1.2 Experimental setup and results

The scheme of the approach, which is based on diffraction gratings, is shown in Fig. 4.1. A 800 nm femtosecond pulsed laser beam illuminates a metal mask and the image of the mask is projected with a lens onto a 1 mm thick GaAs substrate. This creates a pattern of illuminated and dark regions on the substrate as shown in the inset of Fig. 4.1. Where illuminated, the pump beam creates carriers in the substrate by photoexcitation and the result is a photo-imprinted conductive pattern of free carriers inside the GaAs substrate, which we can use to manipulate THz waves. Being made from a copper film that is essentially impenetrable to the pump beam, the metal mask enables us in principle to create high-contrast light patterns on the GaAs substrate only limited by diffraction of the optical pump beam.

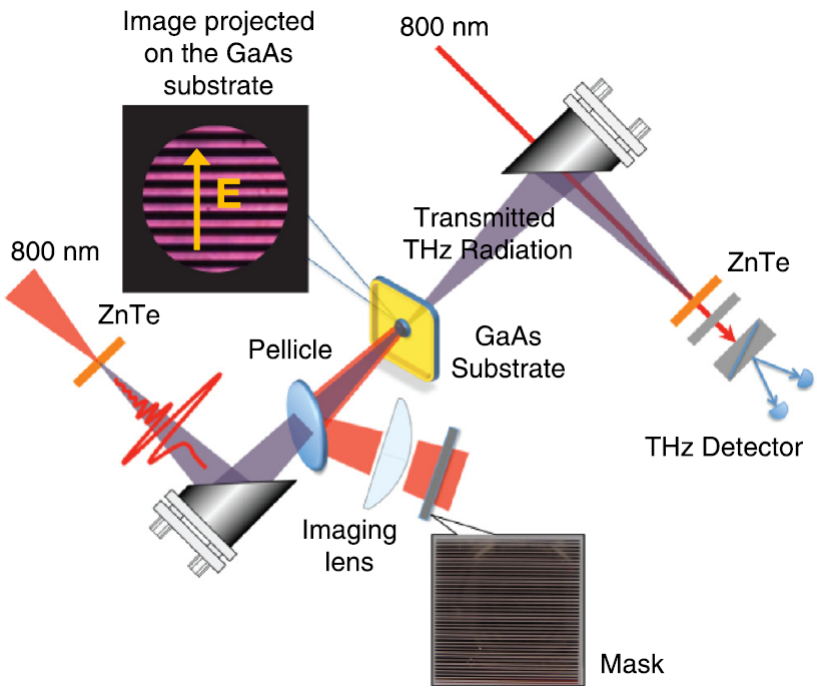

Figure 4.1 The experimental setup showing the key elements for reconfigurable diffractive gratings for THz wave manipulation. Optically projecting an image from a photomask onto a GaAs substrate creates a grating in carrier concentration in the surface of the GaAs.

We subsequently show experimentally that the resulting photo-imprinted patterns can be used as diffractive elements for THz waves operating in transmission, which is highly desirable

for many applications. THz pulses, generated by optical rectification of the femtosecond laser pulses in a 1 mm thick ZnTe crystal, are focused on the GaAs sample and the transmitted THz waves are detected by electro-optic sampling in a second 1 mm thick ZnTe crystal. The THz pulse duration is approximately 2 ps, which is much smaller than the life time of photoexcited carriers in GaAs (∼1 ns) and the diffusion length of the photocarriers (in 1 ns the carriers diffuse over a distance less than 2 μm) is much smaller than the diffractive element structure sizes, so the photo-imprinted grating can be considered essentially static for a single THz pulse. We start with a copper mask creating a photo-imprinted linear grating with lattice constant of 60 μm and a duty cycle of D=50% (i.e. 50% of the area is illuminated, 50% is dark). From the THz transmission spectra for a set of different pump fluences, shown in Fig. 4.2(a), we observe a pronounced spectral feature with strongly reduced transmission at about f=1.39 THz when the THz electric field is polarized perpendicular to the grating lines (TE). For the other polarization (TM), no sharp spectral feature is observed. We also observe higher background transmission levels for low pump fluence (i.e., few photocarriers are created) and low background transmission for higher pump fluence.

The two most plausible mechanisms possibly behind the spectral feature are either (i) coupling to the first diffraction order in GaAs or (ii) a quasi-static electric dipole resonance in the cut-wire elements created by the neighboring stripes of the grating. In order to distinguish between both mechanisms, we have fabricated a set of masks with varying lattice constant (duty cycle is fixed at D=50%) and a set with varying duty cycle (lattice constant is fixed at a=60 μm).

The transmission spectra for the set with varying lattice constant, displayed in Fig. 4.3(a), show a redshift of the spectra for increasing lattice constant. The spectral positions are inversely proportional to the lattice constants as shown in the inset of Fig. 4.3(a) and consistent with the cut-off frequency of the first diffraction order in GaAs, $f = c/n_{\mathrm{GaAs}}a$, with n_{GaAs}=3.56 for GaAs at 1 THz. The transmission spectra for the set with varying duty cycle, displayed in Fig. 4.3(b), show there is no shift in spectral position when the distance between the wires is changed. This observation rules out the electric dipole resonance, which has a resonance frequency that strongly depends on the capacitance between the cut wires (56). The redshift

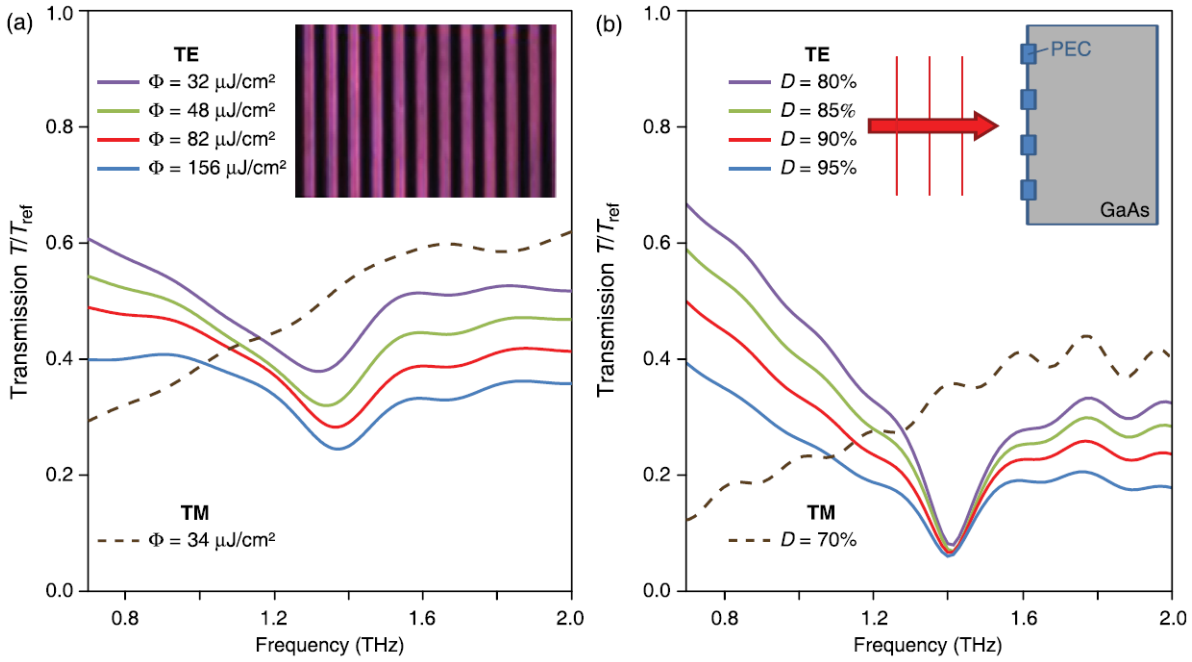

Figure 4.2 THz transmission spectra of the photo-imprinted linear grating. (a) Experimental transmission spectra of a grating with lattice constant a=60 μm and duty cycle D=50% for several pump fluences. The inset shows the projected image of the metal mask at the position of the sample measured with a CCD camera. (b) Simulation results from a simplified model of a diffraction grating with lattice constant a=60 μm) consisting of PEC wires for different duty cycles D.

of the spectral minimum when the grating period is increased points to application of our structure for reconfigurable THz filters.

Further evidence that our photo-imprinted gratings are purely diffraction-based and do not suffer from additional complications like quasi-static resonances or surface modes comes from simulation results involving a simple linear grating of perfectly conducting wires on a GaAs substrate [Fig. 4.2(b)]. The resulting transmission spectra agree qualitatively with the experimental spectra [Fig. 4.2(a)], both in the spectral position of the dip and the overall shape of the transmission spectra. No surface modes or quasi-static resonances are seen in the electric field distribution obtained from the simulations. In addition, comparison of the experimental results of Fig. 4.2(a) and the simple model in Fig. 4.2(b) tells us that different pump fluence values result in diffraction gratings with different diffraction efficiency; i.e., the pump fluence provides us with a straightforward control over the properties of the diffractive element.

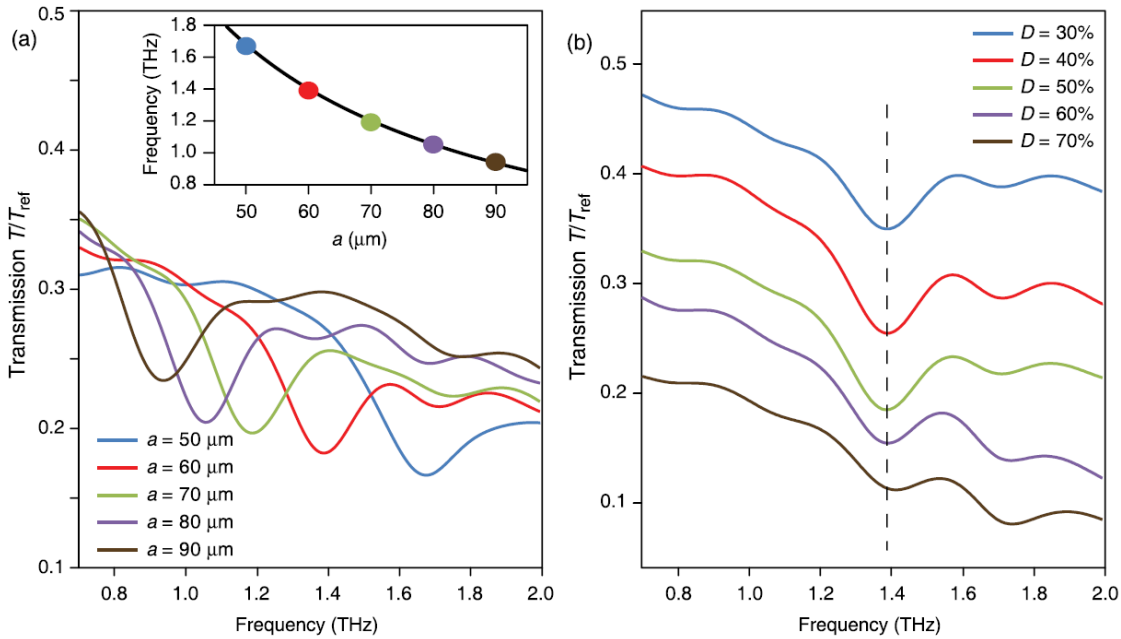

Figure 4.3 (a) Experimental transmission spectra for masks with varying lattice constant (Fluence is 96 μJ/cm^2; duty cycle is D=50%). The inset shows that the transmission dip frequencies are inversely proportional to the lattice constant (consistent with diffraction). The black line is the cut-off frequency of the first diffraction order in GaAs, $f = c/n_{\mathrm{GaAs}}a$. (b) Experimental transmission spectra for masks with varying duty cycle (96 μJ/cm^2; a=60 μm). The spectral position of the dips does not depend on the duty cycle (consistent with diffraction; inconsistent with a cut-wire resonance).

Not only can we create photo-imprinted linear gratings, but we can also generate two-dimensional diffractive elements on the GaAs substrate. One example is shown in the inset of Fig. 4.4 (a square lattice pattern with islands of photocarriers). The resulting transmission spectra plotted in Fig. 4.4 again show a clear minimum at the diffraction edge associated with coupling of energy into the first diffraction order. In fact we can create arbitrary patterns and these experiments therefore open the door to designing diffractive elements with well-established techniques from Fourier optics, which allow determining the required amplitude gratings for fairly general functions including beam shaping (Fresnel lenses, spatial filtering, wavefront correction) and beam steering, fan-outs, etc.

Finally, we performed realistic computer simulations of the experimental setup (the linear grating) that take into account the lossy nature of the photoexcited carriers. We now model

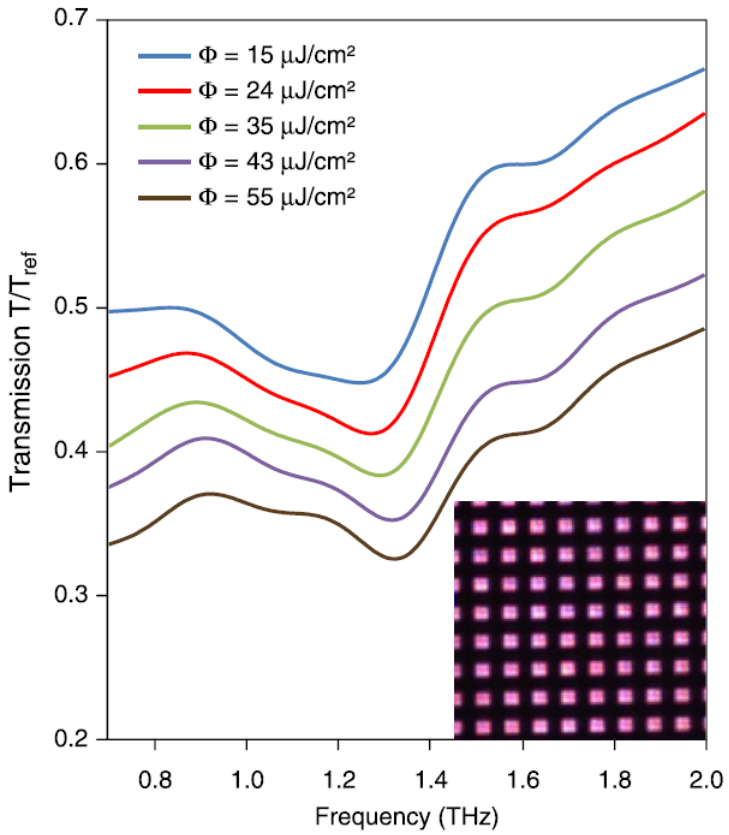

Figure 4.4 THz transmission spectra of a 2D photo-imprinted diffractive element. Inset: projected image of the metal mask at the position of the sample measured by a CCD camera.

the photoexcited free carriers as a conductive sheet with a frequency-dependent conductivity determined from measurements of illuminated GaAs substrates without any mask in place. Fig. 4.5 plots the transmission spectra from these realistic simulations for several values of the carrier density. They are in excellent agreement with the experiments shown in Fig. 4.2(a). We accounted for the finite contrast ratio in the image of the mask. For high fluences, this results in the creation of some photocarriers in the dark regions and, thus, in diffraction gratings with finite contrast. As a consequence, we get smaller dip amplitude than in the idealized simulation of Fig. 4.2(b). In addition, the background transmission now depends characteristically on the carrier density (pump fluence) and the transmission dip is slightly blue-shifted for higher carrier density, as observed in the experiment. The inset of Fig. 4.5 plots the electric field inside the GaAs substrate. We observe the typical checkerboard pattern created by the interference of

the transmitted and diffracted beams. We do not find any resonant fields in the structure, thus avoiding the dissipative loss that that would be produced by surface waves and resonant metamaterials (57). The simulations described in this paragraph will also be crucial in the design of the more intricate diffractive elements mentioned above.

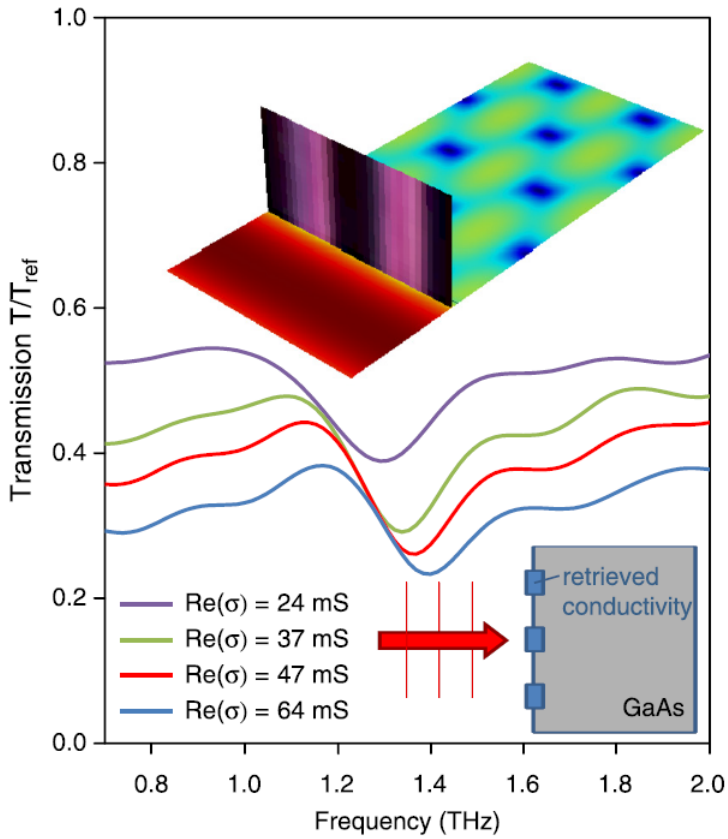

Figure 4.5 Transmission spectra from computer simulations of the photo-imprinted carrier grating taking into account the lossy nature of the photoexcited carriers. The conductivity values are specified at 1 THz. The inset plots the electric field component perpendicular to the grating at f=1.6 THz.

4.1.3 Summary and outlook

In summary, we demonstrated 1D and 2D photo-imprinted photonic structures to manipulate THz waves. The demonstrated photo-imprinted diffractive elements can be made reconfigurable by replacing the fixed metal mask employed here by a device with spatially controlled transmission for the optical pump beam. One possibility is a liquid-crystal spatial

light modulator as recently utilized by Okada and Tanaka (54) for tunable THz devices, but liquid crystals tend to have limited contrast, degrading the quality of the diffraction gratings as shown above. In order to retain the excellent contrast ratios provided by the basically impenetrable copper mask, we could replace the mask by a digital micromirror device (DMD) (58), a technology that is now widely used in digital-light-processing (DLP) projection equipment. The reconfiguration rate that can be achieved in this way will be limited by the DMD mirror switching time of about 20 μs. The previous grating must also be erased, of course, but with a typical recombination time of the photocarriers of 1 ns this will not be a limiting factor. This allows for a reconfiguration rate of 50 kHz, sufficient for both sensing and imaging applications relying on THz science.

4.2 Reversible Terahertz Wave Modulation in Strongly Photoexcited Metamaterials

In this section, we present the other kind of THz wave manipulation scheme, through the photoexcited double-SRRs metamaterials.

4.2.1 Introduction

Recently there has been significant interest in understanding ultrafast THz responses of nonlinear metamaterials, for example, metallic SRRs patterned on substrates exhibiting substantial nonlinearities (59). The resulting components and schemes allow for constructing controllable active THz devices with dynamical tunability of amplitude and phase, which fills the demanding THz technology gap. Prior experiments using time-domain THz spectroscopy have demonstrated dynamic tuning of both magnetic (20; 21; 22; 52; 60; 61) and electric (62) dipole resonances of SRRs on semiconductors or superconductors. More complex structures of coupled resonators on GaAs substrates have been proposed and experimentally studied, revealing frequency-agile THz modulation, for example, a resonance shift with increasing photoexcitation (22; 52). However, thus far all ultrafast studies of THz materials have been concentrated on the relatively low photoexcitation, where a reduction or quenching of the resonant absorptions is observed (20; 22; 63). Two outstanding issues are still poorly understood: First, there lack

insights on how high density photoexcited carriers modify the dynamic responses of metamaterials; second, the decay pathway of photoexcited metamaterials after femtosecond excitation is not explicitly studied, and, particularly, the temporal evolution of the transient states have only been understood as a density-independent relaxation back to the equilibrium.

In this section, we demonstrate an ultrafast reversible modulation of resonant THz absorption in strongly photoexcited metamaterials by optical pump and THz probe spectroscopy. This process directly manifests itself via a remarkable reemergence of the originally quenched THz resonance above a crossover density $N_c \sim 4.7 \times 10^{16}/\text{cm}^3$ after femtosecond photoexcitation. Increasing the excitation from below to above the transition density, we identify two distinctly different relaxation pathways of the THz resonance with opposite dynamics. A model calculation of transient spectra incorporating the first-order diffraction mode from the photoinduced transient grating reproduces the salient features, which is further corroborated by their dependence on the unit cell lattice constant. The revealed scheme represents a relatively simple and generic approach to achieve nonlinear and frequency-agile functions in THz devices without particularly complex structures.

4.2.2 Experimental setup and results

The samples used are double SRRs on GaAs, illustrated in Fig. 4.6, which are patterned 6 μm copper rings on high resistivity GaAs of 630 μm thick. We mainly focus on two SRR samples with unit cell lattice constant of 50 and 45 μm, and the outer dimension of an individual SRR is 36 μm. Our optical pump and THz probe spectroscopy setup is driven by a 1 kHz Ti:sapphire regenerative amplifier with 40 fs pulse duration at 800 nm. One part of the output is used to excite the sample, while the other part is used to generate and detect THz pulses. Phase-locked THz field transients are used as a probe, generated via optical rectification and detected by electro-optic sampling in 1 mm ZnTe crystals. Copper apertures of 2.5 mm are placed in front of the sample and a GaAs reference to ensure a uniform illumination and faithful comparison. The THz field transmission coefficient $T(\omega)$ is obtained by the ratio between two Fourier transformed spectra from the transmitted THz probe pulses through the SRRs and bare GaAs. We derive the complex transmission coefficient $T^*(\omega) = |T(\omega)|\, e^{i\phi(\omega)}$, where $|T(\omega)|$and

$\phi(\omega)$ are the amplitude and the phase, respectively, by the ratio for the Fourier transformed signals. Transient THz signals are recorded at various time delays with respect to the pump pulse to obtain time-dependent $T(\omega, \Delta\tau)$. The whole setup is purged with dry-N_2 gas.

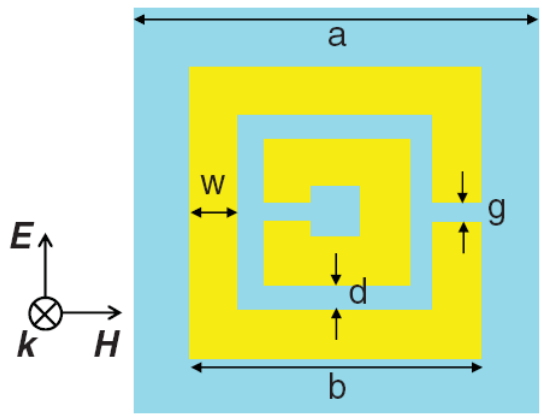

Figure 4.6 Schematic of the SRR unit cell of one of the samples with lattice constant 50 μm and the polarization of the normally incident THz radiation. a = 50 μm, b = 36 μm, d = 3 μm, g = 2 μm, and w = 6 μm.

The static transmission spectra are shown in Fig. 4.7(a) (black dotted line) with a THz probe normally incident on the sample plane. The E field of the THz probe is as shown in Fig. 4.6. There are two main THz resonances detected in this configuration at ω_1 ~1.6 and ω_2 ~ 0.5 THz, which originate from resonant electric processes consistent with prior measurements (20; 62). The ω_1 can be understood as the electric dipole resonance of the metallic bars of the SRRs, and the ω_2 is the magnetic dipole resonance induced by the circulating electric currents generated by the incident E field.

The two THz resonances exhibit distinctly different pump fluence dependence, as shown in the transient THz transmission spectra at $\Delta\tau$ =20 ps [Fig. 4.7(a)] for two pump fluences: 19 μJ/cm^2 (dashed cyan) and 56 μJ/cm^2 (solid red). The 20 ps pump probe delay is chosen to ensure a measure of quasi-steady state considering the transient carrier lifetime in GaAs on the order of 1 ns. The 19 μJ/cm^2 trace exhibits largely quenched resonances for both ω_1 and ω_2 after photoexcitation. However, the 56 μJ/cm^2 trace clearly shows substantial recovery of the resonant THz absorption around ω_1, while the ω_2 resonance remains quenched. This salient

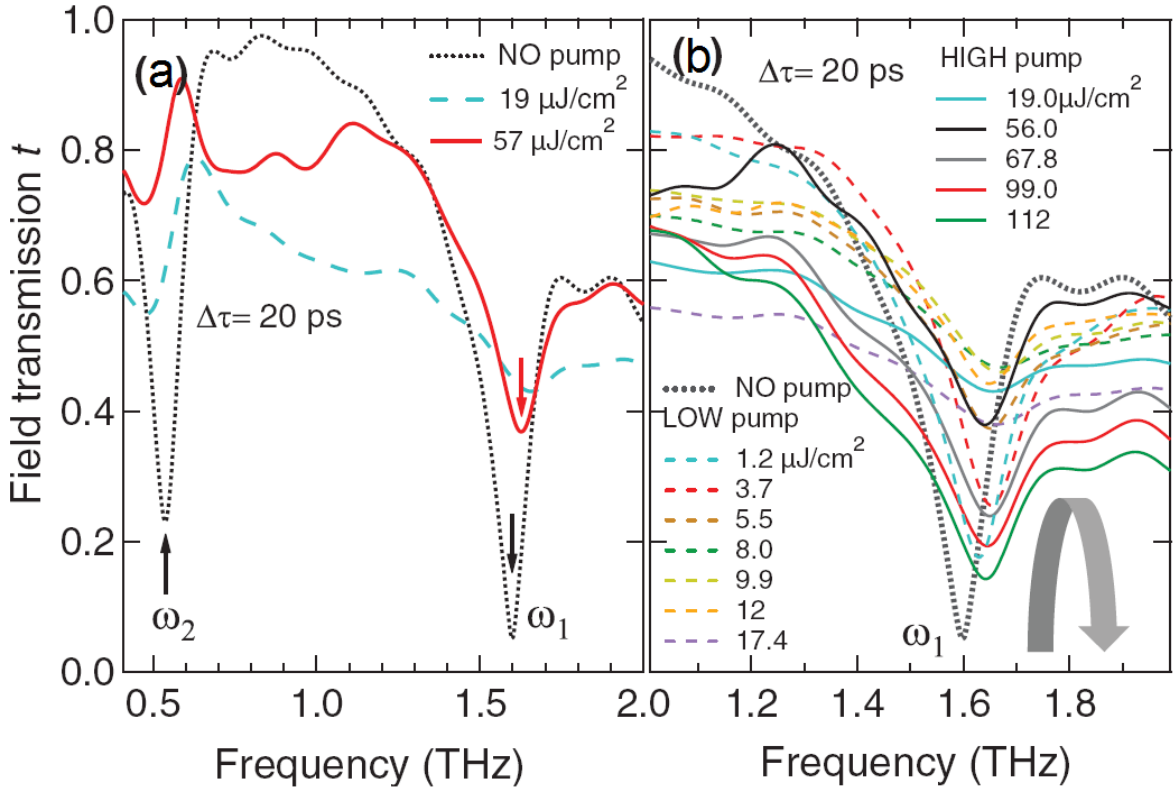

Figure 4.7 (a) Transient transmission spectra T(ω) taken under two excitation fluences, 19 (dashed cyan line) and 57 μJ/cm2 (solid red line), respectively. Static transmission spectra without pump is plotted together (black dotted line). (b) The nonmonotonic pump fluence dependence (indicated by the gray arrow) of the resonant absorption ~1.63 THz for low (dashed lines) and high (solid lines) photoexcitation. Spectra in both panels are taken at fixed pump probe delay of 20 ps.

feature is further corroborated in the detailed pump fluence dependence shown in Fig. 4.7(b). In the low excitation regime from 1.2 to 19 μJ/cm^2, there is a clear weakening in the transition strength and broadening in the linewidth for the ω_1 resonance, with an almost complete quenching at pump fluence of 19 μJ/cm^2. Here, the transmission is ~45% higher and the peak energy has a blue shift of ~60 GHz. In strong contrast, further increasing photoexcitation from 56 to 112 μJ/cm^2 results in a progressively pronounced resonance. The spectra clearly show a red shift of the resonance energy, ~20 GHz for the highest pump fluence used, a partial recovery of the transition strength and linewidth narrowing. This remarkable non-monotonic behavior and re-emerging resonance near the ω_1 manifest a reversible and frequency-agile modulation of

the resonant THz absorption by photoexcitation. This behavior has been seen experimentally observed for the first time. We explain below that for very high pump fluence, the first-order diffraction will surpass the electric resonance behavior in the THz responses of photoexcited metamaterials. In Fig. 4.7(b), the dips in the transmission above 56 μJ/cm^2 are due to the first-order diffraction peaks discussed below.

The weak and strong photoexcitations lead to significantly different relaxation pathways back to the equilibrium, as shown in the time evolution of $T(\omega)$ spectra following photoexcitation in Fig. 4.8. For pump fluence at 4 μJ/cm^2, the THz absorption at ω_1 resonance exhibits an initial photoinduced reduction, immediately followed by a relaxation back to the original value on a ns time scale. Interestingly, opposite to those at the low excitation, the 70 μJ/cm^2 dynamics clearly show a further reduction of the THz resonance $\sim$1.6 THz following the initial decrease. We emphasize two key aspects of this observation: (i) at the large time delay of $\Delta\tau$ =800 ps, the THz resonance $\sim$1.6 THz is almost completely quenched for the 70 μJ/cm^2 excitation, although a clear recovery of the resonance has been seen for the 4 μJ/cm^2 case; and (ii) the pump-fluence-dependent relaxation dynamics of the resonance indicates another way to achieve nonlinear and reversible THz modulation by tuning the time delay.

Ultrafast photoexcitation strongly alters the electronic states in the GaAs substrate by injecting non-equilibrium transient carriers by using ultrafast laser pulses with a pulse duration of 40 fs. Subsequent carrier-carrier/carrier-phonon collisions lead to decoherence and then to a quasi-thermal, hot transient carrier distribution within 1 ps. This hot carrier distribution further cools by emitting phonons and eventually relaxes to the equilibrium by carrier recombination on the order of 1 ns. In the weak excitation regime below 19 μJ/cm^2, the injected carriers make the GaAs substrate conductive. This leads to the reduction of the resonant absorption near ω_1 and even complete quenching of the resonances (20). Thus, the observed crossover from the photoinduced quenching to re-emergence of the THz resonance clearly indicates a new collective excitation setting at the high excitation regime not accessible in the previous measurements.

To gain quantitative insights into the transition density N_c for the excitation-induced crossover behavior, we experimentally study the evolution of the transient carrier density un-

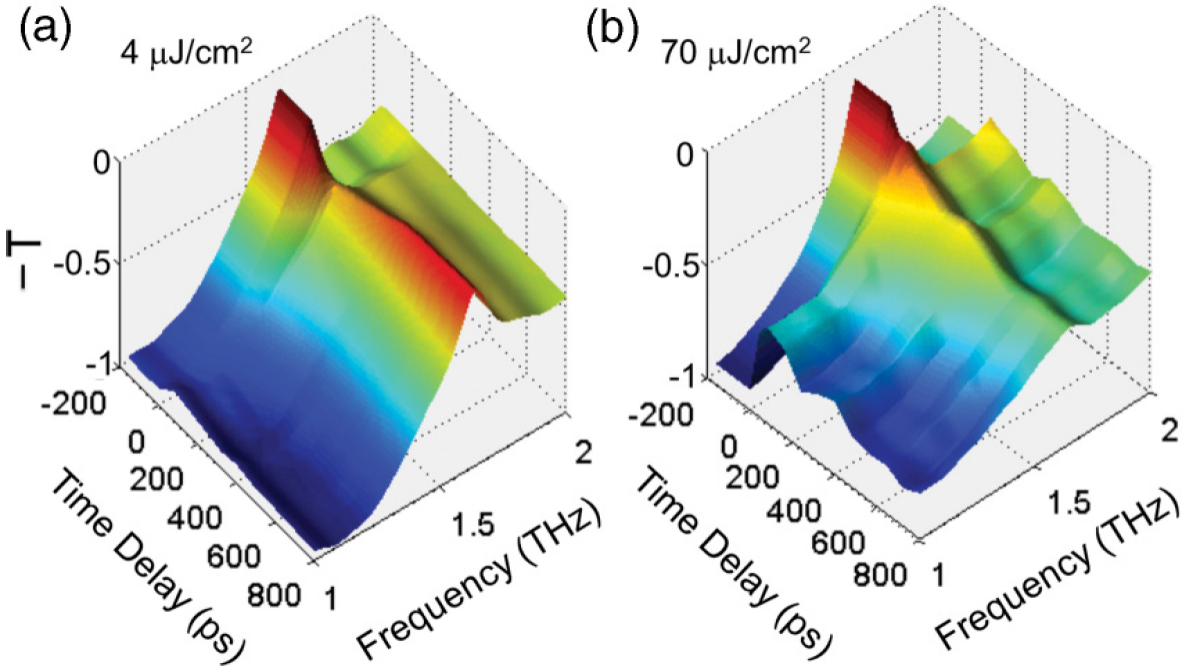

Figure 4.8 Time evolution of transmission spectra, plotted as -$T(\omega)$, in the photoexcited metamaterial of 50 μm lattice constant for (a) 4 μJ/cm^2 and (b) 70 μJ/cm^2, respectively. These clearly show the opposite relaxation pathways for the weak and strong excitation regimes.

der two different strategies: (i) tune the pump fluence with a constant time delay $\Delta\tau$, and (ii) play with the time delay $\Delta\tau$ by applying a fixed high pump power. The phase-sensitive nature of the time-domain THz field measurement can directly yield both real and imaginary parts of the optical conductivity in the photoexcited GaAs substrate on equal footing without any model assumptions. This provides a direct determination of the transient carrier density, based on an analysis using the Drude model (64). Referring to the set of measurements in Figs. 4.7 and 4.8, we show the fluence-dependent carrier concentration at $\Delta\tau = 20$ ps in the inset of Fig. 4.9, and the transition occurs at density $N_c = 4.7 \times 10^{16}/\text{cm}^3$, which corresponds to pump fluence 19 μJ/cm^2. On the other hand, Fig. 4.9 plots the temporal evolution of the transient carrier concentration excited by 70 μJ/cm^2, which shows an exponential decay with a peak density $\sim 10^{17}/\text{cm}^3$. By correlating the temporal profile to the fluence dependence of the carrier density, we define a crossover point at time delay of $\Delta\tau_c$ ~1.73 ns (black square)

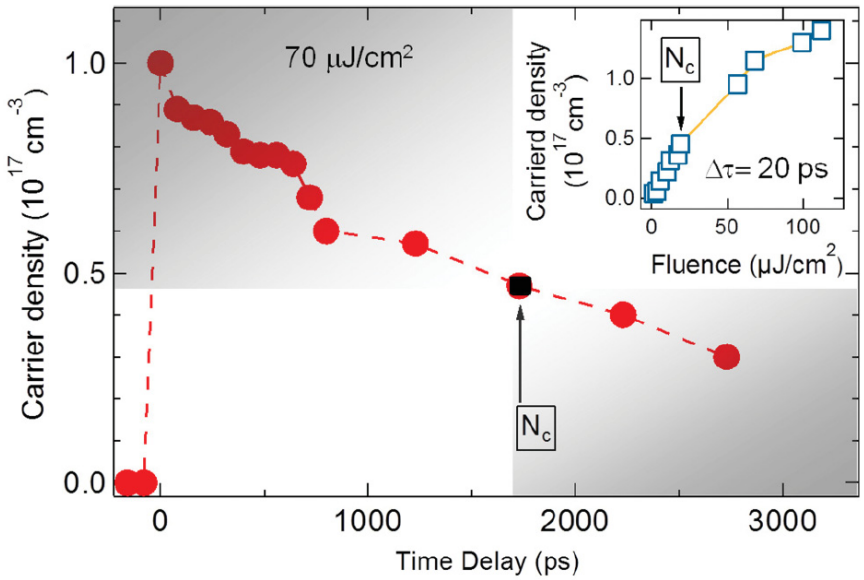

Figure 4.9 The extracted transient carrier concentration as a function of time delay. The left and right gray areas illustrate a crossover from the high to low excitation regime with a crossover density N_c (black square). The inset plots the extracted transient carrier concentration as a function of pump fluence at $\Delta\tau$ =20 ps, marked together with N_c corresponding to the density excited by 19 μJ/cm^2.

corresponding to the transition. This naturally divides the transient electronic density of photoexcited metamaterials into two regimes with opposite time and excitation dependence, as illustrated in the shaded areas of Fig. 4.9. Here, we mention the transition is not related to the high-reflective/antireflective regime discussed in Ref. (65). Transient spectra at various time delays, as shown in Fig. 4.10 show a reversal of the THz transmission change once the system is driven across the boundary, corroborating well with our conclusion, e.g., the THz transmission recovers its strength at $\Delta\tau$ =2.2 ns after initial quenching at time delays before 1.73 ns.

4.2.3 Simulations and discussions

Next, we analyze the transient THz response of photoexcited metamaterials by full-wave numerical simulations. First, we take into account photoinduced dynamic response of the GaAs substrate. In our simulations, for simplicity we only consider a 1-μm-thick homoge-

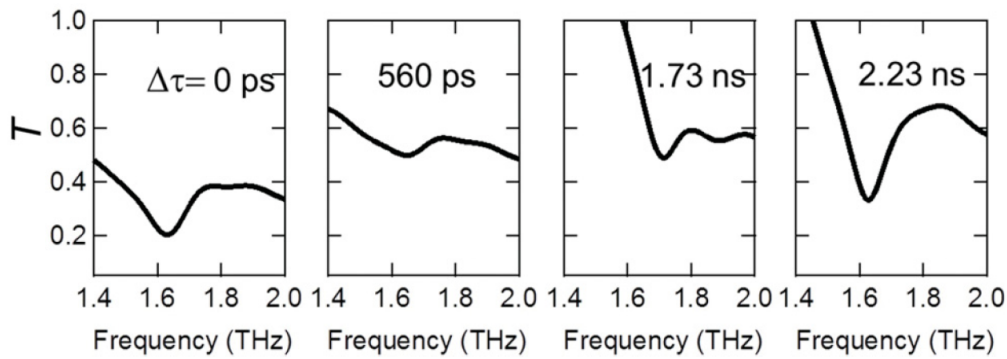

Figure 4.10 The transient transmission spectra $T(\omega)$ at various time delays following 70 μJ/cm^2 photoexcitation.

neously photo-modulated layer described by the well-established Drude model beneath the copper SRRs, but neglect the un-modulated regions hidden by SRRs in the optical path. (We have checked and determined it has little influence on the results.) The settings in the simulations describe the experiments, in which the two ports are settled in a vacuum at the two sides of the SRR sample, as the source and receiver ports, shown in Fig. 4.11. A time filter has been used to gate out the echo signals from the multi-reflection, the same as the time windowing in the experiments. The frequency-dependent complex conductivity of the Drude model for the photoexcited layer is $\sigma = \varepsilon_0\omega_\mathrm{p}^2/(\gamma - i\omega)$. Here, ε_0 is the permittivity of a vacuum, γ represents the collision frequency, and $\omega_\mathrm{p} = \sqrt{Ne^2/(\varepsilon_0 m^*)}$ the plasma frequency. The free electron charge e is 1.6×10^{-19} C and the effective carrier mass in GaAs, $m^* = 0.067m_0$. We modulate the carrier density N in our simulations. Thus, the photoexcited layers has the dielectric function, $\varepsilon(\omega) = \varepsilon_s + i\sigma/(\varepsilon_0\omega)$, where ε_s (=12.7) is the dielectric constant of the undoped GaAs substrate. In our simulations, we keep $\gamma = 1.8$ THz for all the cases as in Ref. (62).

Figure 4.12(a) shows the simulated transmission spectra for various carrier densities N. The simulation clearly shows the crossover from a reduction to an enhancement of the resonant THz absorption ~1.6 THz as the excitation from low to high density regimes. This agrees well with the photoinduced reversible modulation demonstrated in the experiments. Specifically, in the low density below 4.0×10^{16}/cm^3, the THz resonance peak in the transmission curve exhibits clearly weakened transition strength, a blue-shift and spectral broadening. Increasing

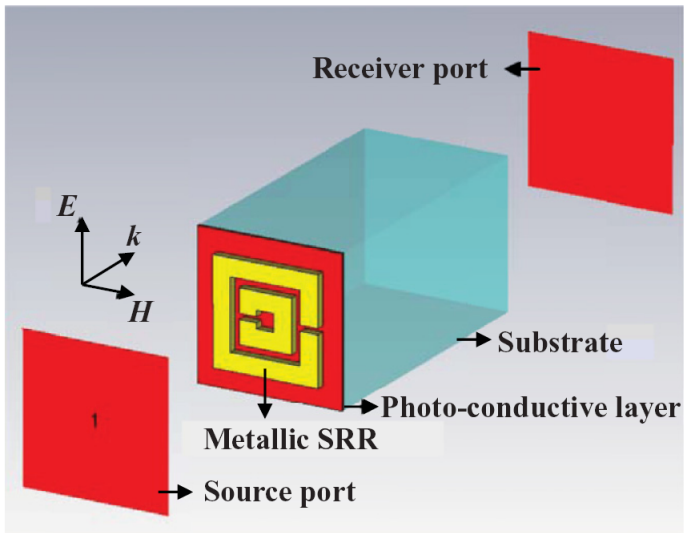

Figure 4.11 Schematic of the simulation configuration.

the carrier density above $4.0 \times 10^{16}/\text{cm}^3$, the resonant THz peak progressively reemerges, e.g., a clear transmission dip seen for the case $N = 8.1 \times 10^{17}/\text{cm}^3$. From the simulations, we can attribute the reemergence of the resonant THz absorption at high density to the effect of first-order diffractive waves from photoinduced transient grating. Due to the periodic structure of the SRRs, the first-order diffractive wave is determined to propagate in the substrate at high excitation, which strongly influences the fundamental absorption mode. This leads to a new THz transmission dip at $f_1 = c/(na)$ above a transition density $\sim 4.0 \times 10^{16}/\text{cm}^3$. Here, c is light speed in a vacuum, n the refractive index of GaAs, and a the lattice constant of the structure. The SRR structure with the dipole resonance close to f_1 allows achieving a reversal of resonant THz absorption with increasing photoexcitation, due to a crossover in the absorption from the dipole mode to the diffraction mode.

In the photoexcited states, the resonance ~1.6 THz will be influenced by both electrical dipole resonance and the first-order diffraction, due to photoinduced grating. Both show strong excitation fluence dependence, whose interplay leads to the observed reappearance of the THz resonance. Regarding the contribution from the first-order diffraction, it indeed exists regardless of the excitation fluence. However, the efficiency of the diffraction should strongly depend on the excitation fluence because the index contrast is a strong and nonlinear function of the

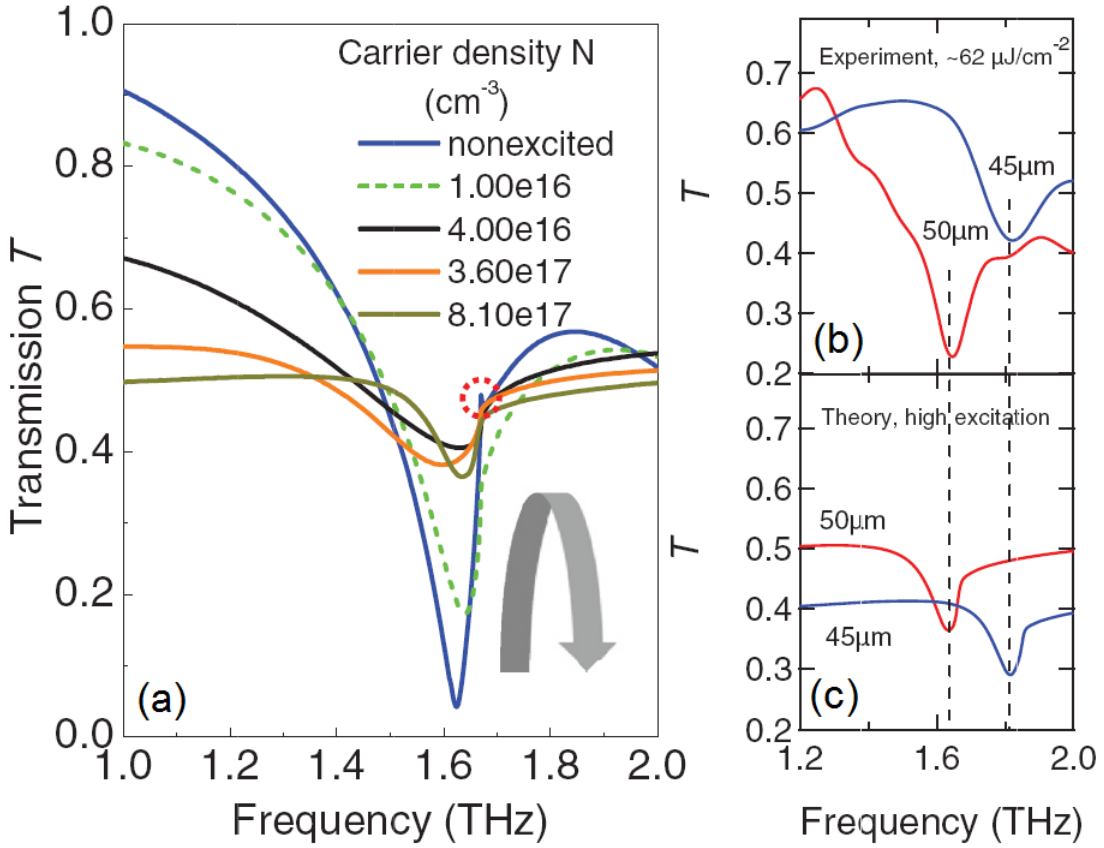

Figure 4.12 (a): The simulated THz transmission spectra for various carrier densities N. The photoinduced THz resonances in the strong excitation regime for two different lattice constants 45 and 50 μm: (b) experiment and (c) simulation.

photo-injected carrier density. In the low fluence regime, the first-order diffraction is relative inefficient and produces smaller scattering intensity than from the photoinduced softening of electrical dipole resonance. Consequently, the net effect is the decrease of the amplitude of the THz resonance. However, the opposite behavior appears at high photoexcitation. Here, the electrical dipole resonance is strongly quenched and the response is dominated by first-order diffraction contributions. The diffraction peak becomes more pronounced at high pump fluence. Thus, referring to the cross-over point in Fig. 4.9, we can attribute this to a transition between two regimes, where the first (low fluence) is dominated by electrical dipole absorption in metamaterials, and the second (high fluence) by first-order diffraction. Additionally, if we have a careful look at the simulation results for the unpumped case in Fig. 4.12(a), we may

find a feature of a tiny kink at the frequency corresponding to the first-order diffraction. Such a feature finally becomes a dip under high fluence.

To corroborate our model, we compare the re-emerged THz resonances from the experiment [Fig. 4.12(b)] to those from the simulation [Fig. 4.12(c)] for two different lattice constants, 50 and 45 μm, respectively. The simulations are performed on the structures with the same double-SRR array for the case with the density $N = 8.1 \times 10^{17}/\text{cm}^3$. It is clearly visible that the simulated transmission dip to higher frequency by decreasing the lattice constant and the dip positions tightly link to the frequency of the first-order diffraction mode for each case. An extremely good agreement between the simulation and the experiment is found for the transmission-dip position and its shift, which underpins the effect of the high-order diffraction mode in the strongly excited metamaterials.

4.2.4 Summary and outlook

In summary, we have demonstrated ultrafast photoinduced reversible modulation of resonant THz absorption in strongly photoexcited metamaterials. Increasing the excitation from below to above the threshold density N_c we observe a crossover from a complete quenching to a reemergence of the THz resonance. Our analysis and theoretical simulations, based on the first-order propagation from the photoinduced transient grating, explain the density- and lattice-constant-dependent frequency shifts. Our results clearly identify the importance of photoinduced optical modes in metamaterials, besides the electronic resonances, which should be carefully considered in designing future multifunctioning photonic-electronic devices using the artificial periodical structures. The easy implementation of the revealed scheme represents another approach to achieve nonlinear and frequency-agile functions in THz devices.

CHAPTER 5. ULTRAFAST TERAHERTZ PROBES OF INTERACTING DARK EXCITONS IN CHIRALITY-SPECIFIC SEMICONDUCTING SINGLE-WALLED CARBON NANOTUBES

In this chapter, we demonstrate ultrafast THz electrodynamics of lowest-lying dark excitons in optically excited (6,5) semiconducting carbon nanotubes. THz photons directly probe the intra-excitonic transition $1s(g)\rightarrow 1s(u)$ between the lowest-lying dark and bright exciton states with an energy gap $\sim$6 meV under different lab conditions, e.g., lattice temperature, excitation wavelength, and fluence. The experimentally observed THz responses are reproduced by an analytical model which enables quantitative analysis of transient densities of dark excitons and free e-h plasma, oscillator strength, transition energy renormalization and relaxation dynamics. Non-equilibrium, yet stable, quasi-1D quantum states with dark excitonic correlations rapidly emerge even with increasing off-resonance photoexcitation and experience a unique crossover from dominantly dark exciton states to complex phase-space filling of both dark and bright pair states, different from dense 2D/3D excitons influenced by the thermalization, cooling and ionization to free carriers.

Specifically, this chapter starts with an introduction to the physical and electronic structures of carbon nanotubes. The dark exciton energy dispersion of semiconducting carbon nanotubes is also described. Next, the sample preparation procedures and basic characterizations are provided. The experimental setup and how we understand and analyze THz results are discussed in detail. This chapter ends with a summary and outlook.

This chapter is largely based on the published paper *Physical Review Letters* **114**, 107402 (2015).

5.1 Motivations

Quasi-one-dimensional (quasi-1D) excitons in single-walled carbon nanotubes (SWNTs), with large binding energies of hundreds of meV, naturally arise from strong quantum confinement and reduced screening of electron-hole (e-h) pairs (66; 67). Their internal structure is characterized, in a 1D hydrogen-atom-like description, by a center-of-mass momentum K and by internal quantum numbers (designated here as 1s, 2s, 2p...). These strong excitonic behaviors manifest themselves in extensive static or ultrafast optical interband absorption or emission spectra in individually separated SWNTs, which are stable even in the presence of unbound e-h carriers from residual tube aggregation and/or metallic tubes (68; 69; 70; 71). However, unlike the hydrogen atom, the correlated e-h pairs in SWNTs evolve in a "modified vacuum" with exotic, chiral symmetry arising from the underlying graphene lattice that gives twofold degeneracy at K and K' points. Coulomb interaction splits such "doubling" into odd (u) and even (g) symmetry states entailing a series of bright and optically forbidden, dark exciton pairs, including the lowest $1s(g)$ and $1s(u)$ (72; 73). Thus far, the dark ground state $1s(g)$, hidden from both single- and two-photon optical interband transitions, is still largely unexplored.

While magneto-optics and light scattering measurements established the existence of dark excitons in SWNTs (74; 75; 76), the search for possible dipole-allowed, lowest transitions $1s(g)\rightarrow 1s(u)$ remains open. Particularly, as these linear probes do not depend critically on quasi-particle/exciton interaction and the associated fast dynamics, they provide little insight into interacting states that are characterized by the co-existence of both the dark & bright excitons and their complex interplay with e-h plasma. Exactly these aspects govern the radiative lifetime and photoluminescence (PL) efficiency, key for SWNT-based optoelectronic applications (77; 78). The lack of quantitative probes and scarce ultrafast measurements for dark states seriously limit their thorough understandings and perspectives of exploring related novel quantum phenomena, e.g., the excitonic Bose condensate (79) and other exotic ground states.

Selective optical pump and THz probe technique represents a versatile spectroscopy tool that is extremely relevant for *quantitative* study of dark excitons. THz pulses directly couple the $1s(g)\rightarrow 1s(u)$ transitions, which represents a direct consequence and measure of excitonic

pair correlations and resulting *dark* states in SWNTs. Being independent of momentum K, THz pulses measure genuine dark exciton population across entire K space, while the available interband optical probes (PL, absorption), due to symmetry and momentum conservation, only detect a subset of excitons near K=0. Additionally, the capability of resonant and off-resonant excitations by tuning the pump photon energy enables, among others, the study of excitons in single chirality tube and of exciton-plasma interaction. These critical aspects for dark exciton studies are absent in prior experiments of SWNTs.

5.2 Introduction to Dark Excitons in Semiconducting Carbon Nanotubes

5.2.1 The physical structure of carbon nanotubes

Carbon nanotubes are hollow cylinders rolled-up from graphene sheets. There are different types of nanotubes depending on the roll-up vector, called chiral vector, along which direction the graphene sheets are rolled-up. The magnitude of the chiral vector also characterizes the nanotube circumference. As shown in Fig. 5.1, the carbon atom lattice basis vectors are defined as $\mathbf{a}_1$ and $\mathbf{a}_2$. The indexed chirality (n,m) defines the roll-up chiral vector $n\mathbf{a}_1$+$m\mathbf{a}_2$ and also determines the electronic properties of nanotubes, e.g., their band gaps.

The zigzag axis is along $\mathbf{a}_1$ vector and the armchair axis is in between $\mathbf{a}_1$ and $\mathbf{a}_2$ vectors, i.e., along $\mathbf{a}_1 + \mathbf{a}_2$ direction, as shown in cyan lines in the Figure. If m=0, the chiral vector is along zigzag axis $\mathbf{a}_1$, therefore such nanotubes are called zigzag nanotubes. For example, the (5,0) nanotubes in light purple color in the Figure. If n=m, the chiral vector is along the armchair axis, therefore such nanotubes are called armchair nanotubes. For example, the (3,3) nanotubes in light green color. If the chiral vector is neither along the zigzag nor the armchair axes, the nanotubes are called chiral nanotubes. For example, the (4,3) nanotubes in magenta color. The angle between the zigzag axis and chiral vector is defined as the chiral angle α.

5.2.2 The electronic structure of carbon nanotubes

The electronic band structure of carbon nanotubes can be obtained from that of a 2D graphene sheet, which is formed by sp^2 hybridization of atomic orbitals in carbon atoms. In

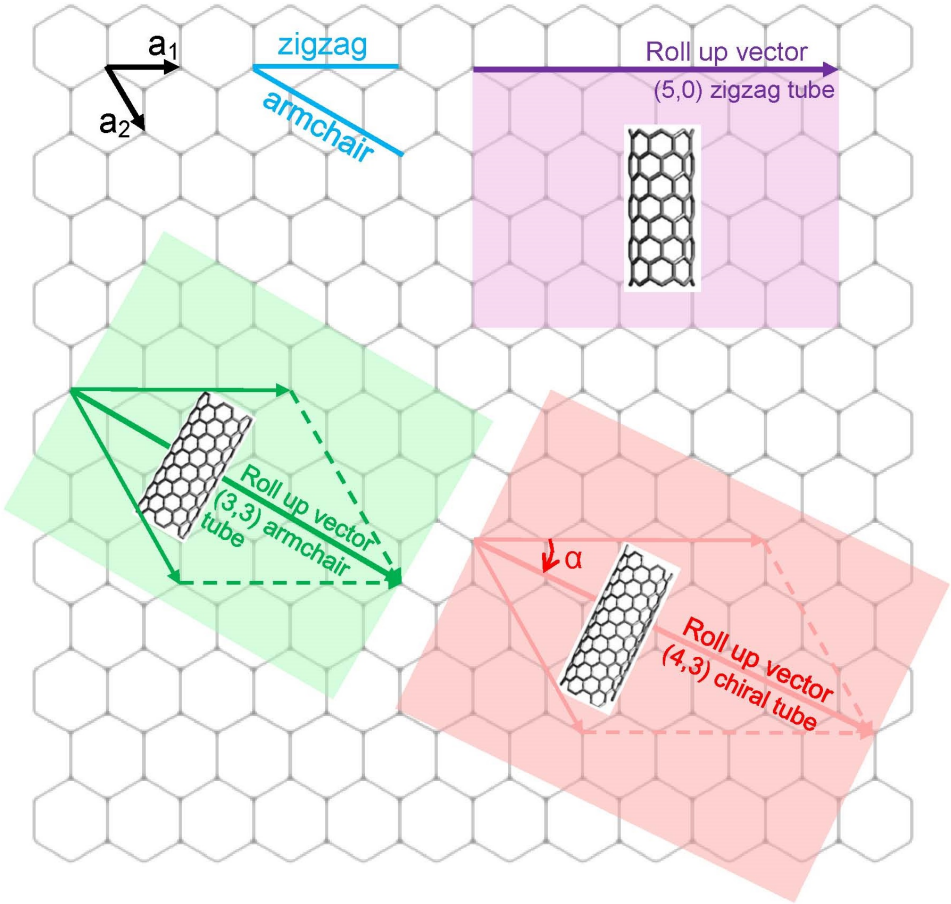

Figure 5.1 Physical structures of carbon nanotubes. A nanotube is obtained by rolling-up the graphene sheet along the chiral vector and matching the two ends of the chiral vector $n\mathbf{a}_1+m\mathbf{a}_2$ together to form a cylinder. Therefore, the magnitude of the chiral vector also defines the circumference of the nanotube. Thus obtained nanotube is said to have chirality (n,m). Note the nanotubes shown in the 3 shaded areas are only schematic and not drawn to scale.

graphene, one $2s$ and two $2p$ orbitals (e.g. $2p_x$ and $2p_y$) of a carbon atom are hybridized and form covalent bond, called σ-bond, with corresponding orbitals of another adjacent carbon atom (see Ref (80) for details). Another $2p$ orbital (e.g. $2p_z$) of the carbon atom forms another type of relatively weaker bond, called π-bond, with the other carbon atom. Therefore, there are three σ-bonds and one π-bond in sp^2 hybridization. The electrons from π-bond having weaker binding energy are valence electrons. They are responsible for carrier transport and other electronic and solid state properties. The tight binding model is used for the calculation of the electronic band structures of π-bond electrons in graphene.

As shown in Fig. 5.2, graphene has periodic honeycomb lattice structure with carbon atom separation a_0=1.42 Å. The unit cells of graphene have translational symmetry in the direction of the unit vectors $\mathbf{a}_1$ and $\mathbf{a}_2$. The wave function of the lattice Ψ thus has to satisfy the Bloch's theorem (80)

$$T\Psi = e^{i\mathbf{k}\cdot\mathbf{a}_i}\Psi \quad (\mathrm{i} = 1, 2), \tag{5.1}$$

where T is a translational operator along the direction of the unit vectors $\mathbf{a}_\mathrm{i}$ (i=1, 2), and $\mathbf{k}$ is the wave vector.

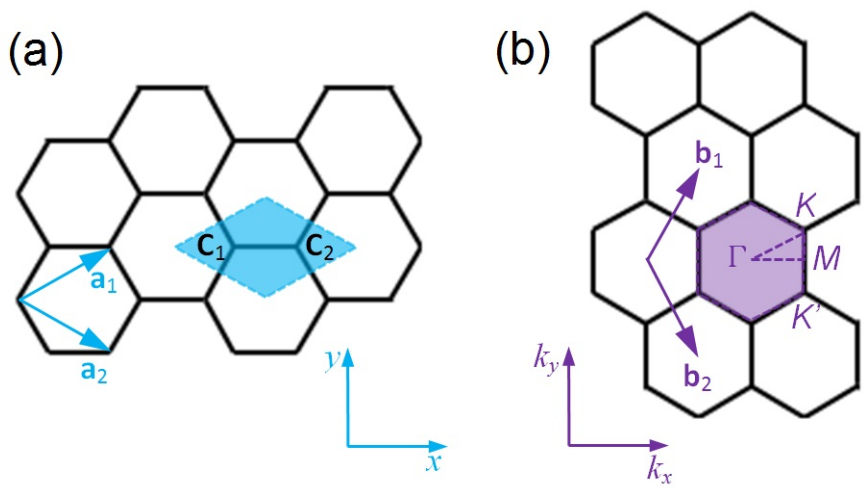

Figure 5.2 (a) Definition of the graphene lattice unit vectors $\mathbf{a}_1$ and $\mathbf{a}_2$ and unit cell shown in the shaded area in real space. There are 2 carbon atoms C_1 and C_2 in each unit cell. (b) Definition of the reciprocal lattice vectors $\mathbf{b}_1$ and $\mathbf{b}_2$ and unit cell in k space. The first Brillouin zone is shown as the shaded area. Γ is the center of the hexagon, K and K' the corners, and M the center of the edge.

One possible solution which satisfies Equ. 5.1 is based on the j-th atomic orbital in the unit cell. The tight binding Bloch function is written as (80)

$$\Phi_j(\mathbf{k}, \mathbf{r}) = \frac{1}{\sqrt{N}} \sum_{\mathbf{R}}^{N} e^{i\mathbf{k}\cdot\mathbf{R}} \varphi_j(\mathbf{r} - \mathbf{R}) \quad (j = 1, 2, ..., n), \tag{5.2}$$

where $\mathbf{R}$ is the position of the atom, N the number of unit cells, φ_j the atomic wavefunction in the state j, n the number of Bloch wavefunctions. For each $\mathbf{k}$, there are n Bloch functions.

Using boundary condition for $M = N^{1/2}$ unit vectors in each $\mathbf{a}_\mathrm{i}$ axis for a 2D graphene

$$\Phi_j(\mathbf{k}, \mathbf{r} + M\mathbf{a}_\mathrm{i}) = \Phi_j(\mathbf{k}, \mathbf{r}) \quad (\mathrm{i} = 1, 2), \tag{5.3}$$

we obtain the wave number $k = 2q\pi/Ma_{\mathrm{i}}$, where q is an integer ranging from 0 to M-1. And the eigenfunctions $\Psi_j(\mathbf{k},\mathbf{r})$ can be written as a linear combination of Bloch functions

$$\Psi_j(\mathbf{k},\mathbf{r}) = \sum_{j'=1}^{n} C_{jj'}(\mathbf{k})\Phi_{j'}(\mathbf{k},\mathbf{r}), \tag{5.4}$$

where $C_{jj'}(\mathbf{k})$ are constants to be calculated by minimizing the j-th eigenvalue $E_j(\mathbf{k})$, i.e., $\partial E_j(\mathbf{k})/\partial C_{jj'}$=0, which can be written as

$$E_j(\mathbf{k}) = \frac{\langle\Psi_j|\mathcal{H}|\Psi_j\rangle}{\langle\Psi_j|\Psi_j\rangle} = \frac{\sum\limits_{j',j''=1}^{n} \mathcal{H}_{j'j''}(\mathbf{k})C^*_{jj'}C_{jj''}}{\sum\limits_{j',j''=1}^{n} \mathcal{S}_{j'j''}(\mathbf{k})C^*_{jj'}C_{jj''}}, \tag{5.5}$$

where

$$\mathcal{H}_{j'j''}(\mathbf{k}) = \langle\Phi_{j'}|\mathcal{H}|\Phi_{j''}\rangle \quad \mathcal{S}_{j'j''}(\mathbf{k}) = \langle\Phi_{j'}|\Phi_{j''}\rangle \tag{5.6}$$

They are called transfer integral matrices and overlap integral matrices respectively.

Rewriting Equ. 5.5 can yield $[\mathcal{H} - E_j(\mathbf{k})\mathcal{S}]C_j = 0$. The physically meaningful solution (the other solution C_j=0 is not physically meaningful) to this equation is given by

$$\det[\mathcal{H} - E_j(\mathbf{k})\mathcal{S}] = 0. \tag{5.7}$$

Equation 5.7 is called the secular equation. Solving the secular equation yields the eigenvalues for $E_j(\mathbf{k})$. There are n eigenvalues for a given $\mathbf{k}$ because j=1, 2, ..., n.

For 2D graphene, as shown in Fig. 5.2, the unit vectors are written as

$$\mathbf{a}_1 = (\frac{\sqrt{3}}{2}a, \frac{a}{2}), \quad \mathbf{a}_2 = (\frac{\sqrt{3}}{2}a, -\frac{a}{2}), \tag{5.8}$$

where $a = \sqrt{3}a_0 = \sqrt{3} \times 1.42\text{Å} = 2.46\text{Å}$, and a_0 is the carbon-carbon bond length. The corresponding reciprocal lattice vectors are

$$\mathbf{b}_1 = (\frac{2\pi}{\sqrt{3}a}, \frac{2\pi}{a}), \quad \mathbf{b}_2 = (\frac{2\pi}{\sqrt{3}a}, -\frac{2\pi}{a}) \tag{5.9}$$

as shown in Fig. 5.2(b). There are two Bloch functions constructed from the two inequivalent carbon atoms at C_1 and C_2 sites in the unit cell. In this case, the (2×2) transfer integral and overlap integral matrices $\mathcal{H}$ and $\mathcal{S}$ are obtained by substituting Equ. 5.2 into Equ. 5.6, which yields the

$$\mathcal{H} = \begin{pmatrix} \epsilon_{2p} & tf(k) \\ tf^*(k) & \epsilon_{2p} \end{pmatrix}, \quad \mathcal{S} = \begin{pmatrix} 1 & sf(k) \\ sf^*(k) & 1 \end{pmatrix} \tag{5.10}$$

where ϵ_{2p} is the orbital energy of $2p$ level, t is the transfer integral which is negative in the case, and $f(k) = e^{ik_x a/\sqrt{3}} + 2e^{-ik_x a/2\sqrt{3}}\cos(k_y a/2)$ [Ref (80)]. Substituting Equ. 5.10 in to Equ. 5.7, we obtain the eigenvalue given by

$$E_j(k_x, k_y) = \frac{\epsilon_{2p} \pm t\sqrt{1 + 4\cos(\frac{\sqrt{3}k_x a}{2})\cos(\frac{k_y a}{2}) + 4\cos^2(\frac{k_y a}{2})}}{1 \pm s\sqrt{1 + 4\cos(\frac{\sqrt{3}k_x a}{2})\cos(\frac{k_y a}{2}) + 4\cos^2(\frac{k_y a}{2})}} \tag{5.11}$$

The energy dispersion relation $E(\mathbf{k})$ is thus obtained and plotted in Fig. 5.3. The magnified energy structure near one of the corners of the first Brillouin zone K is shown on the right. The circular cone-shaped bands are called Dirac cones. The 2 Dirac cones meet at the Dirac point. Therefore, graphene is a zero-gap semiconductor and sometimes considered semimetal.

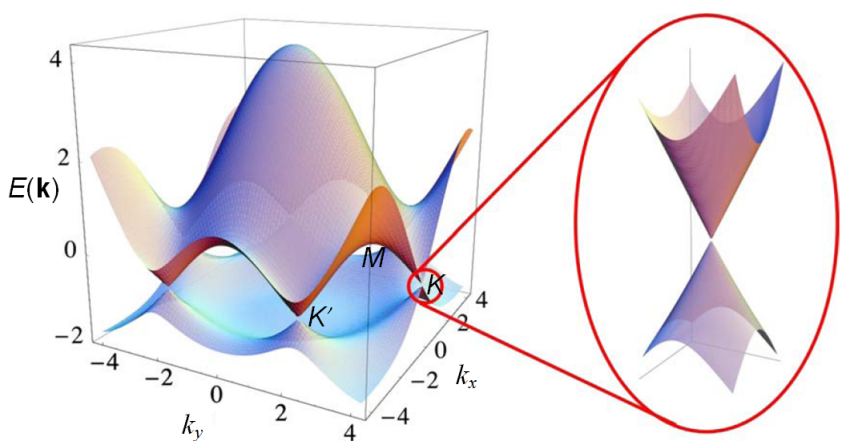

Figure 5.3 The electronic band structue of 2D graphene sheet in the fist Brillouin zone. The figure is taken from Ref (81).

For a 2D graphene sheet with size much larger than wavelength, the wave vector k is considered to be continuous. However, when a carbon nanotube is rolled-up from a graphene sheet, the wave vector associated with the direction of the chiral vector is quantized due to the confined length along this direction, but the wave vector associated with the direction of the tube axis is unaffected. Therefore, the nanotube energy bands consist of a set of 1D energy bands which are cross sections of those for 2D graphene as shown in Fig. 5.4. If the allowed wave vector k (Fig. 5.4, solid lines, left panel) goes through one of the Dirac points, the energy band has zero bandgap. Such nanotubes are metallic tubes (the top panel). On the other hand, if the allowed wave vector k does not go through any of the Dirac points, the energy band has

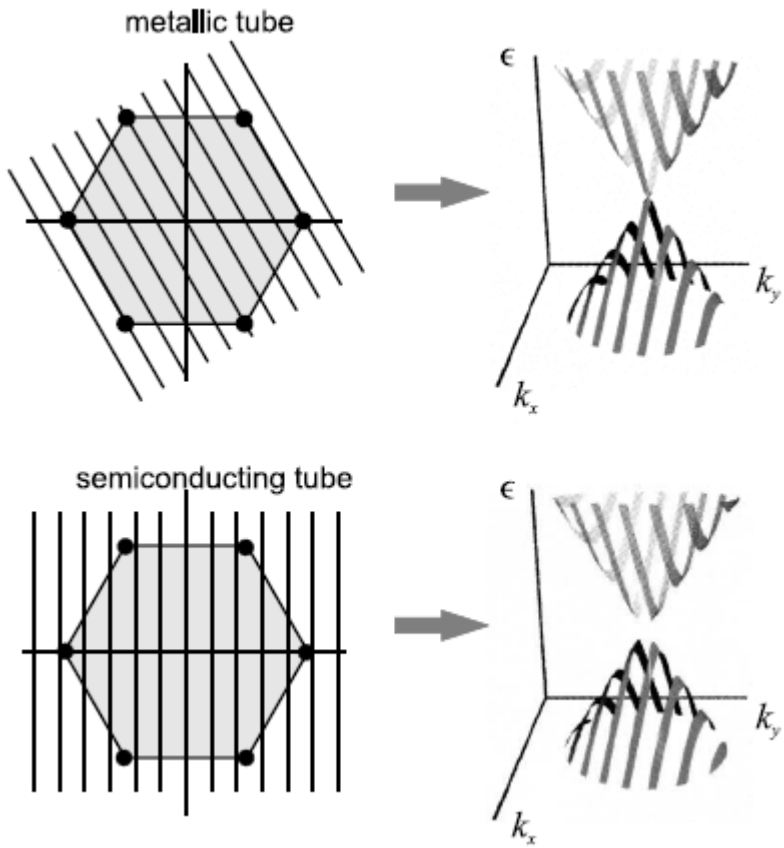

Figure 5.4 The carbon nanotube energy bands derived from a 2D graphene sheet. If the allowed wave vector k (solid lines, left panel) goes through one of the Dirac points, the energy band has zero bandgap. Such nanotubes are metallic tubes (the top panel). On the other hand, if the allowed wave vector k does not go through any of the Dirac points, the energy band has finite bandgap. Such nanotubes are semiconducting tubes (the bottom panel). The allowed k values are determined by the chiral vector. The figure is taken from Ref (82).

finite bandgap. Such nanotubes are semiconducting tubes (the bottom panel). The allowed k values are determined by the chiral vector. If $2n+m$, or equivalently n-m, is a multiple of 3, the nanotubes are metallic; otherwise, they are semiconducting. For example, all the armchair nanotubes are metallic, since $n=m$, so that $2n+m=3n=3m$, which is always a multiple of 3. The zigzag nanotubes (n,0) are only metallic when n is a multiple of 3.

5.2.3 Exciton electronic states in semiconducting carbon nanotubes

In the first Brillouin zone of semiconducting carbon nanotubes, there are 2 equivalent valleys near K and K' as shown in Fig. 5.5(a). When we build one exciton, we take one electron from the conduction band and one hole from the valence band. There are 4 possibilities to do so. For example, the 2 cross-valley transitions as indicated by the 2 dashed line arrows are not allowed, because they require momentum change, but photon has very small momentum, so these 2 transitions cannot couple to a photon. We call these 2 exciton states dark excitons. The corresponding exciton electronic states are shown in Fig. 5.5(b) as indicated by the 2 lowest dashed levels on the sides with pair momentum K much larger than 0. For the 2 direct transitions as indicated by the 2 solid line arrows, the Coulomb mixing leads to an even parity (g) state and an odd parity state (u). By selection rules, $1s(g)$ state is still dark, but the other one $1s(u)$ (solid line) is bright, which means the $1s(u)$ state is allowed to couple to a photon. So there are 4 exciton states, 1 of which is bright, 3 are dark. If we take spin into account, the 2 particle mixing of electron and hole pairs leads to the spin singlet-triplet splitting. By selection rules, the 1 spin singlet state is bright and the 3 spin triplet states are dark. If we combine them together, we find most excitons (15 out of 16) are dark. This largely limits the fluorescence-based and optoelectronic-device applications of semiconducting carbon nanotubes.

5.3 The Optical Pump and Terahertz Probe Experiment

5.3.1 Sample preparation and characterization

We study Co-Mo-catalyst grown SWNTs of mainly (6,5) and (7,5) chiralities embedded in a freestanding 50 μm sodium dodecylbenzenesulfonate (SDBS) film through drying a D_2O solution of SDBS-dispersed SWNTs (83). The SDBS ensures both wide transparency of the polymer matrix in THz range and also serves as a surfactant to effectively reduce SWNT bundles. The absorption spectrum in Fig. 5.6 exhibits the distinct E_{11} and E_{22} quantized interband absorption peaks of dominant (6,5) and (7,5) chiralities, overlapping E_{11} ~1.24 eV for both chiralities and well-separated E_{22} ~2.17 eV (572 nm) for (6,5) and ~1.90 eV (652 nm) for (7,5) tubes, respectively (84).

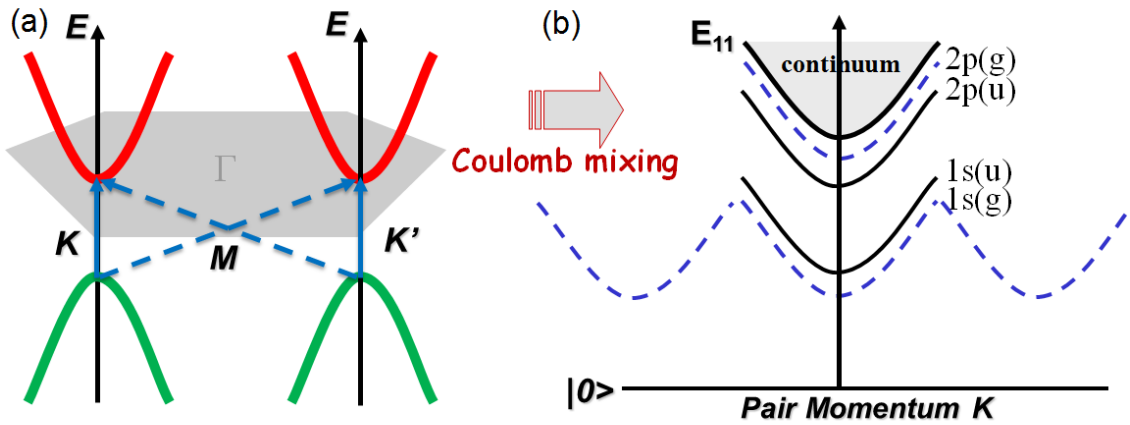

Figure 5.5 (a) The lowest electronic levels of semiconducting carbon nanotubes in the first Brillouin zone. (b) The simplified excitonic energy levels of (a) due to Coulomb mixing of electron and hole pairs. Only a few representative states are shown. The dark exciton states are indicated by dashed lines. The bright exciton states are indicated by solid lines.

Each chirality is associated with substantially prolonged relaxation times and significantly enhanced photobleaching, as shown in the differential transmission spectra (Fig. 5.7) $\Delta T/T$ after 1.55 eV photoexcitation as a function of probe photon energy and time delay. These observations are consistent with the extensive interband studies of high-quality chirality-enriched SWNT samples at visible and near-infrared spectral regions, which are explained by the joint effects of resonantly-enhanced radiative lifetime and exciton-exciton annihilation (EEA) (68; 69).

5.3.2 Experimental setup

The optical pump THz probe spectroscopy setup is driven by a 1 kHz Ti:sapphire regenerative amplifier with 40 fs pulse duration and 800 nm (1.55 eV) center wavelength. The schematic of the setup is shown in Fig. 5.8. One part of the output is used to either off-resonantly excite the sample or pump the OPA, which resonantly excites the E_{22} transition of the (6,5) tubes at 2.17 eV. The other part is used to generate and detect phase-locked THz field transients, used as a probe for $1s(g) \rightarrow 1s(u)$ transition (see Fig. 5.9), via optical rectification and electro-optic sampling in 1 mm thick $\langle 110 \rangle$ ZnTe crystals. 2 delay stages are used in the pump and genera-

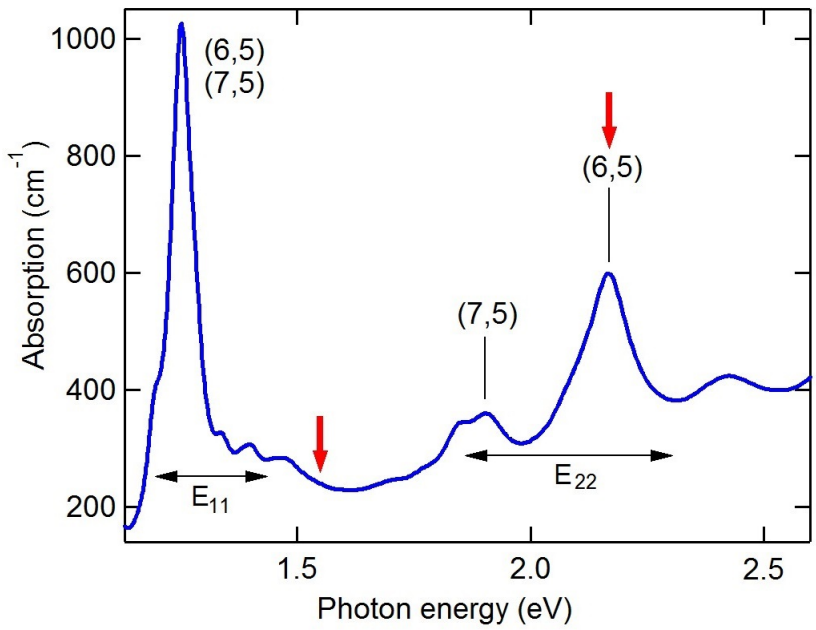

Figure 5.6 The absorption of the 50 μm thick SWNTs/SDBS film showing clearly the dominant (6,5)(7,5) nanotube E_{11} and E_{22} bands. The red arrows indicate 2 photon energies used to excite the sample, either resonant excitation of (6,5) E_{22} transition at 2.17 eV or off-resonant excitation at 1.55 eV which is away from any exciton resonance peak.

tion beams to control the temporal delays of pump-THz and THz-sampling beams respectively. The sample is mounted into a vacuum cryostat to cool it down to 5 K. A copper aperture of 2.5 mm diameter is placed in front of the sample to ensure a uniform pump illumination. Another copper aperture with the same size is used as a reference to measure the THz free propagation. 2 Teflon filters are used to transmit THz pulses and block optical beam residues. The THz section of the setup is purged with dry N_2 gas in order to remove the absorption of THz radiation by water vapor.

5.3.3 Experimental results and data analysis

To probe the response of the excitonic ground states shown in Fig. 5.9, the THz fields in time-domain are measured. Through the fast Fourier transformation and Fresnel equation, the spectral transmissions consisting of the spectral amplitudes and phase information are extracted respectively, from which the frequency dependent complex-valued dielectric function

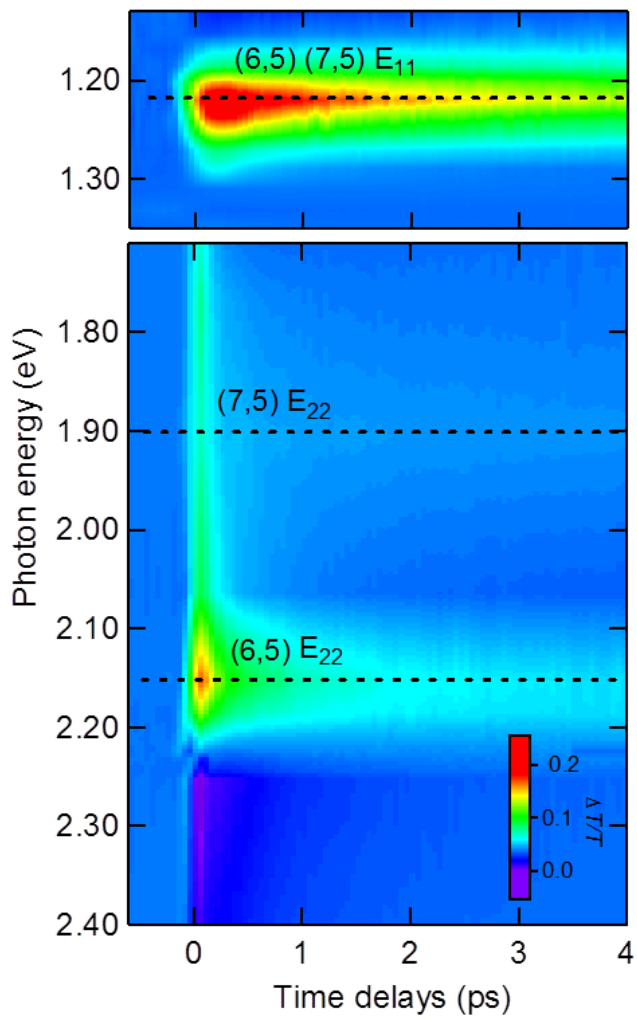

Figure 5.7 The temporally- and spectrally-resolved differential transmission $\Delta T/T$ after 1.55 eV photoexcitation of the SWNTs sample at T=300 K showing clearly the excitation of mainly (6,5) and (7,5) chiralities.

for unexcited sample $\widetilde{\varepsilon}(\omega)$ and its pump induced transient change after pump-probe delay $\Delta\tau$ is obtained as $\Delta\widetilde{\varepsilon}(\omega, \Delta\tau) = \widetilde{\varepsilon}_{\text{excited}}(\omega, \Delta\tau)$ - $\widetilde{\varepsilon}(\omega)$ (85; 86). The corresponding conductivity can be calculated by $\widetilde{\sigma}(\omega) = i[1 - \widetilde{\varepsilon}(\omega)]\omega\varepsilon_0$. The simultaneously obtained ultrafast conductivity and dielectric function *quantitatively* measure the dynamic evolution of both the excitons and *e*-*h* plasma.

Effective medium approximation is applied in order to obtain the nanotube dielectric function $\widetilde{\varepsilon}^{\text{NT}}(\omega)$ from the experimentally measured effective dielectric function $\widetilde{\varepsilon}(\omega)$. The space filling ratio, defined as FR, of the sample is calculated by measuring the intensity transmittance

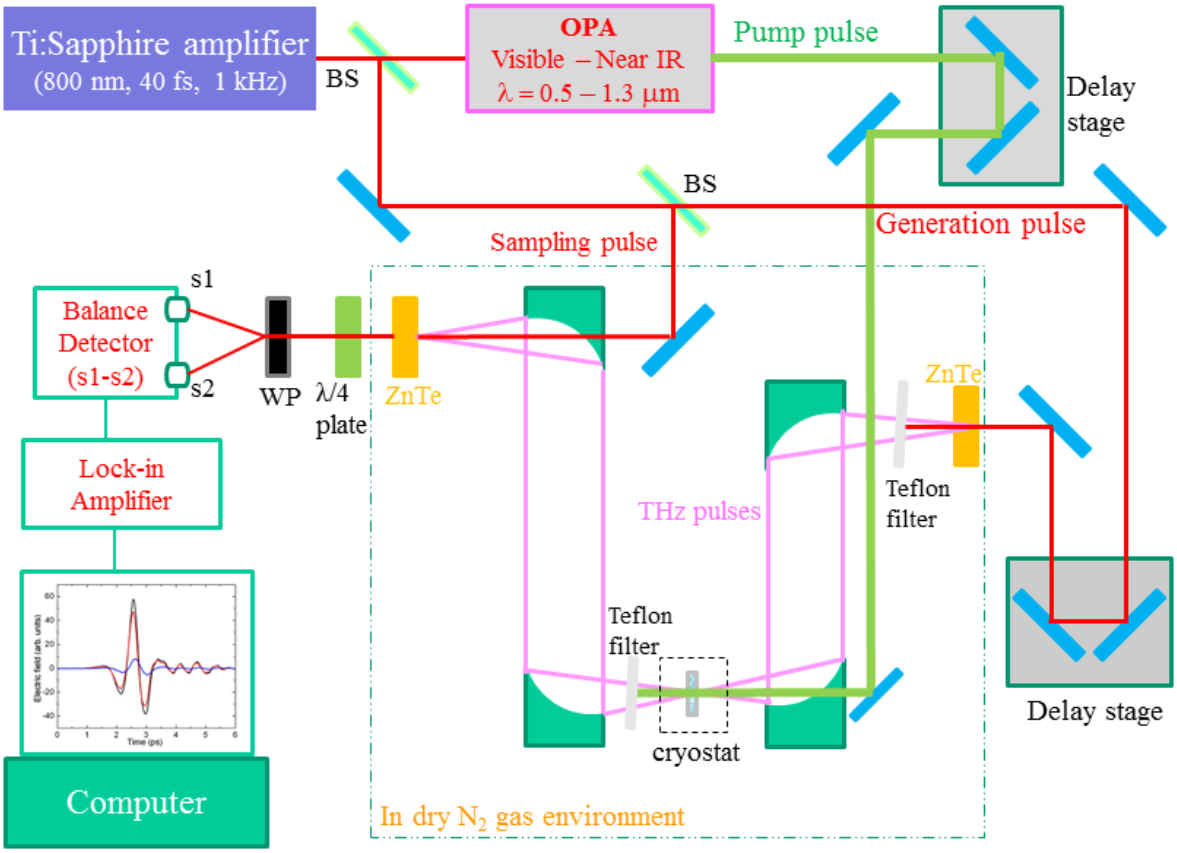

Figure 5.8 The schematic of the optical pump THz probe experimental setup. BS: beam splitter, WP: Wollaston prism. The THz section of the setup is purged with dry N_2 gas as shown in the dashed box.

T of the 572 nm (2.17 eV) light through the 50 μm thick sample via the relation T=exp(-$nd\alpha$). Details of the method can be found in Ref (87; 88). Our calculated FR following the method is ~0.88%. Therefore a simple relation $\tilde{\varepsilon}(\omega) \approx FR \cdot \tilde{\varepsilon}^{\mathrm{NT}}(\omega)$ is obtained for FR much smaller than 1 (82; 88; 89).

Representative ultrafast THz responses $\Delta\sigma_1^{\mathrm{NT}}(\omega)$ and $\Delta\varepsilon_1^{\mathrm{NT}}(\omega)$ are shown in Fig 5.10 (red dots) at $\Delta\tau$=0.5 ps and T=5 K, after 1.55 eV pumping with photon density 3.9×10^{14} cm^{-2} (96 μJ/cm^2). A strong photo-induced absorption appears in $\Delta\sigma_1^{\mathrm{NT}}(\omega)$ within the time resolution with a broad, resonant spectral shape centered at ~6 meV and a dispersive zero crossing occurs in $\Delta\varepsilon_1^{\mathrm{NT}}(\omega)$ at slightly lower photon energy. These two features are characteristic of a well-defined driven THz oscillator while the shift between their spectral positions and the non-

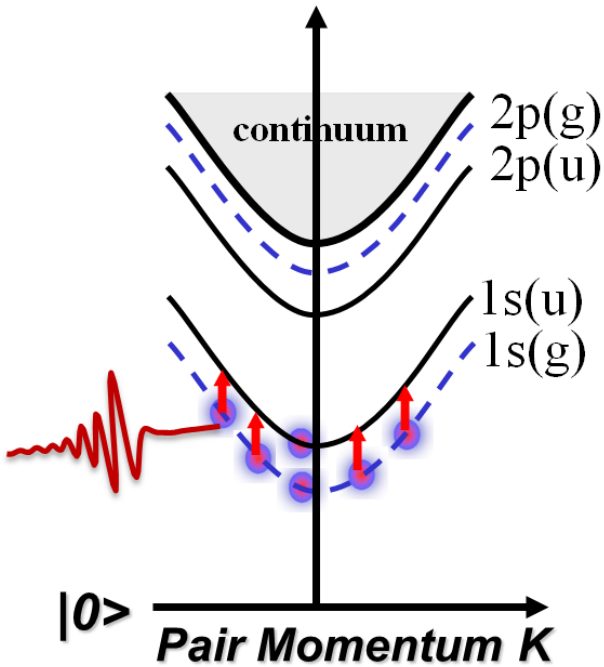

Figure 5.9 Schematic of two-particle e-h pair dispersion, illustrating the lowest-lying $1s(g) \rightarrow 1s(u)$ intraexcitonic transitions (red arrows) resonantly probed by THz pulses.

vanishing conductivity, albeit small, at the lowest probe energy ∼2 meV indicate additional low-frequency spectral weight, in the form of a coexisting unbound e-h plasma as discussed later. We emphasize three key facts to assign this resonance mainly from the $1s(g)\rightarrow 1s(u)$ transition of (6,5) tubes. First, resonant photoexcitation of the (6,5) interband E_{22} excitonic transitions at 2.17 eV, shown in Fig. 5.11(b), leads to significant enhancement of the transient THz resonance ∼6 meV, e.g., roughly three times as large as the 1.55 eV off-resonant excitation [Fig. 5.11(a)], for the same excitation photon density n=1.4×10^{14} cm^{-2} per pulse. This clearly shows the excitonic origins of the THz resonance in (6,5) tubes. Second, raising the initial lattice temperature to T=300 K [Fig. 5.11(c)] diminishes the resonance as compared to T=5 K [Fig. 5.11(b)], for the same resonant excitation. Third, the resonance occurs in the transparent region of the unexcited sample and is close to the $1s(g)\rightarrow 1s(u)$ transition energy of (6,5) tubes indirectly extrapolated in high field magneto-optical studies (74; 75).

For a quantitative analysis, a theoretical model is used to reproduce the experimentally determined complex THz dielectric functions. The model consists of two components: the THz

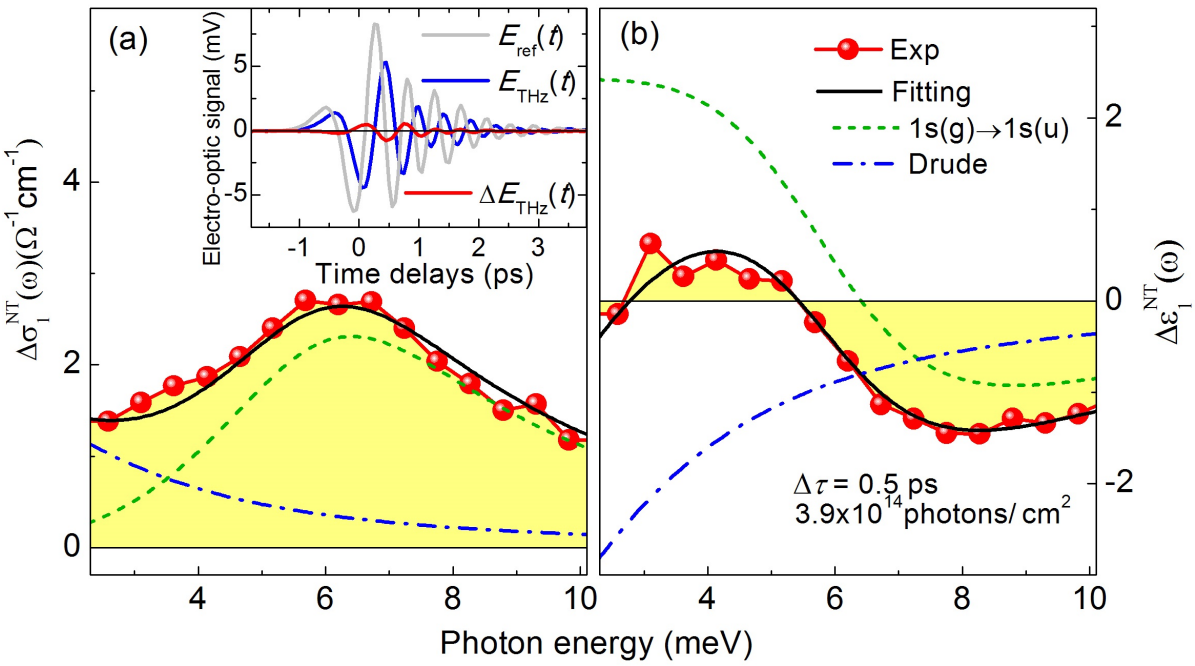

Figure 5.10 Photoinduced THz spectrum changes of (a) $\Delta\sigma_1^{\mathrm{NT}}$ and (b) $\Delta\varepsilon_1^{\mathrm{NT}}$ (red dots), measured at pump-probe delay $\Delta\tau$=0.5 ps after 1.55 eV pumping with fluence 96 μJ/cm^2 (3.9 $\times$ 10^{14} photons/cm^2) at T=5 K. The black line is the fit using the analytical model Equ. 5.12, which is the sum of the $1s(g) \rightarrow 1s(u)$ excitonic (dashed green line) and unbound e-h responses (dash-dotted blue line). Inset of (a): the corresponding transmitted THz time-domain fields through reference (a clear aperture) $E_{\mathrm{ref}}(t)$ (gray), unexcited sample $E_{\mathrm{THz}}(t)$ (blue), and its pump-induced change $\Delta E_{\mathrm{THz}}(t)$ (red).

dielectric function of the intra-excitonic transitions $\varepsilon^{1s}_{g\rightarrow u}(\omega)$ plus a Drude term of unbound e-h plasma $\varepsilon_{eh}(\omega)$:

$$\varepsilon^{\mathrm{NT}}(\omega) = \varepsilon^{1s}_{g\rightarrow u}(\omega) + \varepsilon_{eh}(\omega) = [\varepsilon_\infty + \frac{F^{1s}_{g\rightarrow u}}{(\omega^{1s}_{g\rightarrow u})^2 - \omega^2 - i\omega\Gamma}] - \frac{\omega_{\mathrm{p}}^2}{\omega^2 + i\omega\gamma}. \tag{5.12}$$

For the first component (Fig. 5.10, dashed green), $F^{1s}_{g\rightarrow u}$ denotes effective transition strength of the intra-excitonic $\omega^{1s}_{g\rightarrow u}$ resonance as $F^{1s}_{g\rightarrow u} = f^{1s}_{g\rightarrow u} \cdot (\triangle\omega_{\mathrm{p}}^2)^{1s}_{g\rightarrow u}$, where f is the oscillator strength and $\omega_{\mathrm{p}}^2 = ne^2/\varepsilon_0 m$. The $\triangle\omega_{\mathrm{p}}^2$ term, thereby, measures the population difference Δn between the lowest dark and bright pair states (Fig. 5.9), i.e., $\Delta n_{\mathrm{X}} = n^{1s}_g - n^{1s}_u$. The second, Drude component (Fig. 5.10, dash-dotted blue) is added with ω_{p}^2 proportional to the density of unbound e-h density n_{eh}. ε_0 and ε_∞ are the vacuum and background permittivity, and

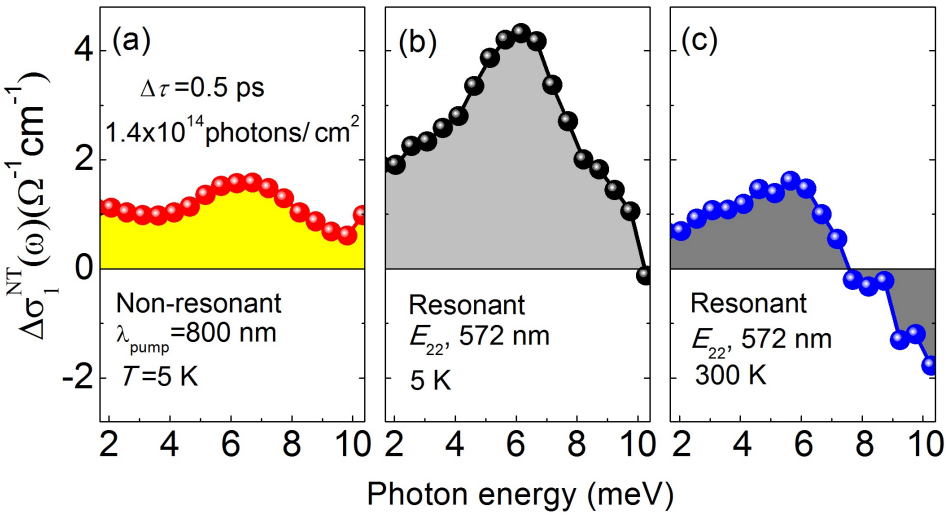

Figure 5.11 Comparison of photoinduced THz conductivity changes $\Delta\sigma_1^{\mathrm{NT}}(\omega)$ at $\Delta\tau$=0.5 ps and under an excitation density of $1.4\times10^{14}/\mathrm{cm}^2$ with (a) off-resonant excitation at 1.55 eV and T=5 K, (b) resonant excitation at 2.17 eV and T=5 K, and (c) resonant excitation at 2.17 eV and T=300 K.

e and m are the electron charge and the effective exciton (or electron) mass obtained from (90). Such composite THz response model (Fig. 5.10, solid black lines) provides an excellent agreement with the low temperature experiment (Fig. 5.10, red dots) by varying the $\omega_{g\to u}^{1s}$ and $F_{g\to u}^{1s}$, carrier density n_{eh}, and the exciton (carrier) broadening Γ (γ). The best fit are strongly restrained by the requirement of simultaneously satisfying both dielectric responses $\Delta\sigma_1^{\mathrm{NT}}(\omega)$ and $\Delta\varepsilon_1^{\mathrm{NT}}(\omega)$, over a broad spectral range, and by the distinctly different spectral shapes of the excitonic oscillator and Drude carriers.

5.3.3.1 Dark exciton formation and relaxation dynamics

Fig. 5.12 presents in detail of ultrafast THz spectra $\Delta\sigma_1^{\mathrm{NT}}(\omega)$ and $\Delta\varepsilon_1^{\mathrm{NT}}(\omega)$ for various time delays $\Delta\tau$ after the resonant E_{22} photoexcitation at 2.17 eV. Pump fluence is 48 μJ cm^{-2} and T=5 K. The transient spectra are characterized by the $\omega_{g\to u}^{1s}$ resonance that retains its shape as the amplitude decays with time. The resonance peaks indicated by the vertical dashed cyan line exhibit no noticeable shift. This shows clearly the dark excitons are formed within sub-ps time scale and very stable. The results can be fitted very well by the model described above (red lines). However, to further determine the exciton density $\Delta n_{\mathrm{X}} = (F_{g\to u}^{1s}/f_{g\to u}^{1s})\cdot(\varepsilon_0 m/e^2)$, the

oscillator strength f is needed for the $1s(g)\rightarrow 1s(u)$ transition which has never been determined before. This can be directly obtained via fluence dependence. Fig. 5.12(b) plots the ratio $R = F^{1s}_{g\rightarrow u} \cdot(\varepsilon_0 m/e^2)/(n_{\rm ph} - n_{eh})$ as a function of fluence down to 3 μJ cm^{-2}, where $n_{\rm ph}$ is the actual absorbed photon density after taking into account the reflection and transmission of the pump beam in the optical path. This ratio, with sufficiently weak photoexcitation, will converge to $f^{1s}_{g\rightarrow u}$ since most photo-generated E_{22} excitons will populate in the dark ground state $1s(g)$ during the THz pulse and $\Delta n_X \approx n_{\rm ph} - n_{eh}$. This condition is ensured due to fast inter-subband E_{22}-to-E_{11} relaxation ~40 fs (91), low transient excitonic temperature and strongly limited exciton-exciton annihilation (EEA) in dilute exciton gas (92). Indeed, the ratio shown in Fig. 5.12(b) exhibits strong pump power dependence and, with decreasing fluence below $\sim$ 10 μJ cm^{-2}, converges to a constant $f^{1s}_{g\rightarrow u} \approx 0.79$. Increasing pump fluence to 10s of μJ cm^{-2} leads to a significant drop of the ratio, which can be attributed to efficient EEA that lowers the photon-exciton conversion efficiency.

The obtained density $\Delta n_{\rm X}$ and its relaxation dynamics (black dots) are well described by a bimolecular decay shown in Fig. 5.12(c). Although it exhibits a highly non-exponential profile over ps time scales, a reciprocal plot of $1/\Delta n_{\rm X}(t)$, instead, yields a simple straight line, i.e., $1/\Delta n_{\rm X}(t) \sim \beta t$ (bottom panel, black dots), which is the hallmark of the bimolecular decay given by $\frac{\rm d}{\rm dt}\Delta n_{\rm X}(t) = -(1/2)\beta\Delta n^2_{\rm X}(t)$ with decay rate of sheet density β=2.3$\times$10^{-14} cm^2 ps^{-1} (68). The $1/n_{eh}(t)$ decay (red dots), on the contrary, show large variation from the bimolecular behavior, which further underscores the excitonic origin of the $\Delta n_{\rm X}(t)$ response. Furthermore, the strong similarity between the $\Delta n_{\rm X}$(t) decay and firmly established exciton kinetics in SWNTs also indicates that most excitons populate in the $1s(g)$ ground state and $\Delta n_{\rm X}$(t)$\approx n^{1s}_g$, under current experimental conditions, i.e., $n^{1s}_g \gg n^{1s}_u$. Here $\Delta n_{\rm X}$ thus quantitatively follows the $1s(g)$ exciton density, revealing particularly that the resonant photoexcitation generates n^{1s}_g ~90% of the total density, much larger than n_{eh} (Fig. 5.12(c), top panel).

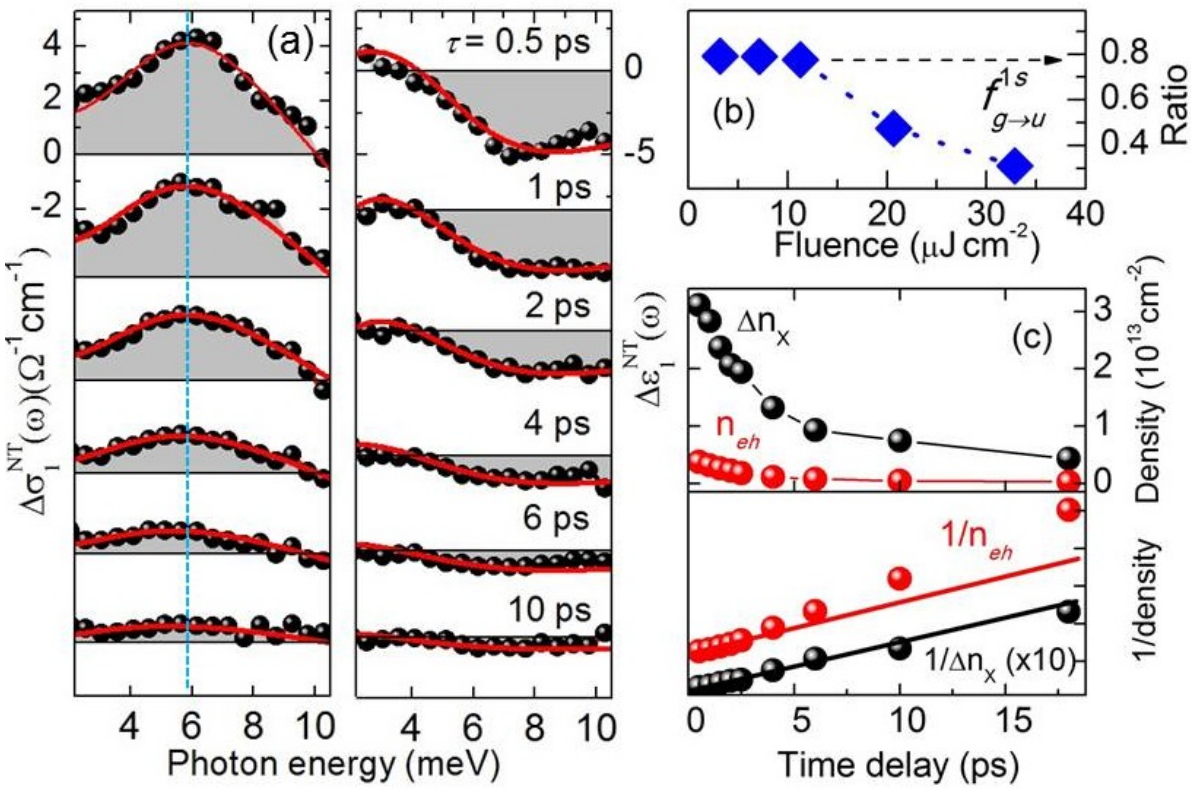

Figure 5.12 (a) Photoinduced THz spectrum changes $\Delta\sigma_1^{\mathrm{NT}}(\omega)$ and $\Delta\varepsilon_1^{\mathrm{NT}}(\omega)$ (black dots) at several pump-probe delays after resonant (6,5) E_{22} excitation at 2.17 eV and T=5 K. Shown together are the fitting (red lines) and peak positions indicated by the dashed cyan line. (b) The ratio $R = F_{g\to u}^{1s} \cdot (\varepsilon_0 m/e^2)/(n_{\mathrm{ph}} - n_{eh})$ as a function of pump fluence. (c) The temporal decay of exciton (Δn_{X}) and unbound plasma e-h (n_{eh}) densities as a function of time delay (top panel) and the reciprocal of Δn_{X} and n_{eh} density decay together with fitting (bottom panel). The traces in the bottom panel are vertically offset for clarity.

5.3.3.2 Dark exciton and free *e-h* plasma interaction and their density dependent renormalization

Increasing off-resonant excitation reveals the complex many-particle state. Fig 5.13 shows $\Delta\sigma_1^{\mathrm{NT}}(\omega)$ and $\Delta\varepsilon_1^{\mathrm{NT}}(\omega)$ for several pump fluences after 1.55 eV photoexcitation at T=5 K. The spectra at $\Delta\tau$=0.5 ps clearly exhibit the $\omega_{g\to u}^{1s}$ resonance, despite 100s of meV detuning away from the excitonic resonance, which dominates e-h plasma especially at low pumping. The sub-ps formation even with off-resonant excitation appears to be much more efficient than 2D/3D excitons that are strongly influenced by the co-existing unbound e-h plasma with 100s

of ps cooling time under the off-resonant pumping (93). The composite THz model (black lines) again consistently reproduces very well the experimental results, which are divided into individual components in the same manner as Fig. 5.10, i.e., the intraexcitonic $1s(g)\rightarrow 1s(u)$ (dashed green lines) and unbound e-h carriers (dash-dotted blue lines).

Note that the model described above starts to deviate from the experimental spectra at high temperature or large exciton density, e.g., the negative $\Delta\sigma_1^{\mathrm{NT}}(\omega)$ in the 300 K case in Fig. 5.11(c) and high pumping above 512 μJ/cm^2 in Fig. 5.13(a). This can be fully resolved by an additional contribution from a photo-bleaching of the absorption band centered at ∼4 THz (dashed pink lines), which were extensively described in the prior study (94) and will only be discussed briefly here: several prior studies in SWNTs have established an absorption band centered at ∼4 THz in SWNTs, which appears to be a "universal" feature in static THz spectra of SWNTs (88; 95). It is expected that the bleaching of this 4 THz oscillator only contributes significantly to the low energy transient spectra at high temperature or high pumping in our case. While it appears to be negligible in the low pumping case shown in Fig. 5.10. The origin of this transition is still somewhat unclear (88). This feature was first assigned to a pseudogap or electronic interband transitions between small gap nanotubes (95). Later, phonon (96) and plasmon resonance (97) were suggested as possible causes. It is out of scope of our study although our ultrafast low energy spectra and fittings indirectly confirmed again its existence.

Additionally, two salient features are visible with increasing pump fluence:

(i) The first feature is that the $\omega_{g\rightarrow u}^{1s}$ resonance in $\Delta\sigma_1^{\mathrm{NT}}(\omega)$ shifts to lower frequency [Fig. 5.13(b)], illustrated by two vertical dashed lines in Fig. 5.13(a), ∼20% change from 15 to 814 μJ cm^{-2}. We attribute this to the critical role of plasma-exciton interaction in the renormalization of the excitonic levels, considering the unbound e-h density significantly increases in the off-resonance pumping, e.g., n_{eh} can reach $\sim 2.5\times 10^{13}$cm^{-2}, comparable to exciton density, shown in Fig. 5.13(c). Note that the $\omega_{g\rightarrow u}^{1s}$ shift is not seen in the system of a predominant exciton population, shown in Fig. 5.12 for the resonant pumping, which has larger exciton density but one order of magnitude smaller n_{eh}. This helps reconcile some seemingly contradictory results regarding the exciton stability in the literature, e.g., photoluminescence spectra of dense excitons have shown no shift up to complete absorption saturation (69; 92), while ultra-violet

pumping results in some slight excitonic shifts (71) that can be confirmed here to free carrier generation.

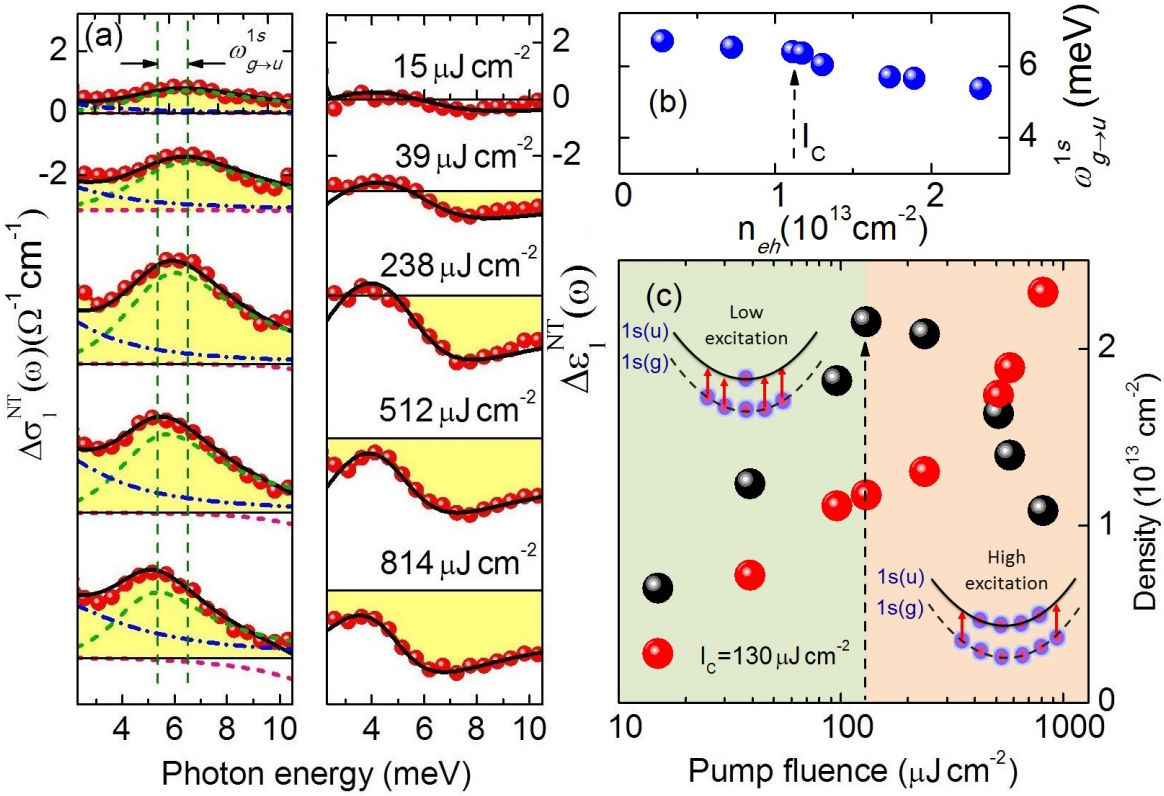

Figure 5.13 (a) Photoinduced THz spectrum changes $\Delta\sigma_1^{\mathrm{NT}}(\omega)$ and $\Delta\varepsilon_1^{\mathrm{NT}}(\omega)$ (red dots) at several pump fluences after 1.55 eV excitation, $\Delta\tau$=0.5 ps, and T=5 K. The fitting (black lines) is divided into individual components (see text) and the vertical dashed lines indicate the shift of the $1s(g)\to 1s(u)$ peak positions. (b) The resonance peak as a function of unbound e-h density. (c) Fluence dependence of the unbound e-h density (n_{eh}, red dots) and exciton density (Δn_{X}, black dots), which is divided into two regimes at I_C ~130 μJ cm^{-2} (dashed arrow).

(ii) The second feature is that the exciton density Δn_{X} exhibits a distinct non-monotonic variation with increasing excitation fluence [Fig. 5.13(c)], which peaks at I_C ~130 μJ cm^{-2} followed by a significant decrease with further increasing fluence (the same non-monotonic fluence dependence of the $\omega^{1s}_{g\to u}$ resonance is also observed with resonant E_{22} excitation, which can be similarly understood). However, most interestingly, the intra-excitonic resonance $\omega^{1s}_{g\to u}$ exhibits *little shift or broadening* at I_C [<5%, dashed arrow in Fig. 5.13(b)], indicating that there is *no obvious exciton ionization to unbound e-h plasma.* This is consistent with the

fact that the photoexcited exciton density is far below the expected Mott density in SWNTs (92). This appears to be fundamentally different from dense 2D and 3D excitons where the strong decrease of excitonic signals occurs *only* upon the ionization of excitons manifested by a significant shift, broadening, and ultimately the disappearance of the THz resonances. The quasi-1D many-body state in SWNTs reveal, instead, the evolution from a predominant dark exciton population in the $1s(g)$ to phase space filling of both the lowest dark and bright exciton pair states. Such crossover at I_C is illustrated by two shaded colors in Fig. 5.13(c): below I_C, photoexcited excitons primarily populate in the lowest lying dark state $1s(g)$ that leads to a rapid rise of Δn_{X} with increasing pump fluence; above I_C, photoexcited excitons have larger probability to populate the $1s(u)$ state rather than the $1s(g)$ ground state, due to electronic heating of the many-body systems, which is responsible for the reduction of the $\omega^{1s}_{g\rightarrow u}$ resonance via Pauli blocking of the transition. The $1s(g)/1s(u)$ exciton pairs, being protected by the symmetry and 1D correlation, is stable against high density ionization. They are well-isolated from higher lying np exciton levels (n>2) and continuum (>200 meV) (66; 67; 70).

5.4 Discussion

5.4.1 Excitons vs. phonons

In this section, we clearly exclude the existence of the photoinduced infrared-active phonon mode as an alternative interpretation of our observed resonance centered at $\sim$ 6 meV instead of the dark excitons.

First, the phonon scenario would require observing at least one of the following two features: either there is any phonon resonance already in the static conductivity spectrum or periodical oscillations superimposed in the photoinduced temporal scan traces. However, both these features are absent in our raw data. A good example of phonon modes in static conductivity spectra is Ref (98) in which the transition metal oxide VO_2 was studied. In Fig. 1(a) of Ref (98), VO_2 shows three obvious phonon peaks in the insulating phase (blue circles) at 50, 62, and 74 meV. VO_2 at higher temperatures becomes a metal accompanied by a peculiar structural phase transition and much smaller phonon resonant amplitudes that are clearly inappropriate

to compare with the SWNT physics in our paper. Authors in the paper interpret "pump-induced THz conductivity [in some regions]...solely from electronic [origins]..." instead of a phonon mode, because the authors further stated "...since spectral region E [>85 meV] is free of phonon resonances" in the *equilibrium* conductivity as shown in Figs. 1(a) and 2(a) of the paper for the 295 K case. On the contrary, the static conductivity spectra of SWNTs in our work shows no resonant spectra in the static state at either 5 K or room temperature, as shown in Fig. 5.14(a). Another example is Ref. (99) in which photoexcited Bi samples show strong phonon oscillations in the transient reflectivity as shown in Fig. 1 of Ref (99). Similarly, VO_2 also shows phonon oscillations in the temporal scan, as shown in Fig. 3(a) of Ref (98). On the contrary, our raw time scan trace [Fig. 5.14(b)] does not show any phonon oscillation feature. In fact, our observation is similar to Fig. 3(b) of Ref (98), where the signal is assigned to electronic origins instead of phonons by the authors.

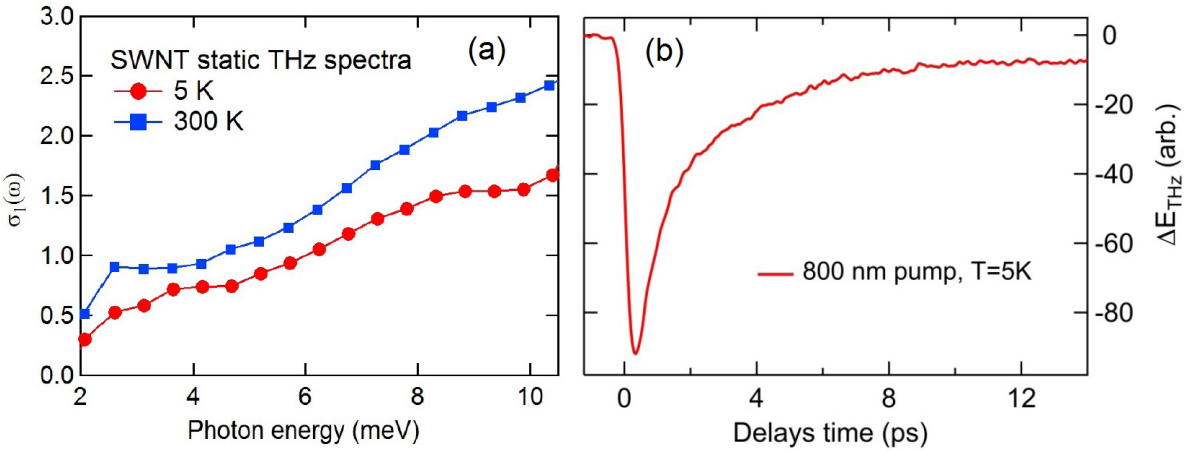

Figure 5.14 (a) Static THz conductivity spectra of SWNTs at T=5 K and room temperature. (b) 800 nm photoinduced transient transmission THz field change of SWNTs at T=5 K.

Second, there are several additional features in our observation that are very difficult, if not impossible, to be consistently explained by phonons, e.g., the non-monotonic pump fluence dependence in our resonance signals [Fig. 5.13(c)] strongly contrast with the monotonic increase before saturation that one would expect with phonons, e.g., Ref (99); the bi-molecule decay profile observed in our study [Fig. 5.12(c)] is the hallmark of exciton-exciton annihilation in SWNTs, which is distinctly different from the density decay of e-h plasma and clearly

underscores the excitonic origin of the THz resonant response; the excitonic enhancement seen in our signals from the interband resonant pumping [Fig. 5.11] is inconsistent with the phonon scenario because the off-resonant excitation should heat up the system more and lead to more pronounced phonons.

Finally, our observed resonant position matches well to the energy of intraexcitonic transition $1s(g)\rightarrow 1s(u)$ reported by static magneto-optical studies, both theoretically and experimentally as shown in our study. To the best of our knowledge, we are not aware of any SWNT phonon modes that can explain our observed spectra.

5.4.2 Non-equilibrium excitonic correlations vs. thermalization

In this section, we further discuss the consistency of our observed fast formation of the $1s(g)\rightarrow 1s(u)$ transition within 100s fs and the slow thermalization between $1s(g)$ and $1s(u)$ states on the order of tens-to-hundreds of ps as seen by time-resolved PL studies (100). Particularly, we would like to concisely clarify that our results are fully consistent with the existing PL literature in SWNTs. Most importantly, ultrafast intraexcitonic $1s(g)\rightarrow 1s(u)$ transitions reported here represents both a direct consequence and measure of *e-h* pair correlations and resulting *dark* ground states at their initial highly *non-equilibrium* and *non-thermal* timescales. However, time-resolved or static PL measurements are only sensitive to the existence of *bright* excitons and only detect a subset that are *thermalized near the zone center K=0* because of the small angular momentum of the emitting photons. Our THz technique, being independent of ground state symmetry and momentum conservation restrictions, allows for studying *ultrafast formation* of dark excitons and *non-equilibrium* pair correlation across the entire K space which is extremely difficult, if not impossible, to be obtained from PL measurements. Specifically:

(i) Dark exciton formation: our THz data reveals a new ultrashort sub-ps *formation* time, which is much faster than the 100s ps *thermalization* times seen in the PL measurements. This is fully consistent with the literature and can be easily understood as follows. As revealed extensively in 2D semiconductor quantum wells (101), exciton formation has two very different time scales: an ultrafast formation within 1 ps by electronic correlation even with off-resonance excitation and a slower one of 100s of ps from thermalization and cooling of unbound transient

carriers into to the lowest excitonic ground state. The PL is extremely limited to measurements of the fast formation of the initial non-equilibrium correlated states from dark excitons as discussed above and mostly detects the bright excitons and their slow thermalization to the excitonic ground states. These two timescales characterize two processes with completely different formation mechanisms: *non-thermal* electronic pair correlation at fs vs. thermalization/cooling at ps timescales.

(ii) Low temperature PL in SWNTs and their poor quantum efficiency (QE): The PL emission in SWNTs appears due to the long thermalization process. Our THz data shows that the initial fast, sub-ps formation process from the electronic pair correlation leads to substantial larger population of the dark $1s(g)$ excitons compared to bright $1s(u)$ excitons under low pump fluence. The slowly thermalized, small bright exciton population gives rise to some detectable PL at all temperatures but with very poor QE, well established in many PL literature of only $\sim 10^{-4} - 10^{-3}$ (102; 103). Our picture here should not be confused with the simple scenario of the thermalized exciton states. Using the existing low temperature time-averaged PL measurement (104), one can easily estimate the population ratio between $1s(u)$ and $1s(g)$ $\sim 0.06 - 0.08$ depending on conditions, i.e., substantial larger population of dark excitons that strongly consolidate the validity of our results. One should also note that PL measurements mostly over-estimate this ratio since it depends on the time-averaged decay near the zone center, while our THz intra-excitonic probe measures genuine non-equilibrium excitonic population cross all of the K space at initial times. We believe that the strongly enhanced electronic correlation and reduced screening in 1D SWNTs regulate exciton formation at the lowest $1s(g)$ state, which dominate any other mechanisms such as carrier cooling for either resonant or off-resonant pumping especially at low pumping, e.g., below the cross-over fluence I_C identified in our paper. This shines novel insights into exciton physics and non-equilibrium pair correlation in SWNTs beyond the existing literature.

5.5 Summary and Outlook

In summary, we provide the first insights into the chirality-specific THz response of ground state dark *e*-*h* pair correlation and dynamics in SWNTs. The ultrafast dark exciton physics

and probes revealed, being independent of ground state symmetry and momentum conservation restrictions, motivate further studies to identify exactly how strongly-enhanced electronic correlation and reduced screening regulate the 1D exciton formation. This may evolve into a benchmark approach for quantitative exciton management in SWNT-based device development, and motivates for fundamental quantum phase discovery of excitons (79) and other strongly correlated excitations (105; 106).

One of the future interesting experiments is to study the time-resolved transient exciton scattering rate change which determines the intraexcitonic transition bandwidth. It is known that after photoexcitation excitons are formed quickly due to strong electronic correlation. The non-equilibrium and non-thermal excitons will populate primarily $1s(g)$ state for all possible momentum K. Therefore THz probe can measure a broadband intraexcitonic transition $1s(g) \rightarrow 1s(u)$ centered at $\sim$6 meV. The $1s(g)$ and $1s(u)$ energy gap is momentum K dependent due to different band structures of the 2 states. After hot excitons at large momentum K cool down to the bottom with very small K and EEA decreases exciton population, the intraexcitonic transition will lead to a narrower bandwidth due to the reduction of exciton density and the fact that more and more excitons gather at the bottom with similar momentum K. However, some of our preliminary experimental results show the opposite trend, i.e., the bandwidth gets broader. This observation may imply that the more exciton there are, the more they intend to gather in K space. This may finally leads to the Bose-Einstein condensate of dark excitons in SWNTs if the exciton density is large enough and the trend keeps to be valid. In order to create much more excitons, we certainly need much higher pump fluence, which is currently not available, but this is one of our recent plans to achieve higher pump fluence in order to confirm this phenomena.

CHAPTER 6. ON-GOING PROJECTS

In this chapter, I briefly summarize several on-going projects performed by the NIR- or MIR-pump and THz-probe spectroscopy experiments. We would like to study low energy electrodynamics of complex materials, which is poorly understood so far. The first on-going project is to understand the coupling mechanism and carrier transport dynamics of two spatially separated insulating bulk and conducting surface states in the topological insulator Bi_2Se_3 at different lab conditions, e.g., different lattice temperature and different photoexcitation wavelength. This project is well-going so far and a significant progress has been made. The next two on-going projects are to study temperature-dependent THz responses of $BaMn_2As_2$ and wavelength/polarization-dependent THz responses of valleytronic material of MoS_2 monolayer and bilayer. These projects are not complete yet, all results and interpretations presented in this chapter represent our best understanding of the results so far.

Specifically, this chapter starts with an introduction to topological insulators and then moves on to the sample preparation and characterization. Next, preliminary experimental results are presented and discussed. Finally, this chapter ends with a brief introduction and some experimental observations of THz probes of $BaMn_2As_2$ and MoS_2 at different lab conditions.

6.1 Ultrafast Terahertz Electrodynamics of Dirac Fermions in Topological Insulator Bi_2Se_3 with Mid-infrared Excitation

In this section, I present ultrafast THz spectroscopy study of topological insulator Bi_2Se_3 after Mid-infrared (MIR) excitation. Excitation wavelength and lattice temperature dependent measurements reveal distinct THz response dynamics and surface-bulk coupling mechanism.

6.1.1 Introduction

Topological insulators (TIs) represent a new state of quantum matter, which attract a lot of recent attentions. One unique property is that they have an insulating bulk state with a few 100s meV bandgap in its interior and a Dirac-cone-like conducting state on its surface which is protected by time-reversal symmetry (107). One key current issue is to understand the low energy electrodynamics and charge transfer mechanism between the conducting Dirac state and the spatially separated insulating bulk state. The schematic of the energy dispersion of a typical TI is shown in Fig. 6.1. The surface state (yellow) has Dirac conic structure with zero bandgap and the bulk bands (violet), like doped semiconductors, have a few hundreds meV energy gap. The dashed line indicates the position of the Fermi level.

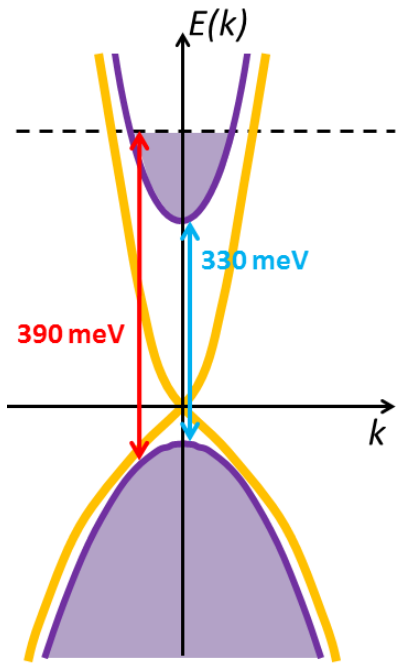

Figure 6.1 Schematic of the energy dispersions of a typical TI. The energy scale bars indicate the energy levels of one of the Bi_2Se_3 TI samples that we have studied and presented in this section.

Our ultrafast MIR pump and THz probe spectroscopy study reveals different responses of THz time-domain fields and conductivities with above- and below-bandgap photoexcitation and different lattice temperatures at T=5 K and T=300 K respectively. It allows to revealing the different bulk-surface coupling mechanism at different temperatures. The demonstrated

approach provides a versatile and powerful spectroscopic tool to investigate the intrinsic Dirac fermion physics in 3D TIs.

6.1.2 The sample preparation and characterization

We study molecular beam epitaxy (MBE) grown topological insulators. We have studied several different TI samples such as Bi_2Se_3 and Bi_2Te_3 with a series of thickness on different substrates. The ones we mostly study are 40 quintuple layers (QLs) of Bi_2Se_3 on a 0.5 mm thick sapphire substrate, and 140 QLs of Bi_2Se_3 on a 0.5 mm thick GaAs substrate. The results presented in this chapter mainly focuses on the first sample (40 QLs Bi_2Se_3/sapphire), which is shown to have a direct bandgap of ∼330 meV (108) (cyan line as shown in Fig. 6.1). In addition, Fourier transform infrared spectroscopy (FTIR) measurement indicates this sample has a bandgap from the top of valence band to the Fermi level of ∼390 meV (red line).

A static THz measurement of the Bi_2Se_3/sapphire sample is shown in Fig. 6.2. The static conductivity $\sigma_1(\omega)$ and dielectric function $\varepsilon_1(\omega)$ are extracted by using the fast Fourier transformation and Fresnel equation as discussed in section 2.3.3. The $\sigma_1(\omega)$ shows a clear Drude feature plus an optical phonon mode centered ∼1.9 THz. The results are consistent with previous static THz measurement of Bi_2Se_3 (109; 110).

6.1.3 Experimental setup and results

The experimental setup is essentially the same as that used for SWNTs experiments as discussed in Fig. 5.8 of Section 5.3.2. In this experiment, the MIR beam is generated from the OPA through the DFG of both signal and idler beams from a GaSe crystal.

THz time-domain fields transmitted through the pure sapphire substrate $E_{\mathrm{ref}}(t)$, the Bi_2Se_3/ sapphire sample $E_{\mathrm{THz}}(t)$ and its pump-induced change $\Delta E_{\mathrm{THz}}(t, \Delta\tau)$ at various pump-probe delays $\Delta\tau$ are recorded. Similarly, through the fast Fourier transformation and Fresnel equation, the photoinduced THz conductivity changes $\Delta\sigma_1(\omega, \Delta\tau)$ and dielectric function changes $\Delta\varepsilon_1(\omega, \Delta\tau)$ at various pump-probe delays $\Delta\tau$ are obtained simultaneously. The bandgap of the sample from the valence band to the Fermi level is 390 meV as revealed by the FTIR measurement and is also confirmed by our wavelength-dependent pump-probe temporal scans

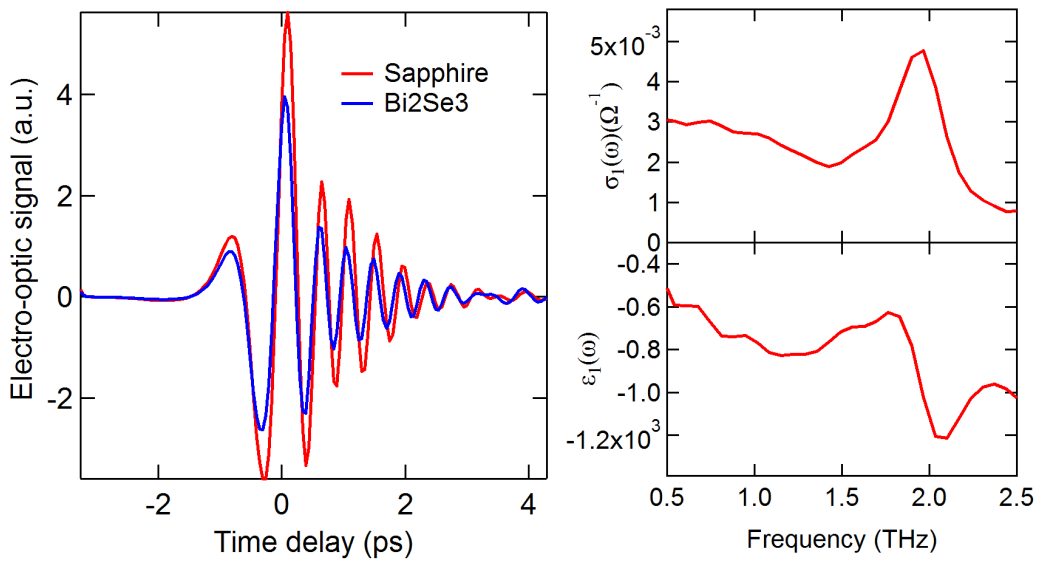

Figure 6.2 Static THz fields transmitted through a sapphire substrate (red, left panel) and 40 QLs Bi_2Se_3/sapphire sample (blue, left panel). On the right panel are the extracted static conductivity $\sigma_1(\omega)$ and dielectric function $\varepsilon_1(\omega)$ of the sample.

which show clearly two distinctly different relaxation dynamics with above- and below-bandgap photoexcitations. Specifically, with above- and below-bandgap photoexcitation at 3.15 μm (394 meV) and 4.5 μm (276 meV) respectively, we see distinctly different THz response dynamics. Fig. 6.3 shows the temporal scans of photoinduced THz transmission changes $\Delta E_{\mathrm{THz}}(\Delta\tau)$ after 3.15 μm (upper panel) and 4.5 μm (bottom panel) excitation at several fluences. With above-bandgap excitation, $\Delta E_{\mathrm{THz}}(\Delta\tau)$ has an initial rapid sub-ps rising and then changes to a fast drop in transmission with a time scale of $\sim$1 ps. The peak amplitudes of $\Delta E_{\mathrm{THz}}(\Delta\tau)$ increase with pump fluence. But the signal size decays quickly and after $\sim$15 ps the sizes for all fluences merge together indicating the saturation of the THz slow responses. Two different relaxation components after photoexcitation are observed: (i) the fast component which is fluence dependent and decays within several ps and (ii) the slow component which is independent of the initial excitation fluence and decays in a time scale of several 100 ps. On the other hand, with below-bandgap excitation, the THz responses have similarly a rapid rising within sub-ps. It follows by a slow drop and decay. Only scans with fluence greater than 10 μJ/cm^2 merge together after $\sim$10 ps. The scans with less fluence do not merge together after a couple of 100 ps when they decay to equilibrium state, which is totally different from the above-bandgap

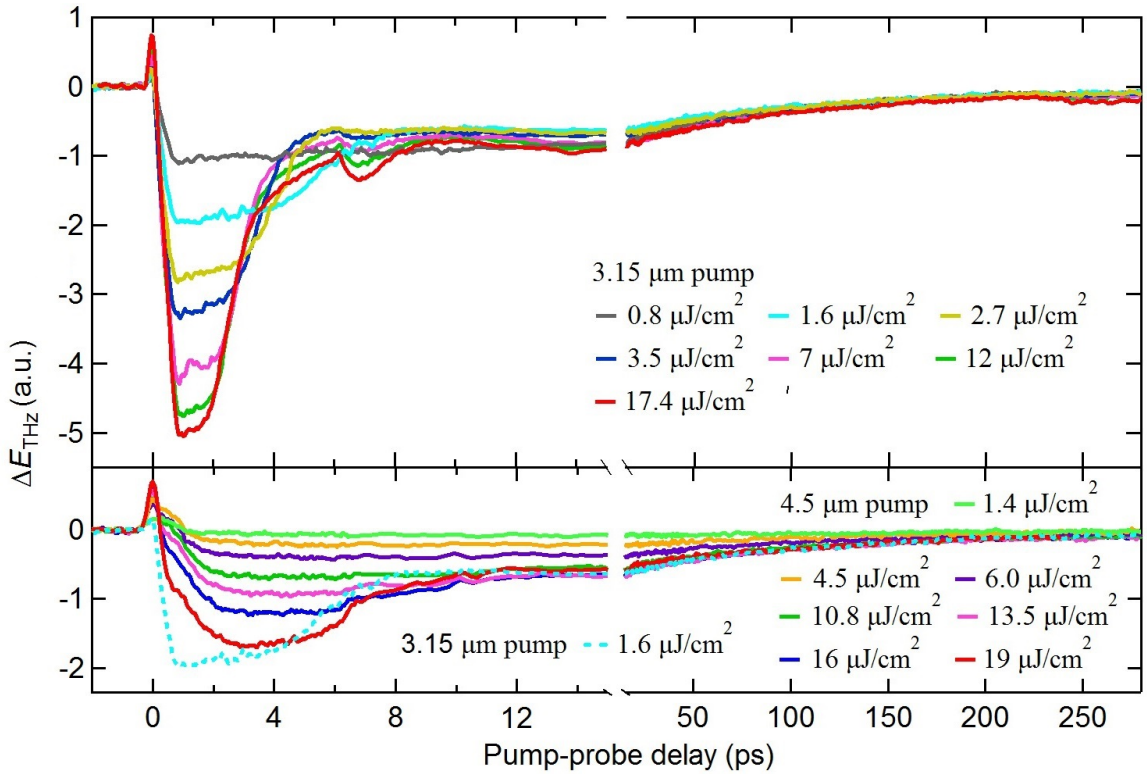

Figure 6.3 Temporal scans of transmitted THz field changes after 3.15 μm (top panel) and 4.5 μm (bottom panel) photoexcitation at several fluences. One of the 3.15 μm pump-probe scans from the top panel (1.6 μJ/cm^2, cyan line) is also plotted in the bottom to compare the signal of above- and below-bandgap excitations.

excitation. One of the above-bandgap excitation scan (1.6 μJ/cm^2, cyan line) is also plotted in the bottom panel in order to compare it with the signal of below-bandgap excitation. It shows that the amplitude of the above-bandgap excitation at 1.6 μJ/cm^2 is larger than all below-bandgap excitations with fluence up to 19 μJ/cm^2. Interestingly, its decay merges with that of the below-bandgap excitation with relatively high fluence (larger than 10 μJ/cm^2) after $\sim$10 ps. This reveals the fact that the relaxation dynamics of the slow component from below-bandgap excitation with high fluence has the same mechanism as that of the above-bandgap excitation, which is interpreted from the two photon absorption (TPA). For below-bandgap excitation with fluence greater than 10 μJ/cm^2, the TPA is efficient which can compete with the above-bandgap excitation with low fluence. Thus, $\Delta E_{\mathrm{THz}}(\Delta\tau)$ from below-bandgap excitation with fluence greater than 10 μJ/cm^2 reaches saturation and they merge together after

∼15 ps. Further increasing the fluence only increases the amplitude of the fast component like the above-bandgap excitation case.

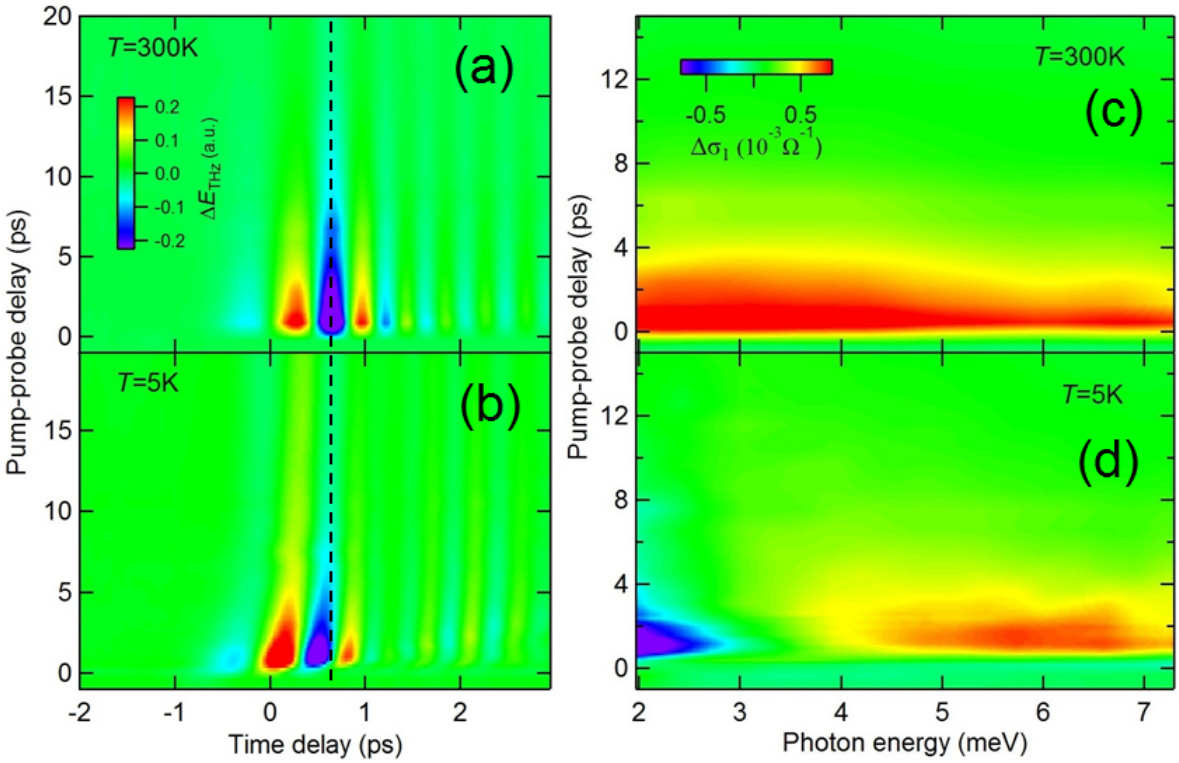

Figure 6.4 Photoinduced THz time-domain field change $\Delta E_{\mathrm{THz}}(t, \Delta\tau)$ at (a) T=300 K and (b) T=5 K after 5 μm excitation with various pump-probe delays. The corresponding photoinduced conductivity change $\Delta\sigma_1(\omega, \Delta\tau)$ at (c) T=300 K and (d) T=5 K.

Next, we compare temperature-dependent THz responses. The THz time-domain field changes $\Delta E_{\mathrm{THz}}(t, \Delta\tau)$ after below-bandgap excitation at 5 μm (248 meV) at various pump-probe delays $\Delta\tau$ and at T=300 K and 5 K are plotted in Figs. 6.4(a)(b) respectively as a 2D false-color plot. It shows the phase of the THz field change $\Delta E_{\mathrm{THz}}(t, \Delta\tau)$ at T=300 K does not have a noticeable shift while that at T=5 K has a significant shift at the early ∼20 ps as indicated by the dashed vertical line. This shift leads to the THz transmission change from negative at 300 K to positive at 5 K at some spectral range, which is confirmed by the conductivity change $\Delta\sigma_1(\omega, \Delta\tau)$ as pure positive for T=300 K indicating the dissipative response only. On the contrary, $\Delta\sigma_1(\omega, \Delta\tau)$ at T=5 K has photoinduced bleaching, i.e., negative conductivity, at low THz photon energy (2-3.5 meV) within the first ∼7 ps pump-probe delay

indicating photoinduced transmission increase for THz photon below 3.5 meV, and it changes to a pure positive Drude response after ∼20 ps. The temperature-dependent THz responses can be understood as effective phonon-assisted surface-bulk coupling at higher temperature (300 K), where the bulk insulating states with much larger carriers suppress surface states and dominate the THz response. However, at 5 K the surface-bulk coupling is ineffective due to the suppression of phonons at low temperature (111), leading to the THz response of both surface and bulk states. The negative conductivity is a signature of photoexcited Dirac cone states which is from the photoinduced increase of the scattering rate of Dirac Fermions (110).

Next, we will work more closely on the theoretical modeling of the THz spectra to extract, e.g., the scattering rates of the surface and bulk states respectively by using 2 Drude model. From the scattering rate changes, we are able to have deeper understanding of the carrier coupling between the surface and bulk states.

6.2 Other On-going Projects

In this section, I will briefly introduce the progress of some other on-going projects, e.g., the study of temperature-dependent THz responses of $BaMn_2As_2$ from 5 K to 300 K and wavelength- and polarization-dependent THz responses of valleytronic material of MoS_2 monolayer and bilayer.

The $BaMn_2As_2$ displays coupled antiferromagnetic and structural transitions (112). The static THz transmission of $BaMn_2As_2$ shows strongly temperature dependence. We observed that at low temperature 5-140 K, the THz transmission does not change with temperature. While when temperature increases from 140 K to 300 K, the THz transmission increases in a super linear trend. And the static THz conductivity measurement shows that the sample has clearly a Drude component plus a Lorentz oscillator centered at ∼2.3 THz. This feature shows weak temperature dependence. The high frequency side of the oscillator is a bit out of our 1 mm ZnTe probe range. In order to have broader bandwidth, GaSe or thinner ZnTe may need to be used. The photoexcited THz response of the sample is a bit weak, we could not have some clear conclusion yet. One thing we could do in future is to increase the THz bandwidth to observe the complete oscillator feature.

The transition metal MoS_2 has attracted great attention recently because of its unique electronic and optical properties. The monolayer MoS_2 is also a promising material for valleytronics. By using left- and right-circularly polarized light, we can selectively excite different excitonic states. In our optical pump and THz probe experiment, we use left-circularly polarized light at 660 nm to excite the MoS_2 bilayer and find it has very small transient THz conductivity at low frequency, which means the product after photoexcitation is insulating, very likely to be from excitons. But the sample is very thin which results in very weak photoinduced signal, this makes data analysis hard. One thing we could do in future is to compare the THz response from bilayer and monolayer samples.

CHAPTER 7. SUMMARY

To summarize, ultrafast time-resolved pump-probe spectroscopy is employed to study ultrafast THz electrodynamics of photonic and electronic nanostructures. Ultrafast THz pulses are the ideal spectroscopic tool to investigate many outstanding scientific phenomena, such as carrier interaction, cooling, transition, and transport, etc. A lot of recent progresses in ultrafast spectroscopy, medical/security imaging, device fabrication, failure analysis, components analysis, quality control, and others greatly reply on the development of THz technology.

One of my projects is to expand the THz spectroscopy technique toolbox, such as the development of the novel, high efficiency, and compact THz wave emitter. It is a big progress for the exploration of artificial-magnetism-induced nonlinear THz emission. This emitter has advantages that the conventional emitters cannot compete. For example, it can be pumped at any wavelength by tailoring the magnetic dipole resonance, but no current solid state THz emitters have this merit and they are limited by the delicate phase-match requirement. Moreover, the SRR emitter can potentially generate THz waves covering the entire THz band by shortening the pump pulse duration, because the SRR emitter does not suffer from the intrinsic limitation of the Reststrahlen region. To the best of our knowledge, all solid state THz emitters have phonon absorptions in THz band. On the other hand, even though our SRR emitter has much larger second-order nonlinear efficiency than conventional nonlinear media, it is only nanometer thick, which cannot fully compete with the conventional nonlinear crystals of thousands times thicker at this stage regarding the total THz emission intensity. It can be one of the future objectives to design and fabricate even higher efficiency THz emitter, and 3D SRR emitters in order to greatly improve the THz emission intensity.

Controlling THz waves effectively is another very important area for the application of THz technology. In our study, 1D and 2D photo-imprinted photonic structures are designed to

manipulate THz waves. According to observation, the THz wave modulation is from the first-order diffraction of the photo-imprinted diffractive elements. This can be used as THz wave filter and THz grating. We have also designed some structures for resonance manipulation, but are unable to observe THz resonance yet, e.g., from the circulating current of the SRRs. One of the major limitations for us to observe resonance is from the resolution and contrast ratio of the illuminated and dark regions of the GaAs. As measured by our camera, the contrast ratio is only around 100. The dark region is not really completely dark due to diffraction. The current numerical aperture is $\sim$0.1. We certainly need to improve our numerical aperture in order to achieve higher image quality closer to diffraction limit. But this is limited by some other facts, such as the configuration of the THz setup. It requires the modification of the current THz setup a lot.

THz spectroscopy technique is also employed to study low energy THz electrodynamics of dark excitons in semiconducting carbon nanotube. Carbon nanotubes have very good physical and optical properties and bright potential applications in many areas. However, most photo-generated carriers in semiconducting carbon nanotubes are dark excitons. They do not couple to a photon directly and limit free carriers to form current. This greatly limits the fluorescence- and optoelectronic-based applications of carbon nanotubes. Our THz study reveal the formation of lowest-lying dark excitons in semiconducting carbon nanotubes within 1 ps time scale regardless of the excitation wavelength due to strong 1D confinement and electronic correlation of electrons and holes. Resonant excitation leads to 90% of the products being dark excitons and one order of magnitude smaller free carriers. By tuning excitation wavelength away from excitonic transitions, free carriers with population comparable with that of dark excitons can be generated. Under such a condition, dark excitons are still very stable, but the intraexcitonic transition gap is renormalized due to the interaction of excitons and free carriers. In other words, the $1s(g)\rightarrow 1s(u)$ transition frequency shifts to smaller value with the increasing of free carrier population. Another interesting feature observed is that the photogenerated excitons will evolve from a predominant dark exciton population in $1s(g)$ at low excitation fluence to phase-space filling of both the dark $[1s(g)]$ and bright $[1s(u)]$ exciton states. Simply put, the photogenerated excitons will primarily populate at the lowest dark exciton states with low ex-

citation fluence, but they will have greater probability to populate at the upper bright exciton states at strong excitation fluence. One of the future interesting THz spectroscopy experiments on SWNTs is to study the time-resolved transient exciton scattering rate change which determines the intraexcitonic transition bandwidth. We have already observed some trend of the exciton collective effects. If this can be confirmed, by using much higher excitation fluence, it may indicate the realization of the Bose-Einstein condensate of excitons in SWNTs.

Bibliography

[1] R. Kohler *et al.*, *Nature* **417**, 156 (2002).

[2] M. Tonouchi, *Nat. Photon.* **1**, 97 (2007).

[3] B. Ferguson and X. C. Zhang, *Nat. Mater.* **1**, 26 (2002).

[4] G. L. Carr *et al.*, *Nature* **420**, 153 (2002).

[5] Y.-S. Lee, *Principles of Terahertz Science and Technology*, (Springer, 2009).

[6] R. W. Boyd, *Nonlinear Optics*, (Academic Press, Burlington, 2008).

[7] P. C. M. Planken, H. K. Nienhuys, H. J. Bakker, and T. Wenckebach, *J. Opt. Soc. Am. B* **18**, 313-317 (2001).

[8] Y. Liu and X. Zhang, *Chem. Soc. Rev.* **40**, 2494 (2011).

[9] D. R. Smith, J. B. Pendry and M. C. K. Wiltshire, *Science* **305**, 788 (2004).

[10] C. M. Soukoulis and M. Wegener, *Nat. Photon.* **5**, 523 (2011).

[11] B. S. Williams, *Nat. Photon.* **1**, 517 (2007).

[12] G. Scalari *et al.*, *Laser Photon. Rev.* **3**, 45 (2009).

[13] D. Mittleman, *Sensing with Terahertz Radiation*, (Springer-Verlag, Berlin, 2003).

[14] C. Kubler, R. Huber and A. Leitenstorfer, *Semicond. Sci. Technol.* **20**, S128 (2005).

[15] D. J. Cook and R. M. Hochstrasser, *Opt. Lett.* **25**, 1210 (2000).

[16] K. Y. Kim, A. J. Taylor, J. H. Glownia and G. Rodriguez, *Nat. Photon.* **2**, 605 (2008).

[17] S.-P. Han *et al.*, *Opt. Express* **20**, 18432 (2012).

[18] D. K. Polyushkin, E. Hendry, E. K. Stone and W. L. Barnes, *Nano Lett.* **11**, 4718 (2011).

[19] M. Kauranen and A. V. Zayats, *Nat. Photon.* **6**, 737 (2012).

[20] W. J. Padilla, A. J. Taylor, C. Highstrete, M. Lee and R. D. Averitt, *Phys. Rev. Lett.* **96**, 107401 (2006).

[21] H.-T. Chen *et al.*, *Nature* **444**, 597 (2006).

[22] N.-H. Shen *et al.*, *Phys. Rev. Lett.* **106**, 037403 (2011).

[23] I. Chatzakis *et al.*, *Phys. Rev. B* **86**, 125110 (2012).

[24] C. M. Soukoulis, S. Linden and M. Wegener, *Science* **315**, 47 (2007).

[25] V. M. Shalaev, *Nat. Photon.* **1**, 41 (2007).

[26] N. I. Zheludev, *Science* **328**, 582 (2010).

[27] I. Chatzakis, *Appl. Phys. Lett.* **103**, 043101 (2013).

[28] M. W. Klein, C. Enkrich, M. Wegener and S. Linden, *Science* **313**, 502-504 (2006).

[29] S. Linden, F. B. P. Niesler, J. Frstner, Y. Grynko, T. Meier, and M. Wegener, *Phys. Rev. Lett.* **109**, 015502 (2012).

[30] C. Ciraci, E. Poutrina, M. Scalora, and D. R. Smith, *Phys. Rev. B* **85**, 201403(R) (2012).

[31] A. Nahata, A. S. Weling, and T. F. Heinz, *Appl. Phys. Lett.* **69**, 2321 (1996).

[32] W. L. Faust, and C. H. Henry, *Phys. Rev. Lett.* **17**, 1265 (1966).

[33] A. Leitenstorfer, S. Hunsche, J. Shah, M. C. Nuss, and W. H. Know, *Appl. Phys. Lett.* **74**, 1516 (1999).

[34] F. Kajzar, and J. D. Swalen, *Organic Thin Films for Waveguiding Nonlinear Opitcs.* (Gordon and Breach, 1996).

[35] T. h. Rasing, and I. Musevic, *Surfaces and Interfaces Liquid Crystals.* (Springer-Verlag, 2004).

[36] F. J. Rodriguez, F. X. Wang, and M. Kauranen, *Opt. Express* **16**, 8704 (2008).

[37] K. Kawase *et al.*, *Opt. Lett.* **25**, 1714 (2000).

[38] M. V. Exter, C. Fattinger, and D. Grischkowsky, *Opt. Lett.* **14**, 1128 (1989).

[39] D. Grischkowsky, S. Keiding, M. Van Exter, and C. Fattinger, *J. Opt. Soc. Am. B* **7**, 2006 (1990).

[40] K. Wang, and D. M. Mittleman, *Nature* **432**, 376 (2004).

[41] D. W. Porterfield *et al.*, *Appl. Opt.* **33**, 6046 (1994).

[42] H.-T. Chen *et al.*, *Opt. Express* **15**, 1084 (2007).

[43] N. I. Landy, S. Sajuyigbe, J. J. Mock, D. R. Smith, and W. J. Padilla, *Phys. Rev. Lett.* **100**, 207402 (2008).

[44] M. Diem, T. Koschny, and C. M. Soukoulis, *Phys. Rev. B* **79**, 033101 (2009).

[45] L. Ren *et al.*, *Nano Lett.* **12**, 787 (2012).

[46] S. Foteinopoulou, M. Kafesaki, E. N. Economou, and C. M. Soukoulis, *Phys. Rev. B* **84**, 035128 (2011).

[47] B. A. Munk, *Frequency Selective Surfaces: Theory and Design* (Wiley, Hoboken, 2005).

[48] N. I. Zheludev and Y. S. Kivshar, *Nat. Mater.* **11**, 917 (2012).

[49] M. M. Sigalas, C. T. Chan, K. M. Ho, and C. M. Soukoulis, *Phys. Rev. B* **52**, 11744 (1995).

[50] D. F. Sievenpiper, M. E. Sickmiller, and E. Yablonovitch, *Phys. Rev. Lett.* **76**, 2480 (1996).

[51] C. Luo, S. Johnson, J. Joannopoulos, and J. Pendry, *Opt. Express* **11**, 746 (2003).

[52] H.-T. Chen *et al.*, *Nat. Photon.* **2**, 295 (2008).

[53] H. Tao *et al.*, *Phys. Rev. Lett.* **103**, 147401 (2009).

[54] T. Okada and K. Tanaka, *Sci. Rep.* **1**, 121 (2011).

[55] C. Kurter *et al.*, *Appl. Phys. Lett.* **100**, 121906 (2012).

[56] J. Zhou, E. N. Economou, T. Koschny, and C. M. Soukoulis, *Opt. Lett.* **31**, 3620 (2006).

[57] P. Tassin, T. Koschny, M. Kafesaki, and C. M. Soukoulis, *Nat. Photon.* **6**, 259 (2012).

[58] S. Busch, B. Scherger, M. Scheller, and M. Koch, *Opt. Lett.* **37**, 1391 (2012).

[59] A. K. Azad, J. Dai, and W. Zhang, *Opt. Lett.* **31**, 634 (2006).

[60] H. T. Chen *et al.*, *Opt. Lett.* **32**, 1620 (2007).

[61] H. T. Chen *et al.*, *Phys. Rev. Lett.* **105**, 247402 (2010).

[62] J. M. Manceau, N. H. Shen, M. Kafesaki, C. M. Soukoulis, and S. Tzortzakis, *Appl. Phys. Lett.* **96**, 021111 (2010).

[63] K. M. Dani *et al.*, *Nano Lett.* **9**, 3565 (2009).

[64] R. A. Kaindl, D. Hagele, M. A. Carnahan, and D. S. Chemla, *Phys. Rev. B* **79**, 045320 (2009).

[65] L. Fekete, J. Y. Hlinka, F. Kadlec, P. Kuzel, and P. Mounaix, *Opt. Lett.* **30**, 1992 (2005).

[66] F. Wang, G. Dukovic, L. E. Brus, and T. F. Heinz, *Science* **308**, 838 (2005).

[67] J. Maultzsch, *et al.*, *Phys. Rev. B* **72**, 241402(R) (2005).

[68] Y. Z. Ma, L. Valkunas, S. L. Dexheimer, S. M. Bachilo, and G. R. Fleming, *Phys. Rev. Lett.* **94**, 157402 (2005).

[69] G. N. Ostojic, S. Zaric, J. Kono, V. C. Moore, R. H. Hauge, and R. E. Smalley, *Phys. Rev. Lett.* **94**, 097401 (2005).

[70] J. Wang, M. W. Graham, Y. Ma, G. R. Fleming, and R. A. Kaindl, *Phys. Rev. Lett.* **104**, 177401 (2010).

[71] J. J. Crochet *et al.*, *Phy. Rev. Lett.* **107**, 257402 (2011).

[72] H. Zhao and S. Mazumdar, *Phys. Rev. Lett.* **93**, 157402 (2004).

[73] V. Perebeinos, J. Tersoff, and P. Avouris, *Nano Lett.* **5**, 2495 (2005).

[74] J. Kono, R. J. Nicholas and S. Roche, *Topics in Applied Physics* **111**, 393 (2008).

[75] R. Matsunaga, K. Matsuda, and Y. Kanemitsu, *Phys. Rev. Lett.* **101**, 147404 (2008).

[76] O. N. Torrens, M. Zheng, and J. M. Kikkawa, *Phys. Rev. Lett.* **101**, 157401 (2008).

[77] F. Xia, M. Steiner, Y. Lin, and P. Avouris, *Nat. Nanotech.* **3**, 609 (2008).

[78] H. Zhao, and S. Mazumdar, *Phys. Rev. Lett.* **93**, 157402 (2004).

[79] L. V. Butov, A. C. Gossard, and D. S. Chemla, *Nature* **418**, 751 (2002).

[80] R. Saito, G. Dresselhaus, M. S. Dresselhaus, *Physical Properties of Carbon Nanotubes*, (Imperial College Press, London, 1998).

[81] A. H. C. Neto, F. Guinea, N. M. R. Peres, K. S. Novoselov, and A. K. Geim, *Rev. Mod. Phys.* **81**, 109 (2009).

[82] T. Kampfrath, Ph.D. thesis, Free University Berlin (2006), http://www.diss.fu-berlin.de/2006/250/.

[83] T. Ogawa, S. Watanabe, N. Minami, and R. Shimano, *Appl. Phys. Lett.* **97**, 041111 (2010).

[84] S. M. Bachilo, M. S. Strano, C. Kittrell, R. H. Hauge, R. E. Smalley, R. B. Weisman, *Science* **298**, 2361 (2002).

[85] I. Chatzakis *et al.*, *Phys. Rev. B* **86**, 125110 (2012).

[86] L. Luo *et al.*, *Nat. Commun.* **5**, 3055 (2014).

[87] M. F. Islam, D. E. Milkie, C. L. Kane, A. G. Yodh, and J. M. Kikkawa, *Phys. Rev. Lett.* **93**, 037404 (2004).

[88] T. Kampfrath *et al.*, *Phys. Stat. Sol. (b)* **244**, No. 11 3950 (2007).

[89] F. J. Garcia-Vidal, J. M. Pitarke, and J. B. Pendry, *Phys. Rev. Lett.* **78**, 4289 (1997).

[90] A. Jorio *et al.*, *Phys. Rev. B* **71**, 075401 (2005).

[91] C. Manzoni *et al.*, *Phys. Rev. Lett.* **94**, 207401 (2005).

[92] Y. Murakami, and J. Kono, *Phys. Rev. Lett.* **102**, 037401 (2009).

[93] R. Huber, R. A. Kaindl, B. A. Schmid, and D. S. Chemla, *Phys. Rev. B* **72**, 161314(R) (2005); R. A. Kaindl, D. Hägele, M. A. Carnahan, R. Lövenich, and D. S. Chemla, *Nature* **423**, 734 (2003).

[94] T. Kampfrath *et al.*, *Phys. Rev. Lett.* **101**, 267403 (2008).

[95] A. Ugawa, A. G. Rinzler, and D. B. Tanner, *Phys. Rev. B* **60**, R11305 (1999).

[96] T. Jeon *et al.*, *J. Appl. Phys.* **95**, 5736 (2004).

[97] N. Akima *et al.*, *Adv. Mater.* **18**, 1166 (2006).

[98] C. Kubler *et al.*, *Phys. Rev. Lett.* **99**, 116401 (2007).

[99] M. Hase, M. Kitajima, S. Nakashima, and K. Mizoguchi, *Phys. Rev. Lett.* **88**, 067401 (2002).

[100] S. Berciaud, L. Cognet, and B. Lounis, *Phys. Rev. Lett.* **101**, 077402 (2008).

[101] R. A. Kaindl, M. A. Carnahan, D. Hagele, R. Lovenich, and D. S. Chemla, *Nature* **423**, 734 (2003).

[102] M. J. O'Connell *et al.*, *Science* **297**, 593 (2002).

[103] F. Wang, G. Dukovic, L. E. Brus, and T. F. Heinz, *Phys. Rev. Lett.* **92**, 177401 (2004).

[104] R. Matsunaga, Y. Miyauchi, K. Matsuda, and Y. Kanemitsu, *Phys. Rev. B* **80**, 115436 (2009).

[105] T. Li *et al.*, *Nature* **496**, 69 (2013).

[106] T. Li *et al.*, *Phys. Rev. Lett.* **108**, 167401 (2012).

[107] M. Z. Hasan *et al.*, *Rev. Mod. Phys.* **82**, 3045 (2010).

[108] I. A. Nechaev *et al.*, *Phys. Rev. B* **87**, 121111(R) (2013).

[109] R. V. Aguilar *et al.*, *Phys. Rev. Lett.* **108**, 087403 (2012).

[110] S. Sim *et al.*, *Phys. Rev. B* **89**, 165137 (2014).

[111] Y. H. Wang *et al.*, *Phys. Rev. Lett.* **109**, 127401 (2012).

[112] Y. Singh *et al.*, *Phys. Rev. B* **80**, 100403(R) (2009).